LATTICE BOLTZMANN SHALLOW WATER EQUATIONS FOR LARGE SCALE HYDRAULIC ANALYSIS

Dissertation

submitted to and approved by the

Department of Architecture, Civil Engineering and Environmental Sciences

University of Braunschweig – Institute of Technology

and the

Department of Civil and Environmental Engineering

University of Florence

in candidacy for the degree of a

Doktor-Ingenieurin (Dr. -Ing.)/

Dottore di Ricerca in Civil and Environmental Engineering *)

by

Sara Venturi

born 28/06/1973

from Foligno (PG), Italy

Submitted on:	20 February 2018
Oral examination on:	8 May 2018
Professorial advisors:	Prof. Martin Geier
	Prof. Piergiorgio Manciola, Ing. Silvia Di Francesco

2018

*) Either the German or the Italian form of the title may be used.

Abstract

This thesis presents a new lattice Boltzmann model for both steady and unsteady two-dimensional shallow water equations. Throughout this work, the usage of different collision operators (CO) for the lattice Boltzmann solution of shallow water equations is proposed and investigated: BGK linear CO based on a single relaxation time (SRT), cascaded and cumulant CO with a multiple relaxation times approach (MRT). The motivation in using a MRT collision operator instead of the standard BGK, was to introduce the maximum number of adjustable parameters, which leads to an improvement of both stability and accuracy. The thesis focuses on the development, validation and applications of the aforementioned CO for shallow water flows. The cascaded LBM is based on the use of central moments as basis; it overcomes the defects in Galilean invariance of the original MRT method and it has been shown to further improve stability. An adaptation of the original formulation proposed for a single-phase fluid is therefore proposed and developed to reproduce shallow free surface flow. Furthermore, an alternative and more concise approach is based on the use of a cumulant collision operator, which relaxes, in the collision step, quantities (i.e. cumulants) that are Galilean invariant by construction. In the first part of the thesis, a convergence study of the different approaches, based on the use of the Taylor Green Vortex as test case, is performed, to compare conventional and innovative solution methods from stability and accuracy point of view. Then, the second part is devoted to analyzing different strategies to introduce, in the innovative models, the treatment of external forces term and various kinds of boundary conditions, that maintain the accuracy characteristics of the model. Special attention is due to the wet-dry front in shallow flows; in fact, a correct simulation of such processes plays a crucial role in practical engineering studies. The proposed methodologies are tested and validated through the use of analytical solutions and experimental solutions, taken as benchmarks throughout the thesis. Finally, the suitability of the proposed mathematical model for hydraulic engineering applications is discussed through the modelling of a real flood event.

Zusammenfassung

Diese Arbeit präsentiert ein neues Gitter-Boltzmann-Modell für stationäre und instationäre zweidimensionale Flachwassergleichungen. In dieser Arbeit wird die Verwendung verschiedener Kollisionsoperatoren (CO) für die Gitter-Boltzmann-Lösung von Flachwassergleichungen vorgeschlagen und untersucht: der lineare BGK CO basierend auf einer einzelnen Relaxationszeit (SRT), der kaskadierte und der Kumulanten CO mit multiplen Relaxationszeitansatz (MRT). Die Motivation bei der Verwendung eines MRT-Kollisionsoperators anstelle des standardmäßigen BGK bestand darin, die maximale Anzahl an einstellbaren Parametern einzuführen, was zu einer Verbesserung sowohl der Stabilität als auch der Genauigkeit führt. Die Arbeit konzentriert sich auf die Entwicklung, Validierung und Anwendung des oben genannten CO für die Flachwassergleichung. Die kaskadierte LBM basiert auf der Verwendung zentraler Momente als Basis. Sie überwindet die Verletzung der Galilei-Invarianz der ursprünglichen MRT-Methode und verbessert nachweislich die Stabilität. Eine Anpassung der ursprünglichen Formulierungfür die Flachwassergleichung wird daher vorgeschlagen und entwickelt. Darüber hinaus basiert ein alternativer Ansatz auf der Verwendung eines Kumulantenkollisionsoperators, der in dem Kollisionsschritt Größen (d. H. Kumulanten) relaxiert, die per Konstruktion Galilei-Invarianten sind. Basierend auf der Verwendung des Taylor Green Vortex als Testfall wird im ersten Teil der Arbeit eine Konvergenzstudie der verschiedenen Ansätze durchgeführt. Damit werden die konventionellen und innovativen Lösungsmethoden aus Sicht der Stabilitäts-und Genauigkeit verglichen. Der zweite Teil widmet sich der Analyse verschiedener Strategien, um in den innovativen Modellen die Behandlung von äußeren Kräften und verschiedene Arten von Randbedingungen einzuführen, die die Genauigkeitseigenschaften des Modells beibehalten. Besonderes Augenmerk liegt auf der Nass-Trocken-Front in flachen Strömungen. Eine korrekte Simulation solcher Prozesse spielt eine entscheidende Rolle in praktischen Ingenieurstudien. Die vorgeschlagenen Methoden werden durch die Verwendung von analytischen Lösungen und experimentellen Lösungen in Form von Benchmarks in der Arbeit getestet und validiert. Abschließend wird die Eignung des vorgeschlagenen mathematischen Modells für wasserbauliche Anwendungen durch die Modellierung eines realen Hochwasserereignisses diskutiert.

Acknowledgements

Firstly, I would like to express my sincere gratitude to my Italian and German tutors. Prof. Piergiorgio Manciola, for his continuous support, for having always trusted in me and for having always represented a point of reference in this work; thank to my advisor Silvia Di Francesco, who introduced me to the Lattice Boltzmmann world and helped me in overcoming the difficulties during my work, trying to be always present.
An especial thank to my German tutor Prof. Martin Geier, for his patience, competence and his infinite knowledge. The interest stimulated in me was a strong motivation for going ahead.
I thank Prof. Manfred Krafczyk, for his gorgeous hospitality at IRMB Department of the Technical University of Braunschweig; thank to all the guys that I knew at IRMB who supported me in the most different situations: Fritz Lewall, Hussein Alihussein, Martin Schönherr, Konstantin Kutscher, Stephan Lenz, Jan Linxweiler.
Then, a special thank to my friend and office-mate, Giulia, and to my friend Marco, who always sustained me in the moments of discouragement.
Thank to Francesca, for her sincere participation to my vicissitudes.
Thank to my parents, who understood how much could have been important for me to finish this adventure.
An immeasurable thank my husband Stefano for all his help, psychological and practical...and for having always and continuously encouraged me.
In the end, I want to apologize with my kind daughter Anna, who had to beard the distance from her mother during my staying abroad.

Contents

List of Figures

List of Tables

List of Abbreviations

1D	One-dimensional
2D	Two-dimensional
AT	Arrival Time
BGK	Bhatnagar-Gross-Krook
BC	Boundary Conditions
CO	Collision Operator
CaLB	Cascaded Lattice Boltzmann Method
CMs	Central Moments
CumLB	Cumulant Lattice Boltzmann Method
CFD	Computational Fluid Dynamics
CPU	Central Processing Unit
DF	Distribution Function f
DTM	Digital Terrain Model
EDF	Equilibrium Distribution Function f_{eq}
EDF	Electricité de France
ET	Electrical Transformer
FCM	Factorized Central Moment
FFT	Fast Fourier Transform
GIS	Geographical Information System
GPGPU	General-Purpose computing on Graphics Processing Units
IGN	Institut Geographique National
LBM	Lattice Boltzmann Method
l.u.	Lattice Units
p.u.	Physical Units
i/oBC	Inflow/outflow BC
MRT	Multiple-Relaxation-Time
NSW	Non Linear Shallow Water Equations
NRBC	Non-reflecting Boundary Condition
PDF	Probability Distribution Function
SRT	Single-Relaxation-Time
ST	Shutdown Time
SW	Shallow Water

SWE	Shallow Water Equations
WS	Water Surface

List of Symbols

c	Discrete speed $c = \frac{\Delta x}{\Delta t}$
$c_{\alpha\beta\gamma}$	Cumulant
$C_{\alpha\beta\gamma}$	Cumulant time density ρ
$c_s^{'}$	Speed of sound (l.u.)
c_s	Speed of sound (p.u.)
C_r	Courant number
e_α	Discrete speed
f	Distribution function
f_i	Discrete probability distribution function
f	Parallelized code fraction
k_x	x-component of the wave vector $\mathbf{k}$
k_y	y-component of the wave vector $\mathbf{k}$
$g^{'}$	Gravity acceleration (l.u.)
g	Gravity acceleration (p.u.)
$h^{'}$	Water depth (l.u.)
h	Water depth (p.u.)
h_{lim}	Depth threshold
i	Cartesian vector unit (phisical space) / Miller index (lattice space)
j	Cartesian vector unit (phisical space) / Miller index (lattice space)
k	Cartesian vector unit (phisical space) / Miller index (lattice space)
l_a, l_m, l	Specific lengths for different scales (microscopic, mesoscopic, macroscopic)
$\mathbf{F}$	External force
F_x	External force x direction
F_y	External force y direction
F	Probability distribution function in frequency space
F_r	Froude number
Fr_{lim}	Froude number limiter
Ma	Mach number
$m_{\alpha\beta\gamma}$	Raw moment
$\mathtt{m}$	Particle mass

n_f	Manning coefficient
P	Number of processors
T	Simulation time
S	Parallel speed up
Re	Reynolds number
$t^{'}$	Coordinate in time (l.u.)
t	Coordinate in time (p.u.)
t_D	Decay time of the wave
$t_a, t_m, t_{conv}/t_{diff}$	Specific times for different scales (respectively: microscopic, mesoscopic, macroscopic: advective or diffusive dynamic)
$\mathbf{u}^{'}$	Fluid velocity vector (l.u.)
$\mathbf{u}$	Fluid velocity vector (p.u.)
u	x-component of the velocity vector $\mathbf{u}$ (p.u.)
v	y-component of the velocity vector $\mathbf{u}$ (p.u.)
v	Particle velocity
w	z-component of the velocity vector $\mathbf{u}$ (p.u.)
$u^{'}$	x-component of the velocity vector $\mathbf{u}$ (l.u.)
$v^{'}$	y-component of the velocity vector $\mathbf{u}$ (l.u.)
$w^{'}$	z-component of the velocity vector $\mathbf{u}$ (l.u.)
v_T	average thermal velocity of molecules
w_α	Reticular weight
x	Cartesian coordinate
y	Cartesian coordinate
z	Cartesian coordinate
z_b	Bed topography
Z	Frequency space coordinate
Δx	Spatial resolution
Δt	Temporal resolution (time step)
$\delta(x)$	Dirac delta function
$\kappa_{\alpha\beta\gamma}$	Central moment
$\nu^{'}$	Kinematic viscosity (l.u.)
ν	Kinematic viscosity (p.u.)
Ω	Collision operator
ω	Collision frequency $\omega = \frac{1}{\tau}$
τ	Relaxation time
$\boldsymbol{\xi}$	Microscopic velocity
$\boldsymbol{\Xi}$	Frequency space

ξ	Microscopic velocity component
Ξ	Frequency space coordinate
v	Microscopic velocity component
Υ	Frequency space coordinate
ζ	Microscopic velocity component

To my family

Introduction

The lattice Boltzmann method (LBM) is a numerical method derived from the discretization of the kinetic equation of Boltzmann. From a statistical perspective, the approach is defined as mesoscopic, because it works at a level of detail between the microscopic and macroscopic scales, tracking the evolution of the probability distribution function of particles. While traditional CFD methods (finite difference, finite element and finite volume method) solve the macroscopic equations of fluid mechanics (Navier Stokes equations), LBM solves the discrete kinetic equations reproducing the fluid mechanics equations, in the macroscopic limit. The LBM approach is a versatile method and it has been extensively applied in different fields, such as turbulent flows, multiphase flows (Falcucci, Ubertini, and Succi, 2010), multicomponent flows, flow of complex fluids and in complex geometries (Ubertini, Bella, and Succi, 2003), porous media and thermal flows (Zarghami, Francesco, and Biscarini, 2014). However, it is not so common to use the LBM approach to simulate large scale hydraulic problems such as flooding events, dam breaks and propagation of tsunamis. The shallow water equations (SWE), representing an approximation of Navier Stokes equations, in the field of hydraulic engineering, provide a reasonable and simplified solution at a scale that is of interest to engineers and professionals. An in-depth analysis of the LBM approach applied to the solution of shallow water equations started with the work of Salmon (Salmon, 1999) and Dellar (Dellar, 2002); the research activity then continued with the comprehensive revision of the method by Zhou (Zhou, 2004), who opened the way to further work; basically, this work adopted the Zhou approach, at least in its principal outlines (i.e. collision operator, force schematization, turbulence model) and applied it to different test-cases. Only a few of them dealt with the simulation of large scale problems (Thommes, Seaid, and Banda, 2007), (Shafiai, 2011), (Prestininzi, Sciortino, and Rocca, 2013) and the problem of the effective applicability of a shallow water lattice Boltzmann model to complex hydraulic problems remains substantially open in term of efficiency, stability and accuracy. Moreover, the model that is in general used is based on the standard BGK approach in the collision step; only a small number of authors (Peng,

2012), (Liu, 2009), (De Rosis, 2017) have dealt with testing the different results obtaining using multi relaxation time (MRT) collision operators (CO). Therefore, the objective of this thesis is to test shallow water models using non - conventional MRT collision operators: central moments and cumulants CO (Geier et al., 2015) and compare the new methods with the standard BGK approach. In order to make the model applicable, in practice, to the solution of large-scale problems, an in-depth analysis of the treatment of the modelling of external forces will be performed and different boundary conditions (solid and inlet/outlet BC) will be analyzed. Moreover, a method schematizing the wetting-drying boundaries is proposed, based on a double limiter of the depth and of the Froude number. The non-conventional models will be tested and validated using the standard benchmark problems. Finally, the correctness of the proposed mathematical model for hydraulic engineering applications is discussed through the simulation of a real flood event, the Malpasset dam – break. This is an important test-case not only for its tragic importance, but also fo the availability of experimental and surveyed data.

Chapter 1

Lattice Boltzmann method

In this chapter, some fundamentals of the Lattice Boltzmann method theory will be introduced; particular attention will be paid to the different approaches in the collision step and to the meaning of Galilean invariance in LBM. In the last part, a brief explanation of the force term and boundary conditions is reported.

1.1 The Lattice Boltzmann equation

The basic idea of Boltzmann's work (Boltzmann, 1872) (Boltzmann, 1896) is that a gas is constituted of particles interacting with each other and can be described by classical statistical mechanics, and, because there are so many particles, a statistical treatment is required and applicable. The particles behaviour can be extremely straightforward and explained by just the concepts of streaming in space and a multitude of collision interactions. The Boltzmann equation describes the behaviour of particles by the evolution equation:

$$\partial_t f + \boldsymbol{\xi} \partial_{\boldsymbol{\xi}} f = \Omega \tag{1.1}$$

where f is a statistical function, the particle probability distribution function, t is the time, ξ is the microscopic particle velocity, and Ω is the collision term (collision operator, CO). The distribution function f can be seen as the probability of a particle to be in a certain state in the momentum space. The left side of equation 1.1 indicates the streaming of particles while the right side indicates the collision between particles. The collision term Ω is not straightforward to solve. Several attempts have been made to model the collision term, and the first solution obtaining a certain relevance was proposed by Bhatnagar, Gross and Krook (BGK) in 1954 (Bhatnagar, Gross, and Krook, 1954). They assumed that the collision is the process that returns particles to

the state of the local Maxwellian equilibrium:

$$\Omega = \frac{f - f^{eq}}{\tau} \tag{1.2}$$

where τ is the collision mean free time. In equation 1.2 the rate of change (i.e. the molecular collision frequency ω) is related to the collision mean free time as $\omega = \frac{1}{\tau}$. The numerical solution of equation 1.1 is possible by discretizing it in space, time, and particle velocity. In fact, in the lattice Boltzmann method, the particles are allowed only to have a discrete number of velocities. The velocities are selected such that particles travel a predefined distance in a certain time. When the distances between particles and the length of the time-steps is chosen such that they move from node to node on a Cartesian grid, all interpolations are avoided and the streaming step is exact. All non linearity is confined to an algebraic collision term, the discrete analogue of Ω in equation 1.1. Hence, the lattice Boltzmann evolution equation in three dimensions is written as (Geier et al., 2015):

$$f_{ijk(x+ic\Delta t)(y+jc\Delta t)(z+kc\Delta t)(t+\Delta t)} = f_{ijkxyzt} + \Omega_{ijkxyzt} \tag{1.3}$$

where i, j and $k \in \mathbb{Z}$ and x, y and z are the variables in space, ic, jc and kz are the variables in velocity space with $\boldsymbol{\xi} = (ic, jc, kc)$, Δx and Δt are, respectively, the grid spacing and the time-step, $c = \frac{\Delta x}{\Delta t}$ is the discrete speed. Figure 1.1 shows a three-dimensional discretization of the velocity space with 27 discrete speeds, the D3Q27 lattice. In fact, it is generally used the notation $DdQq$ for a q-velocity model in a d-dimensional space. The node in the middle is the source point (zero velocity) from which f streams into the directions of the 26 neighbours. The distance between the source node and any of the neighbours is unitary with i, j and $k \in \{-1, 0, 1\}$. The lattice Boltzmann method is a numerical method for solving the Navier-Stokes equations, based on the discretization of space and velocity and is able to exactly satisfy the conservation laws (mass, momentum and angular momentum). The hydrodynamic variables such as density, velocity are represented by the moments of the Probability Distribution Function f (PDF).

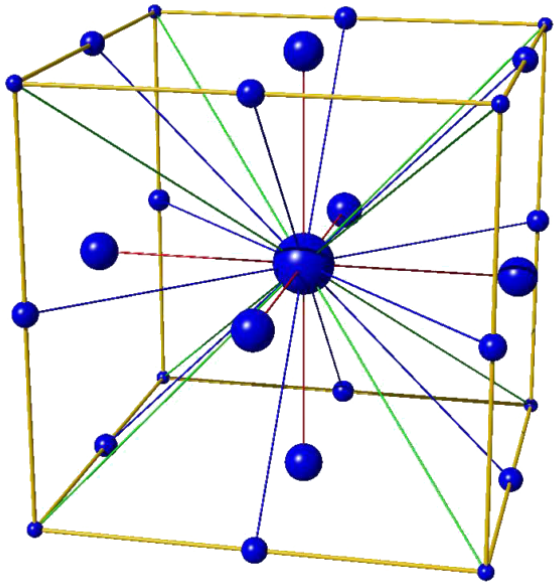

FIGURE 1.1: Moment distribution in D3Q27 lattice. The point in the middle is the source point at rest. The others are the links to the other neighbour directions. The volume of the spheres shows the weight of the states in the equilibrium distribution (Geier, 2006).

The most relevant difficulties of LB method can be found in the collision operator. The widespread solution based on a single relaxation time approach (SRT BGK method) (Qian, D'Humières, and Lallemand, 1992) is characterized by a relatively simple implementation. The relaxation rate is chosen only considering binary collisions, that are the collisions with the highest probability to happen (Geier, 2006). In order to maximize the number of adjustable parameters and increase both stability and accuracy, the multiple relaxation times MRT was introduced (D'Humières, 1994). Even though it was demonstrated that MRT CO improves the solution of LBM, it introduces an additional Galilean invariance violation and hyper-viscosity problems (Geier et al., 2015). The first problem is due to the definition of the moments. In fact, the MRT method modifies the PDF into a set of raw moments (Geier et al., 2015) using a linear transformation. Each moment is orthogonal to all the others and relaxes with its own rate. However, the orthogonality of the moments is not reference frame independent (Krafczyk et al., 2015) and orthogonality is not maintained if the reference frame is changed. Therefore, the original MRT method further violates the Galilean invariance, compared to a BGK model. Hyper-viscosity problems come from the coupling of the

different relaxation rates, because the moments are not statistically independent. The cascaded LBM (Geier, Greiner, and Korvink, 2006) solves the first problem, using as observable quantities central moments, defined in a frame co-moving with the fluid. However, a co-moving frame of reference did not guarantee that the moments evolved independently. In fact, this assumption leads to incorrect results when the relaxation rates of different moments are not optimally selected. A solution to this problem is the factorized central moment method (FCM). By means of the factorization, the degrees of freedom are decoupled and the central moments turn into moments statistically independent of each other.

1.1.1 Cumulant LBM

The factorization in (Geier, Greiner, and Korvink, 2009) was theorized with the cumulant LBM (Geier et al., 2015), which at the same time oversteps the two problems of statistical independence of the moments and hyperviscosity.
The discrete probability distribution function (PDF) can be written in continuous form using the microscopic velocities $\boldsymbol{\xi} = (\xi, v, \zeta)$ and the Dirac δ function:

$$f(\boldsymbol{\xi}) = f(\xi, v, \zeta) = \sum_{ijk} f_{ijk} \delta(ic - \xi) \delta(jc - v) \delta(kc - \zeta) \tag{1.4}$$

The two-sided (bilateral) Laplace transform of this distribution $f(\boldsymbol{\xi})$ is continuous and smooth in the frequency space $\boldsymbol{\Xi} = (\Xi, \mathrm{Y}, Z)$ and it is equal to:

$$F(\boldsymbol{\Xi}) = \mathcal{L}\{f(\boldsymbol{\xi})\} = \int_{-\infty}^{\infty} f(\boldsymbol{\xi}) e^{-\boldsymbol{\Xi}\cdot\boldsymbol{\xi}} d\boldsymbol{\xi} \tag{1.5}$$

In frequency space, for the observable quantities c_α, statistically independent and Galilean invariant, the joint probability function can be expressed in the form:

$$F(\boldsymbol{\Xi}) = F(\Xi, \mathrm{Y}, Z) = \prod_{\alpha} F_\alpha(c_\alpha) \tag{1.6}$$

i.e., the $F(\boldsymbol{\Xi})$ represents the product of the individual probabilities of c_α (factorization). If the logarithm of joint probability is considered, the probability distribution function can be expressed in Taylor series. The cumulants of the

distribution c_α are equal to the coefficient of the series:

$$c_{\alpha\beta\gamma} = \frac{\partial^\alpha \partial^\beta \partial^\gamma}{\partial \Xi \partial \mathrm{Y} \partial Z} \ln \left(\frac{F\left(\Xi, \mathrm{Y}, Z\right)}{\varrho_0} \right) |_{\Xi, \mathrm{Y}, Z=0} \tag{1.7}$$

where ϱ_0 is a density metric for dimensional consistency (Kian Far et al., 2016a). Cumulants respect the hypothesis of statistical independence between different degrees of freedom and frame invariance by definition. Each collision process can be modeled by an individual rate equation:

$$c^*_{\alpha\beta\gamma} = \quad c^{eq}_{\alpha\beta\gamma} \quad \omega_{\alpha\beta\gamma} + \left(1 - \omega_{\alpha\beta\gamma}\right) c_{\alpha\beta\gamma} \tag{1.8}$$

The asterisk * indicates the post-collision cumulant, $c^{eq}_{\alpha\beta\gamma}$ is the equilibrium value of the cumulant and $\omega_{\alpha\beta\gamma}$ is the relaxation frequency. In frequency space the equilibrium distribution is smooth and the logarithm form can be expanded into Taylor series:

$$\ln\left(F^{eq}\left(\Xi, \mathrm{Y}, Z\right)\right) \quad = \quad \ln \frac{\varrho}{\varrho_0} - \Xi u - \mathrm{Y} v - Z w + \frac{c_s^2}{2} \left(\Xi^2 + \mathrm{Y}^2 + Z^2\right) \tag{1.9}$$

where c_s^2 is the square speed of sound and u,v,w are the macroscopic velocity values. The logarithm of the Laplace transformed equilibrium is a polynomial function with a finite number of terms in Taylor expansion; hence the series is characterized by a finite number of coefficients (i.e. cumulants). The complete discussion about theory of cumulants is in (Geier et al., 2015). Recent applications of cumulant LBM can be found in (Pasquali, 2017), (Pasquali, Geier, and M., 2017) and (Kian Far et al., 2016b).

1.1.2 Raw moments and central moments

As the bilateral Laplace transform function of f, $F\left(\Xi, \mathrm{Y}, Z\right)$, can be considered equivalent to the moments generating function of the distribution (Dupré, 2010), raw moments can be obtained as:

$$m_{\alpha\beta\gamma} = \frac{\partial^\alpha \partial^\beta \partial^\gamma}{\partial \Xi \partial \mathrm{Y} \partial Z} \left(\frac{F\left(\Xi, \mathrm{Y}, Z\right)}{\varrho_0} \right) |_{\Xi, \mathrm{Y}, Z=0} = \sum_{i,j,k} i^\alpha j^\beta k^\gamma f_{ijk} \tag{1.10}$$

Hereafter, non-orthogonal central moments, used in the cascaded LBM as observable quantities and derived from a centred distribution function:

$$\kappa_{\alpha\beta\gamma} = \frac{\partial^{\alpha}\partial^{\beta}\partial^{\gamma}}{\partial\Xi\partial\Upsilon\partial Z}\left(\frac{\tilde{F}\left(\Xi,\Upsilon,Z\right)}{\varrho_0}\right)\Big|_{\Xi,\Upsilon,Z=0} = \sum_{i,j,k}\left(i-u/c\right)^{\alpha}\left(j-v/c\right)^{\beta}\left(k-w/c\right)^{\gamma} f_{ijk} \tag{1.11}$$

where $\tilde{F}$ is a centred distribution function as in (Geier et al., 2015); u, v, and w are the components of the local velocity vector.

1.2 Relevant scales in CFD models

The lattice Boltzmann method can be considered a mesoscopic approach between the microscopic methods and the conventional numerical methods based on the solution of Navier Stokes equation. In Figure 1.2, the hierarchy of lengths and time scales in CFD models is shown (Krüger et al., 2016).

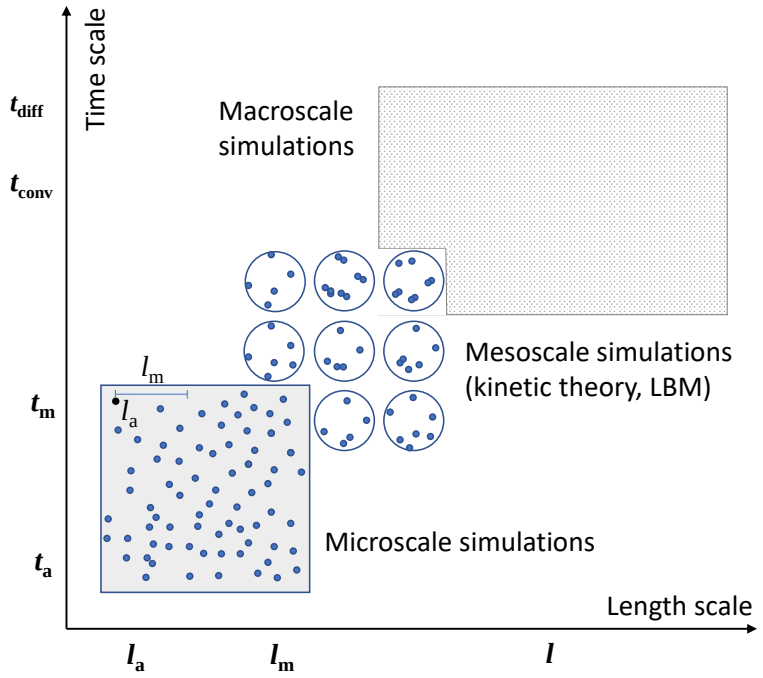

FIGURE 1.2: Hierarchy of lengths and time scales in CFD models. Adapted from (Krüger et al., 2016).

The x-axis shows the specific lengths for different scales: l_a is the size of the fluid atom or molecule in microscale simulations; l_m is the distance travelled between two successive collisions in mesoscale simulations; l is the typical scale related to tangible properties (velocity, density) in a macroscale simulation. Coupled with the previous lenght scales, there are the following

time scales: t_a, t_m and t_{conv} or t_{diff} at macroscopic scale. The kinetic theory, at which LB method is related, operates at mesoscopic scale. To the length l_m, representing the distance covered between two successive collisions of particles, is associated, in the y-axis, t_m, the mean flight time between two successive collisions; t_m is equal to $\frac{l_m}{v_T}$, where v_T represents the average thermal velocity of the molecules.
In a macroscale simulation, it is possible to have inertial or viscous regime (respectively, advective or diffusive dynamics); it depends on what is the shortest (most relevant) time scale: $t_{conv} \simeq \frac{l}{u}$ or $t_{diff} \simeq \frac{l^2}{\nu}$, where u is the macroscopic velocity and ν is the kinematic viscosity.
The ratio between these two hydrodynamic time scales is the well-known Reynolds number $Re = \frac{ul}{\nu}$.
The Mach number (Ma) defines the ratio between the acoustic and advective time scales. In practice, we can usually assume steady fluid flow with $Ma \leq 0.1$ to be incompressible.

1.3 Galilean invariance in LBM

Recently, the issue of violation of Galilean invariance in LBM has been largely discussed (Lallemand and Luo, 2000), (Geier, Greiner, and Korvink, 2006), (Geier, 2006), (Geier et al., 2015), (Geier, Fakhari, and Lee, 2015).
The Boltzmann equation in 1.1, defined in the continuum space, is invariant under Galilean transformations. In kinetic theory, this is expressed by using the velocity $\xi - u$, the difference between ξ and the local fluid velocity u. The lattice Boltzmann approach fulfils computational efficiency by restricting the infinite set of particle velocity ξ in equation 1.1 to a finite set and evolving the finite set of functions $f_\alpha(x,t)$ $\alpha = 1, ..., N$ rather than $f(x, \xi, t)$. However, the adoption of a finite velocity set f_α leads to a finite number of independent moments; this breaks Galilean invariance at the level of the discrete Boltzmann equation. The problem is, in general, solved within the limit of second order accuracy (Geier et al., 2015). However, beyond the second order, the violation of Galilean invariance leads to spurious dependencies; i.e., the dependence of the viscosity from the velocity of the flow; the coupling between moments with different relaxation rate in the collision; a phase lag in the advection of vortexes with a superimposed velocity field. The first two problems have been resolved introducing the cumulant CO; a solution for the third problem is discussed in (Geier and Pasquali, 2018) where different

strategies are analyzed. In particular, the proposed solutions deal with increasing of the number of speeds or using a different arrangement of reticular speeds; it is also proposed a modified equilibrium of second order cumulants based on finite differences corrections.

1.4 Evaluation of the force term in LB method

Different approaches can be considered in order to include the force term in LBM. Luo (Luo, 1993) suggested that the force term can be introduced into the collision term; in (Shan and Chen, 1994) the body force is introduced in the collision operator. Later, in (Li-Luo, 1998) Luo demonstrated that the first choice is a special case of the second. In (Buick and Greated, 2000) it was concluded that the best results can be obtained by adding the force term in the collision process and shifting the field velocity of a quantity proportional to the external force. Zhou, in his BGK shallow water model, demonstrated that the external forces can be included in the mathematical models simply adding them to the streaming process (Zhou, 2004).

1.5 Boundary conditions

Infinitely large systems cannot be simulated. The size of the simulation domain must be bounded, and the domain edges must be treated by using some boundary condition (BC). In this section, different kind of solid boundary conditions and inlet/outlet boundary conditions are described. Several studies show that boundary conditions play a critical role on the results of simulation and can affect the accuracy, efficiency and stability of the simulation. Indeed, even though the boundary conditions concern a limited part of the fluid domain, they can extremely affect the flow solution. Some representative works about boundary conditions are due to (Ginzburg and d'Humieres, 2003), (Junk and Yang, 2005), (Latt et al., 2008). Boundary conditions and initial conditions are still a non-trivial task in LBM and its determination is more complex than in conventional numerical methods solving the Navier Stokes equations (Krüger et al., 2016). In fact, rather than specifying the macroscopic variables of interest at the boundary (i.e. velocity or pressure), in LB method conditions for the mesoscopic populations have to be set up.

1.5.1 Periodic boundary conditions

Periodic boundary conditions apply only when the edge of the system is connected to the opposite edge; they state that the fluid leaving the domain on one edge will, instantaneously, re-enter at the opposite edge. Consequently, periodic boundary conditions conserve mass and momentum over time. For example, a periodic boundary condition in the x-direction can be applied by specifying the unknown distributions at inflow boundary after streaming with the corresponding distributions at outflow boundary (see Figure 1.3):

$$f_\alpha(1,t) = f_\alpha(N_x,t) \qquad \alpha = 1,5,8$$

$$f_\alpha(N_x,t) = f_\alpha(1,t) \qquad \alpha = 6,3,7$$

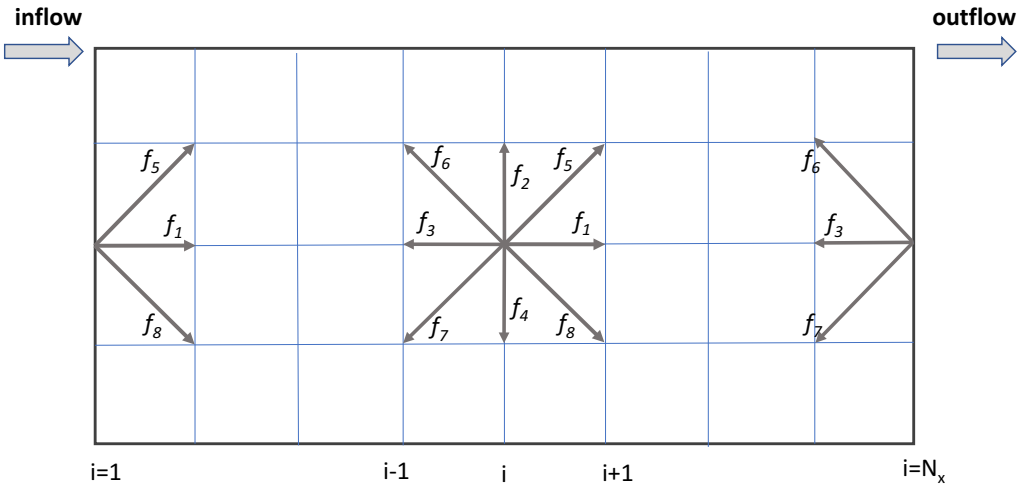

FIGURE 1.3: Periodic boundary condition in the x direction.

Similarly, a periodic boundary condition in the y direction can be applied.

1.5.2 Solid boundary conditions

No-slip boundary conditions

One of the most simple and common treatment of boundary conditions is the no-slip BC. The correct implementation is crucial for modelling confined fluid flow phenomena and other problems including solid boundaries. The standard LB boundary condition to model walls is the bounce-back method (He et al., 1997), (Ginzbourg and Adler, 1994). The basic rule of bounce-back

is illustrated in Figure 1.4. When the bounce-back is applied at boundaries, the populations moving against the wall during the streaming step are reflected towards where they originally came from. During the collision with the wall, normal and tangential momentum components are reversed. Then, the average momentum of populations along the direction in Figure 1.4, before and after collision, is equal to zero; in fact: $\mathtt{m}\mathtt{v}\left(t+\Delta t\right)=-\mathtt{m}\mathtt{v}\left(t\right)$, where $\mathtt{v}$ is the particle velocity and $\mathtt{m}$ the mass. In bounce-back boundary conditions, the populations leaving the nodes at boundaries at time t meet the surface of the wall and they are reflected back, arriving at time $t+\Delta t$ at the node from which they came. For these populations, the standard streaming step is replaced by the equations (see Figure 1.5):

$$f_{\alpha}\left(i,t+\Delta t\right)=f_{\overline{\alpha}}\left(i,t\right)$$

where i is the grid coordinate at the boundary; f_{α} and $f_{\overline{\alpha}}$ are respectively, the leaving and the reflected populations. It has to be pointed out that the bounce back method here illustrated and used in this study is the half-way bounce back (Sukop and Thorne, 2006): particles travel only half of the distance between the nodes at boundary and solid node, so that the inversion of the velocity occurs during the streaming step. The bounce back method can be implemented easily also for flows in arbitrary complex geometries. In fact, the position of solid points is not required and the code results efficient and easy to implement (Gallivan et al., 1997).

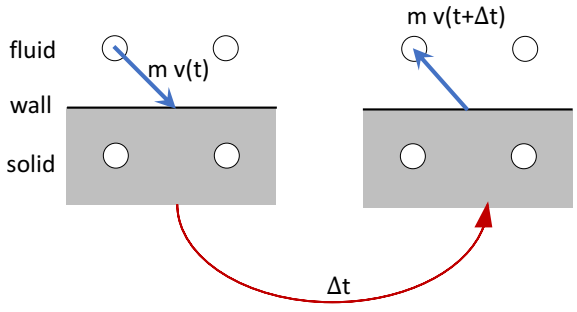

FIGURE 1.4: Principle of bounce back method. Reproduced from (Krüger et al., 2016).

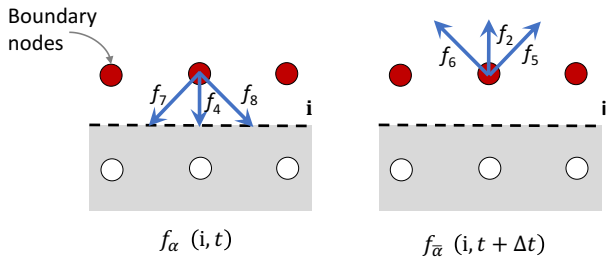

FIGURE 1.5: Evolution in time of the bounce-back rule equation at a bottom wall.

For the case depicted in Figure 1.5, the implementation is:

$$f_6\left(i, t+\Delta t\right) = f_8\left(i, t\right)$$

$$f_2\left(i, t+\Delta t\right) = f_4\left(i, t\right)$$

$$f_5\left(i, t+\Delta t\right) = f_7\left(i, t\right)$$

The bottom grey shaded domain is the solid region, and the dashed line corresponds to the location of the no-slip boundary; red and white circles denote boundary and solid nodes, respectively.

1.5.3 Inlet/outlet boundaries

Due to computational limitations, the simulation domain has to be truncated and boundary conditions have to be set where physical problems do not have boundaries. This kind of boundaries are called inflow/outflow boundary conditions (hereinafter, i/oBC). The i/oBC boundaries are essentially inlets or outlets where the flow either enters or leaves the computational domain and where it should be imposed, for example, the velocity or the density. The problem is often not insignificant, and it can produce both physical and numerical difficulties. The i/oBC used in this work are described in chapter 3, section 3.3.

Chapter 2

Lattice Boltzmann shallow water equations

2.1 Shallow water equations

The shallow water equations (SWE) derive from the three dimensional incompressible Navier-Stokes equations and are valid for problems in which vertical dynamics can be neglected compared to horizontal effect, with several simplified assumptions: the water depth is small enough so that such flows are characterized by horizontal motion; the assumption of hydrostatic pressure replaces the momentum equation in the vertical direction and the vertical acceleration can be neglected.
The shallow water equations derive from the Navier Stokes equations, the continuity equation and the momentum equation, hereinafter written in tensor form using the Einstein summation convention:

$$\frac{\partial u_j}{\partial x_j} = 0 \tag{2.1}$$

$$\frac{\partial u_i}{\partial t} + \frac{\partial \left(u_i u_j\right)}{\partial x_j} = F_i - \frac{1}{\rho}\frac{\partial p}{\partial x_i} + \nu \frac{\partial^2 u_i}{\partial x_j \partial x_j} \tag{2.2}$$

where the subscripts i and j are space direction indices, t the time, u the velocity, F_i the body force per unit mass in i direction, ρ the fluid density, ν the kinematic viscosity, p the pressure. The term on the left is the inertial term, where $\frac{\partial \left(u_i u_j\right)}{\partial x_j}$is called convective term. On the right side, the pressure term and the viscous term are shown.
The governing equations for shallow water can be derived from 2.1 and 2.2. In fact, they are obtained using an integration over depth in order to obtain vertically averaged quantities. The second term on the right of the equation

2.2 (pressure term) becomes:

$$\int_{z_b}^{h+z_b} \frac{1}{\rho}\frac{\partial p}{\partial x} dz = gh\frac{\partial(h+z_b)}{\partial x} \tag{2.3}$$

where h is the water depth, z_b is the bed elevation above datum. In fact, shallow water equations are characterized by a pressure p approximately hydrostatic over the vertical direction:

$$\frac{\partial p}{\partial z} = -\rho g \tag{2.4}$$

where ρ is the water density and g the gravity acceleration. Integration of the equation 2.4 over depth with the boundary condition that the pressure at free surface is the atmospheric pressure $p_a = 0$ leads to the hydrostatic pressure approximation in shallow water flow:

$$p = \rho g\left(h + z_b - z\right) \tag{2.5}$$

The following system of 2D shallow water equations are given as in (Zhou, 2004) and can be written in the following form:

$$\frac{\partial h}{\partial t} + \frac{\partial(hu_j)}{\partial x_j} = 0 \tag{2.6}$$

$$u_j = \frac{1}{h}\int_{z_b}^{z_b+h} u dz \tag{2.7}$$

$$\frac{\partial(hu_i)}{\partial t} + \frac{\partial(hu_iu_j)}{\partial x_j} = -g\frac{\partial}{\partial x_i}\left(\frac{h^2}{2}\right) + \nu\frac{\partial^2(hu_i)}{\partial x_j \partial x_j} + F_i \tag{2.8}$$

where h his the water depth, u is the velocity, ν is the kinematic viscosity, F_i is the external force in the i direction. The shallow water regime is shown in Figure 2.1. The external force term can be written as follows:

$$F_i = F_{Pi} + F_{si} + F_{wi} + F_{Ci} \tag{2.9}$$

where the F_{Pi} is the force due to gravity and defined in 2.3, the F_{si} the bed shear stress defined as:

$$F_{si} = C_b u_i \sqrt{u_i u_i} \tag{2.10}$$

where $C_b = g\frac{n_f^2}{h^{1/3}}$ is a friction factor in which n_f is the Manning's coefficient at the seabed. The terms F_{wi} and F_{Ci} are, respectively, the wind shear stress and the force representing the Coriolis effect. The last two terms are not

considered in this study.

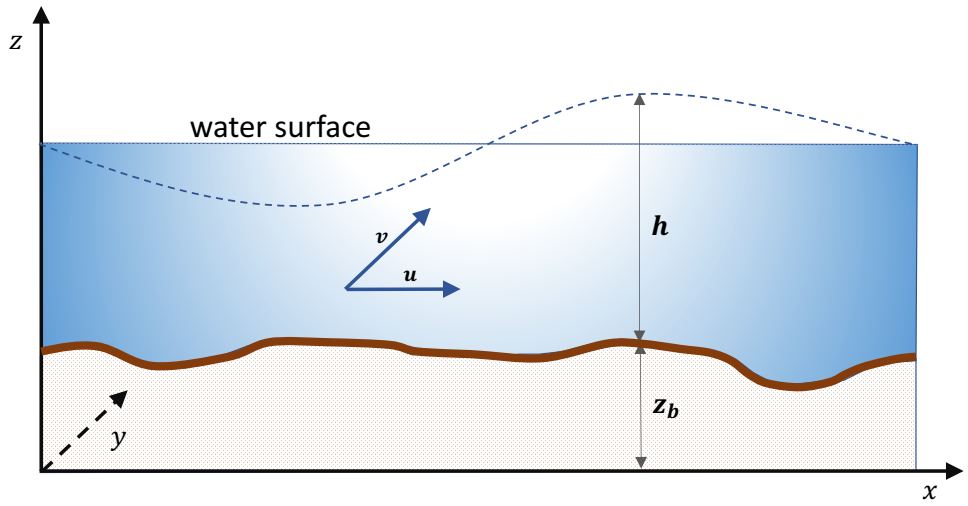

FIGURE 2.1: Parameters of shallow water equations (SWE). Horizontal velocities (u, v); water depth h; water surface (continuous line: steady flow; dashed line: unsteady flow).

2.1.1 Literature review

The shallow water equations (SWE) allow to simulate flows in water bodies where the horizontal length scale is larger than the fluid depth. If vertical variations must be taken into account, these variations can be separated from the horizontal ones using a set of shallow water equations for a series of horizontal fluid layers (i.e., multilayer SWE) (Prestininzi, Sciortino, and Rocca, 2013). The SWE are largely adopted in ocean engineering (Salmon, 1999), hydraulic engineering (Meselhe, Sotiropoulos, and Holly, 1997), (Valiani, Caleffi, and Zanni, 2002) and coastal engineering (George, 2006), (Brocchini and Dodd, 2008), (Huynh, Dodd, and Zhu, 2017). In fact, the SWE allow to study a wide range of physical problems such as storm surges, tidal flows and fluctuations in estuary and coastal water regions, tsunami and bore wave propagation, stationary hydraulic jump, off-shore structures and open channel flows. The SWE can also be coupled to transport equations to model the conveyance of several quantities such as temperature, pollutants, salinity and sediments.

It is not trivial to model such realistic large scale flow problems since the terrain topography can be complicated and irregular. Traditional numerical methods (finite difference, finite volume and finite element methods) have been used to simulate the SWE (Bermudez and Vazquez, 1994); (Randall J.LeVeque, 1998); (Stansby and Zhou, 1998), (Prestininzi, Lombardi, and La

Rocca, 2016); (Toro, 1992); (Vazquez, 1999), inter alia. Most of these methods put in evidence that the application of bed slope and friction forces can lead to inaccurate solutions due to numerical errors, i.e. (Bermudez and Vazquez, 1994); (Randall J.LeVeque, 1998); (Vazquez, 1999). In addition, the extension of these schemes to complex geometries is not straightforward (Benkhaldoun, Elmahi, and Seaid, 2007). Some of these approaches are very computational expensive if applied to real flows (Vukovic and Sopta, 2002). Since the problems are posed at a large scale, it should be the aim to develop a simple and accurate representation of the source term to simulate realistic shallow water flows without resorting to upwind discretization or Riemann problem solvers (Benkhaldoun, Elmahi, and Seaïd, 2010).

2.1.2 LBM for shallow water equations

Hereafter, a description of standard SRT and MRT model for the solution of shallow water lattice Boltzmann equations is given; moreover, in the next paragraphs, the most significant works concerning the two type of models are briefly introduced.

Single relaxation time models

The conventional models solving the shallow water equations are generally based on a BGK CO (section 1.1). The implementation scheme, solved on a regularly spaced domain, is described by the discrete Lattice Boltzmann relation :

$$f_\alpha\left(x + e_a\Delta t, t + \Delta t\right) = f_\alpha\left(x, t\right) + \Omega_\alpha + F_\alpha \qquad \alpha = 0, ..., n-1 \tag{2.11}$$

where x represents the position of the particle in the discretized space at time t, $f_\alpha\left(x, t\right)$ are the particle distribution functions and e_α represents the set of discrete speeds, along the allowed n - 1 lattice directions. In a D2Q9 model n=9. Ω_α is the collision operator, F_α represents the external force. Several authors dealt with the solution of shallow water using the LBM. Dellar proved that the shallow water lattice Boltzmann model, based on the typical truncation of the EDF, from continuum Boltzmann equation of kinetic theory ("a priori" approach), is not stable for the coupling between the hydrodynamic and "ghost" modes (Dellar, 2002). Different and stable equilibria have been introduced by Salmon (Salmon, 1999) who reduced the instability effects of D2Q9 shallow water model. Zhou (Zhou, 2004) built a model with EDF

and evolution equation equal to Salmon, but enhanced it with an external force treatment, different boundary conditions and a turbulence model. This model was successfully applied in highly efficient simulations of structure-fluid interaction (Geveler et al., 2011), multilayer shallow water equations (Prestininzi, Sciortino, and Rocca, 2013) and (Prestininzi, Lombardi, and La Rocca, 2016), modelling of wetting–drying processes (Liu and Zhou, 2014). The aforementioned authors suggest to express the equilibrium PDF as a power series in macroscopic velocities up to second order, assuring mass and momentum conservation:

$$f_\alpha^{eq} = \begin{cases} h - \frac{5gh^2}{6} - \frac{2h}{3}\,\mathbf{u}\cdot\mathbf{u} & \alpha = 0 \\ \beta h\left(\frac{gh}{6} + \frac{1}{3}\,(e_\alpha\cdot\mathbf{u}) + \frac{1}{2}\,(e_\alpha\cdot\mathbf{u})^2 - \frac{1}{6}\,\mathbf{u}\cdot\mathbf{u}\right) & \alpha = 1,...,8 \end{cases} \tag{2.12}$$

where $\mathbf{u}$ is the velocity vector and β assumes the value 1 if $\beta = 1,...,4$ and $\frac{1}{4}$ otherwise (De Rosis, 2017).

Multi relaxation time models

MRT Lattice Boltzmann Models have been recently proposed as alternative to BGK models. Several authors introduced in shallow water LB model the MRT originally developed by d'Humieres et al. (D 'Humieres et al., 2002). Just to name a few, Liu (Liu, 2009) put in evidence the longer simulation times by using an MRT rather than an SRT CO; on the other hand, Tubbs (Tubbs and Tsai, 2011) highlighted the higher stability compared with an SRT model, thanks to the possibility to choose in the best way relaxation rates not related to physical parameters. Peng (Peng, 2012) put in evidence the improvement of the stability of the model and its capability of simulating flows with higher Reynolds number.

Lately, a formulation based on central moments has been proposed by De Rosis (De Rosis, 2017). Starting from the equilibrium functions used in (Salmon, 1999) and (Zhou, 2004), De Rosis chose a suitable non-orthogonal basis in order to define a set of pre-collision central moments, then separately relaxed with independent relaxation rates. The method is consistent with the BGK operator, as the latter is recovered exactly if all the moments relax with a common frequency.

2.2 Stability conditions in LBM shallow water

Several researchers (Liu, 2009), (Zhou, 2004), (Shafiai, 2011), dealing with the solution of shallow water with the lattice Boltzmann method, assert that the method has been tested to remain stable under some conditions. First of all, there must be diffusion phenomena for a water flow, so the kinematic viscosity ν should be positive. Then:

$$\nu = c_s^2 \left(\tau - \frac{1}{2}\right) \frac{\Delta x^2}{\Delta t} > 0$$

It follows that:

$$\tau > \frac{1}{2}$$

Secondly, it is necessary to respect the Courant-Friedrichs-Lewy (CFL) (LeVeque, 1996) condition to make the simulation stable. The Courant number C_r allows to compare the speed $\frac{\Delta x}{\Delta t}$ of the propagation of informations in the model with the physical speed of the advection of the fluid. i.e. if $C_r > 1$, the simulation cannot propagate the physical solution quickly enough and the simulation becomes unstable. Therefore, generally $C_r < 1$ is a necessary condition for stability. It means that:

$$\sqrt{u_i u_j} < \frac{\Delta x}{\Delta t}$$

and

$$\sqrt{gh} < \frac{\Delta x}{\Delta t}$$

where $\sqrt{gh}$ is the celerity of a shallow wave. Finally, it is generally considered that, in the lattice Boltzmann shallow water method, the $F_r > 1$ should remain lower than one so that the flow is limited to sub-critical flow (Zhou, 2004). Then:

$$F_r = \frac{\sqrt{u_i u_j}}{\sqrt{gh}} < 1$$

In the shallow water framework, the limitation on the Froude number is a serious defect for real applications, where transcritical flows are frequently encountered. It is noteworthy that La Rocca (La Rocca et al., 2015) proposed a multispeed model with sixteen speeds, able to simulate transcritical and supercritical 2D shallow water flows, thanks to the higher order equilibrium terms.

2.3 From lattice units to physical units

In the LB simulation, the grid spacing Δx is assumed as the space unit. Therefore, if a linear size of L meters is represented using N grid points, the space unit is expressed in meters:

$$\Delta x = \frac{L}{N} \qquad (m)$$

In a similar way, the time unit of LB simulations is the elementary lattice time step. Its physical value can be defined via the speed of sound as follows, as $c_s = c_s^{'} \frac{\Delta x}{\Delta t}$, where c_s and $c_s^{'}$ are, respectively, the physical value and the lattice value of the speed of sound. Then:

$$\Delta t = \frac{c_s^{'}}{c_s} \Delta x \qquad (s)$$

The speed of sound represents the velocity at which the waves travel (Succi, 2001).
In shallow flow simulations, the speed of sound can be assumed equal to $\sqrt{\frac{gh}{2}}$ (section 3.1.2); then, the value of the lattice time step expressed in seconds becomes:

$$\Delta t = \frac{\sqrt{\frac{g^{'}h^{'}}{2}}}{\sqrt{\frac{gh}{2}}} \Delta x \quad (s)$$

where $g^{'}$ and g, $h^{'}$ and h are the value of the gravity acceleration and of the depth, respectively, in lattice and physical units. If the value of the depth h is maintained not scaled then $(h^{'} = h)$ the expression of the lattice time step becomes:

$$\Delta t = \sqrt{\frac{g^{'}}{g}} \Delta x \quad (s) \tag{2.13}$$

Chapter 3

Innovative models for shallow water equations

In this chapter, an explanation of the principal frameworks of the innovative models studied in this work: the lattice pattern and the characteristics of the speed of sound, the different collision operators taken into consideration, the concept of aliasing, the approach for the inclusion of the force term and the different boundary conditions.
About the style of this chapter, the parameters in the formulas have to be intended as expressed in lattice units, if not differently specified. In fact, the equations are written as they were implemented in the code and, in a LB code, it recommended to work with lattice units, as the use of physical units could bring to numerical errors.

3.1 D2Q9 model

3.1.1 Lattice pattern

The Figure 3.1 depicts lattice directions and velocities for the D2Q9 lattice pattern (Wolf-Gladrow, 2004) adopted in our models. The lattice pattern in LBM has the two functions to represent the points of the grid and to determine the motion of particles directions. In two dimensions, the vectors of the particles speed are defined as:

$$e_0 = \begin{pmatrix} 0 \\ 0 \end{pmatrix} \quad e_1 = \begin{pmatrix} 1 \\ 0 \end{pmatrix} \quad e_2 = \begin{pmatrix} 0 \\ 1 \end{pmatrix} \quad e_3 = \begin{pmatrix} -1 \\ 0 \end{pmatrix} \quad e_4 = \begin{pmatrix} 0 \\ -1 \end{pmatrix}$$
$$e_5 = \begin{pmatrix} 1 \\ 1 \end{pmatrix} \quad e_6 = \begin{pmatrix} -1 \\ 1 \end{pmatrix} \quad e_7 = \begin{pmatrix} -1 \\ -1 \end{pmatrix} \quad e_8 = \begin{pmatrix} 1 \\ -1 \end{pmatrix}$$

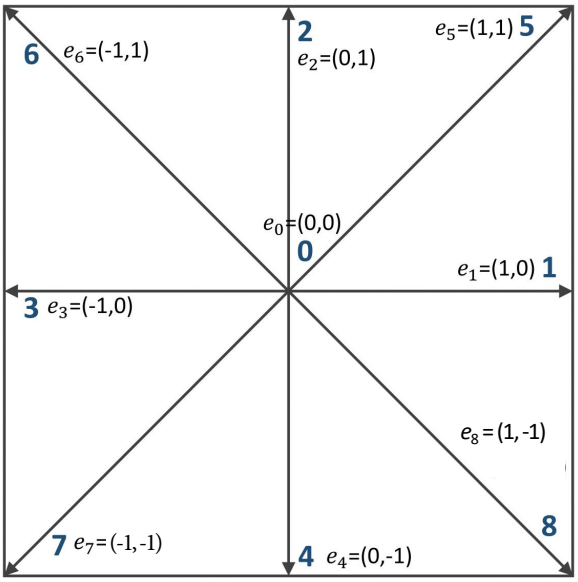

FIGURE 3.1: D2Q9 lattice velocity scheme and corresponding lattice velocity components.

The D2Q9 pattern satisfies the homogeneity requisite, strictly related to the definition of Galilean invariance (Geier, 2006). In fact, an homogeneous velocity distribution implies that it is always necessary to have s^D speeds, where D is the number of dimensions and s is the number of discernible states in a single dimension.

3.1.2 Speed of sound in SW model

In shallow water model the speed of sound in viscosity is not constant but is a function of fluid elevation h and gravity acceleration g:

$$c_s'^2 = \frac{g'h'}{2} \tag{3.1}$$

This is in accordance with the theory: in fact, two-dimensional compressible Navier-Stokes equations can be obtained from the shallow water equations using as equation of state the expression: $P = \frac{1}{2}g\rho^2$ (Dellar, 2002). It completely differs from standard Lattice Boltzmann models, in which the speed of sound is constant and equal to $c_s'^2 = 1/3$.

3.1.3 Viscosity

In LBM, the relaxation rate ω is related to the mean free time between two binary collisions and it is defined as the inverse of the parameter τ (Geier,

2006). The kinematic viscosity ν (transport coefficient) can be expressed as:

$$\nu^{'} = c^{'2}_{s}\, \tau_{binary} \tag{3.2}$$

and, consequently:

$$\nu^{'} = c^{'2}_{s}(\frac{1}{\omega} - \frac{1}{2}) \tag{3.3}$$

where $c^{'}_{s}$ is the lattice speed of sound as defined in section 3.1.2. In standard LBM, the value of $c^{'2}_{s}$ is given by the aliasing of the (raw) moments m_{10} and m_{30} as explained in section 3.1.7. In SRT models, the values of ω is unique; on the other hand, in MRT models (i.e. cascaded and cumulant models), different relaxation rates exist for different moments. The relation between them is explained in section 3.1.5.

3.1.4 Macroscopic variables

The macroscopic properties (water depth h and velocity field u_i) of the flow are computed, respectively, from the zero order moment m_{00} and first order moment m_{10} and m_{01} of the PDF:

$$h^{'} = \sum_{\alpha=1}^{n} f_\alpha \quad u^{'}_{i} = \frac{1}{h^{'}} \sum_{\alpha=1}^{n} e_{\alpha i} f_\alpha \quad \alpha = 0, ..., n-1 \tag{3.4}$$

with n=9.
During the collision, update rules are applied at each node. The rules depend only on the state of the probability distribution function (PDF) on the node and are ignorant of other variables in the system. Collision is supposed to observe the given conservation laws, generally for mass and momentum. In fact, m_{00}, m_{10}, m_{01} moments are quantities that do not change during the collision.

3.1.5 Cascaded model

As described in chapter 1, the cascaded model (CaLB) is based on a CO in which, differently from traditional MRT models, *central moments* are relaxed instead than *raw moments*. The central moments can be defined as:

$$\kappa_{\alpha\beta} = \sum_{i,j} \left(i - u^{'}\right)^{\alpha} \left(j - v^{'}\right)^{\beta} f_{ij} \qquad i, j = -1, 0, 1 \tag{3.5}$$

where the sum of α and β indices represents the moment order. The subscripts ij indicate the corresponding components of the velocity vectors of PDF (Miller convention). In the D2Q9 velocities scheme, the equilibrium central moments are given by (Geier, 2006):

$$\begin{cases} \kappa_{00} = h \\ \kappa_{10} = 0 \\ \kappa_{01} = 0 \\ \kappa_{20} = {c_s^{'}}^2 h^{'} \\ \kappa_{02} = {c_s^{'}}^2 h^{'} \\ \kappa_{11} = 0 \\ \kappa_{12} = 0 \\ \kappa_{21} = 0 \\ \kappa_{22} = {c_s^{'}}^4 h^{'} \end{cases} \tag{3.6}$$

where $c_s^{'}$ is the speed of sound. In the CaLB model, the collision is performed by relaxing central moments to their local equilibrium values, separately. As anticipated before in chapter 1, the Galilean invariance is naturally guaranteed. In fact, by definition, central moments can be considered independent of velocity (Geier, 2006).
Regarding the implementation procedure, before the collision, the PDF are transformed into the central moments using the equations in Appendix A; after the collision step, the post-collision central moments are transformed back to PDF. In the collision step, central moments are relaxed following the equations:

$$\kappa_{\alpha\beta}^{pc} = \kappa_{\alpha\beta} - \omega_{\alpha\beta}\left(\kappa_{\alpha\beta} - \kappa_{\alpha\beta}^{eq}\right) \tag{3.7}$$

where $\kappa_{\alpha\beta}^{pc}$ is the post-collision central moment. Following the relation 3.2, the moments that are related to the definition of the value of the transport coefficient ν is κ_{11} and the corresponding central moments obtained from the rotational invariance constraint (Geier, 2006). Then, in order to conserve the isotropy of the model, κ_{20} and κ_{02} are relaxed together:

$$\begin{cases} \kappa_{20+02}^{pc} = \kappa_{20+02} - \omega_{20+02}\left(\kappa_{20} - \kappa_{20}^{eq} + \kappa_{02} - \kappa_{02}^{eq}\right) \\ \kappa_{20-02}^{pc} = \kappa_{20-02}\left(1 - \omega_{20-02}\right) \end{cases} \tag{3.8}$$

The relaxation rates related to the kinematic viscosity are ω_{11} and ω_{20-02}:

$$\omega_{11} = \frac{1}{3\nu' + 0.5} \qquad \omega_{20-02} = \omega_{11} \tag{3.9}$$

Generally, it can be considered that the only relaxation rates that influence the leading order errors are the ones related to the transport parameter, ω_{11} and ω_{20-02}. The relaxation rate ω_{20+02} can be imposed equal to the unity or related to the bulk viscosity. The others are free parameters and can be chosen in the range $\{0, ..., 2\}$ to improve stability; however, they are generally imposed equal to one.

3.1.6 Cumulant model

A brief description of the theory of the cumulants has already been done in section 1.1.1. About practical implementation, in D2Q9 cumulant model (CumLB) the observable quantities relaxed during collision, the cumulants, can be found by means of central moments equations. In fact, cumulants, until third order, are identical to central moments. In particular:

$$\begin{cases} C_{00} = \kappa_{00} \\ C_{10} = \kappa_{10} \\ C_{01} = \kappa_{01} \\ C_{20} = \kappa_{20} \\ C_{02} = \kappa_{02} \\ C_{11} = \kappa_{11} \\ C_{12} = \kappa_{12} \\ C_{21} = \kappa_{21} \end{cases} \tag{3.10}$$

In equations 3.10 the normalization is omitted and it has to be considered that the cumulant of order $a + b$, C_{ab}, is given by: $C_{ab} = c_{ab} \cdot h'$.
Cumulants start to differ from central moments at fourth order. The fourth order cumulants can be derived from central moments by means of the expressions (Geier et al., 2015):

$$C_{22} = \kappa_{22} - \left(\kappa_{20}\,\kappa_{02} + 2{\kappa_{11}}^2\right)/h' \tag{3.11}$$

The collision step is performed in term of cumulants. The equation in Appendix A can be used in CumLB model substituting central moments with

cumulants by means of 3.10 and 3.11 equations; after the collision, the backward transformation in Appendix A is applied, to obtain PDF from cumulants.

3.1.7 Aliasing

In a D2Q9 lattice Boltzmann model the velocity set is reduced to nine velocities, then just nine independents (raw) moments are available to precisely reconstruct the discrete velocity distribution function. In fact, the generic moment can be expressed as:

$$m_{\alpha\beta} = \sum_{i,j} i^{\alpha} j^{\beta} f_{ij} \qquad i,j = -1,0,1 \tag{3.12}$$

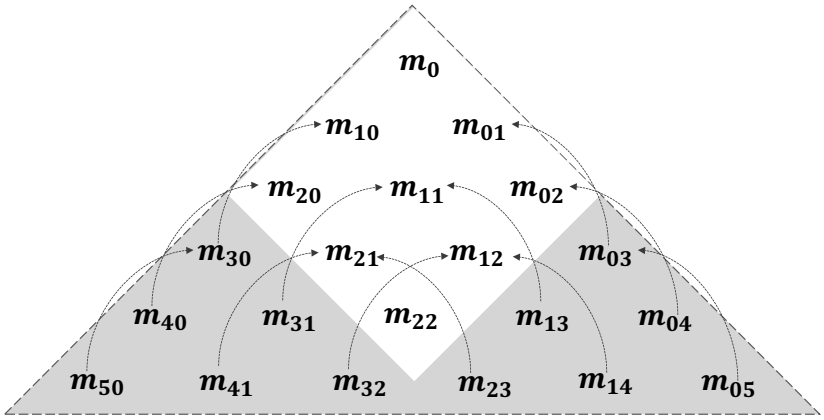

FIGURE 3.2: Dependent and independent moments in D2Q9 model. Higher-order moments (black on light grey) depend on nine lower-order independent moments (black on white). Reproduced from (Krüger et al., 2016).

For example, from such formula derives that $m_{30} = m_{10}$:

$$m_{30} \quad = \quad \sum_{i,j} i^3 f_{ij} \quad = \quad m_{10} \quad = \sum_{i,j} i f_{ij}$$

Moreover, from equation 3.12 it is also possible to say, in the D2Q9 velocity set, that:

$$m_{03} = m_{01} \quad m_{31} = m_{11} \quad m_{13} = m_{11}$$

The non-existence of the moments $m_{30}, m_{03}, m_{31}, m_{13}$ as independent moments and their coincidence with lower order moments is known as aliasing.

From the theory of cumulants (Geier et al., 2015), the non-conserved cumulants are equal to zero in the equilibrium. Then, the definition of cumulants in section 1.1.1 helps in computing the equilibrium of moments. This value could also be traditionally calculated using the Taylor expansion of the Maxwell-Boltzmann distribution up to second order in the Mach number (Chen and Doolen, 1998). The third order equilibrium moment m_{30} is:

$$m_{30} = \left(3 \cdot {c_s^{'}}^2 \cdot u^{'} + {u^{'}}^3\right) h^{'} \tag{3.13}$$

If the normalized value of m_{30} is considered and the high order term ${u^{'}}^3$ is neglected, the moment m_{30} becomes:

$$m_{30} = 3 \cdot {c_s^{'}}^2 m_{10} \tag{3.14}$$

but m_{30} should be equal to m_{10} in order to respect the aliasing in relation 3.14.

3.1.8 Difference between conventional and innovative model

In the last section, the relation 3.14 explains why, in usual lattice Boltzmann models, the speed of sound is considered constant and equal to $\frac{1}{3}$.
However, in the shallow water model, the speed of sound is not constant but variable with the water depth. Anyway, the relation 3.14 has to be respected. This problem can be solved in two different way.
The first solution could be the one adopted in cascaded/cumulant model; i.e. in these models, the speed of sound square is ${c_s^{'}}^2 = \frac{g^{'}h^{'}}{2}$ and this expression enters in the definition of the central moments/cumulants of equilibrium. Moreover, it has to be pointed out that, in the collision step, the relaxation rate of 2nd order central moments/cumulants are adjusted in order to conserve the isotropy during the collision, in such a way:

$$\omega_{11} = \left(\frac{2}{3g^{'}h^{'}}\left(\frac{1}{\omega} - \frac{1}{2}\right) + \frac{1}{2}\right)^{-1} \tag{3.15}$$

and

$$\omega_{20-02} = \left(\frac{\frac{2}{3}\left(\frac{1}{\omega} - \frac{1}{2}\right)}{1 - \frac{g^{'}h^{'}}{2}} + \frac{1}{2}\right)^{-1} \tag{3.16}$$

where the relaxation rate ω is related to the actual viscosity of the fluid (section 3.1.3).
On the other hand, in the conventional SRT model (section 2.1.2), the speed

of sound is decoupled from the third order moment m_{30}. As a result, this model uses a speed of sound square different from $\frac{g^{'}h^{'}}{2}$ in the diffusion process. This can be evinced observing the equilibrium equations of conventional SW model, where the part related to the viscosity appears equal to the one in the standard two dimensional lattice Boltzmann model, whereas the part related to the density is different and takes into account the dependency of the speed of sound from the water depth. This observation appears clear if the EDF shown in section 2.1.2, for $\alpha = 1, ..., 8$, is written in the following form:

$$f_{\beta}^{eq} = \beta h \left(\frac{c_s^{'2}}{3} + \frac{1}{3} \left(e_{\alpha} \cdot \mathbf{u}^{'} \right) + \frac{1}{2} \left(e_{\alpha} \cdot \mathbf{u}^{'} \right)^2 - \frac{1}{6} \mathbf{u}^{'} \cdot \mathbf{u}^{'} \right) \tag{3.17}$$

where $\mathbf{u}^{'}$ is the velocity of the fluid $\mathbf{u}^{'} = [u^{'}, v^{'}]$.

3.1.9 Improvement of the isotropy in cumulant model

In chapter 6, it will be shown that it is advantageous to consider, during the collision step, both the cumulant model and the model of De Rosis, briefly described in section 2.1.2. Hence, it becomes possible to take advantage of the positive features of each model.
In De Rosis model, the 3th order cumulant occurs as follows:

$$c_{21}^{DeRosis} = \frac{1}{3} h^{'} v^{'} - \frac{h^{'2} g^{'}}{2} v^{'}$$

whereas in the cumulant model it is approximately equal to zero.

$$c_{21}^{cum} \cong 0$$

Then, the different contribution of the two model can be considered in the collision step introducing, in the cumulant model, the following value of the equilibrium 3th order cumulant:

$$c_{21}^{*} = c_{21}^{cum} + K c_{21}^{DeRosis} \tag{3.18}$$

where K is a constant, variable between 0 and 1 (i.e. if K is equal to 0 the model of De Rosis is not considered). In section 3.1.8, it was explained that,

in cumulant/cascaded model, the isotropy of the model is restored by introducing in the relaxation rates related to the transport parameter the dependency on the speed of sound ${c_s^{'}}^2 = \frac{g^{'}h^{'}}{2}$.
If the rule 3.18 is applied in the collision, the actual speed of sound is changed in:

$$ {c_s^{'}}^2 = \frac{g^{'}h^{'}}{2} + K\left(\frac{1}{3} - \frac{g^{'}h^{'}}{2}\right) \tag{3.19} $$

and, consequently, the relaxation rates ω_{11} in equation 3.15 and ω_{20-02} in equation 3.16 are changed using the value of the speed of sound in equation 3.19. The resulting relaxation rates are:

$$ \omega_{11} = \left(\frac{1}{3\left(\frac{g^{'}h^{'}}{2} + K\left(\frac{1}{3} - \frac{g^{'}h^{'}}{2}\right)\right)}\left(\frac{1}{\omega} - \frac{1}{2}\right) + \frac{1}{2}\right)^{-1} \tag{3.20} $$

$$ \omega_{20-02} = \left(\frac{\frac{2}{3}\left(\frac{1}{\omega} - \frac{1}{2}\right)}{1 - \left(\frac{g^{'}h^{'}}{2} + K\left(\frac{1}{3} - \frac{g^{'}h^{'}}{2}\right)\right)} + \frac{1}{2}\right)^{-1} \tag{3.21} $$

3.2 Evaluation of the force term

Zhou (Zhou, 2004) has successfully demonstrated that the approach of adding the external force to the streaming step (section 1.4) is a simple and general method in BGK LBM and it represents the underlying physics, producing accurate solutions to many flows.
In our non-conventional models (CumLB and CaLB), the presence of the external force has been taken into account also in the transformation from distribution to central moments/cumulants and vice-versa. In this regard, the macroscopic variables h, u, v in the equations in Appendix A are modified using the following relations (Geier et al., 2015):

$$ h^{'} = \sum_{\alpha=1}^{n} f_\alpha \quad {u_i}^{'} = \frac{\sum_{\alpha=1}^{n} e_{\alpha i} f_\alpha}{h^{'}} + \frac{{F_i}^{'}}{2h^{'}} \tag{3.22} $$

The equations to be considered for the transformation from PDF into central moments/cumulants and vice versa are shown in Appendix B.

3.2.1 Computation of the weights

The weights state the mass distribution in a force. The weights can be obtained by EDF from cumulants shown in Appendix A, imposing the velocities (u, v) equal to zero (absolute equilibrium):

$$f_\alpha = \begin{cases} \frac{1}{9}(h^{'} - 3)^2 h^{'} & \alpha = 0 \\ -\frac{1}{18}(h^{'} - 3) h^{'\,2} & \alpha = 1,2,3,4 \\ \frac{h^{'\,3}}{36} & \alpha = 5,6,7,8 \end{cases} \tag{3.23}$$

Then, the previous equation are normalized in order to have the sum along the x direction or y direction equal to 1. The reticular weights become:

$$w_\alpha = \begin{cases} \frac{1}{3h^{'}}\left(-3 + h^{'}\right)^2 & \alpha = 0 \\ -\frac{1}{6}\left(-3 + h^{'}\right) & \alpha = 1,2,3,4 \\ \frac{h^{'}}{12} & \alpha = 5,6,7,8 \end{cases} \tag{3.24}$$

Actually, the sum of the weights along the x direction or along the y direction is equal to 1:

$$4 \cdot \frac{h^{'}}{12} - 2 \cdot \frac{1}{6} \cdot \left(h^{'} - 3\right) = 1$$

Then, the external force in the x direction can be expressed as:

$$F^{'}{}_{\alpha x} = w_\alpha \left(F^{'}{}_x e_\alpha\right) \tag{3.25}$$

where w_α represent the reticular weight in equations 3.24. An analogous expression can be used for the force along the y direction.

3.3 Boundary conditions

The standard boundary conditions (BC) used in this work (periodic BC, no-slip BC) have been already synthetically described in chapter 1, paragraph 1.5.

About inlet/outlet boundaries, hereafter the boundary conditions originally derived for the innovative models are explained. In particular, in the paragraph, the derivation and implementation of Zou-He BC are reported. Moreover, non-reflecting outlet BC are compared with Zou-He BC, in order to put in evidence the decrease of wave reflection using the non-reflecting BC (paragraph 3.3.3).

3.3.1 Zou-He BC: derivation and implementation

The Zou-He (Zou and He, 1997) boundary condition is often used for modelling i/oBC. These i/oBC are based on the bounce-back of the non equilibrium part of the distribution function. The scheme hereinafter described is adapted to the equilibrium of the innovative models described in sections 3.1.5 and 3.1.6. For the standard implementation of Zou-He BC refers to (Zhou, 2004).
In a straight channel of length L, we want to impose the discharge at the inlet section (q_{in}) and a constant water depth (h_{out}) at the outlet section. Without loss of generality, it can be assumed that the velocity u (velocity along the direction of the channel) is equal to zero at $x = 0$ and $x = L$. After the streaming step, the unknown distribution functions at boundaries can be determined from the conservation equations of mass and momentum and from the bounce-back rule for the non-equilibrium part:

$$f_1 - f_1^{eq} = f_3 - f_3^{eq} \quad at \quad x = 0$$

$$f_3 - f_3^{eq} = f_1 - f_1^{eq} \qquad at \quad x = L$$

In detail, the following equations are used at the inlet for the unknown distributions f_1, f_5, f_8 (Figure 3.3), with the discharge $q^{'} = h^{'}u^{'}$, defined by the initial conditions:

$$f_1 = \frac{1}{2}\left(2h^{'}u^{'} - g^{'}\left(h^2u^{'}\right) + 2f_3\right)$$

$$f_5 = \frac{1}{4}\left(g(h^{'2}u^{'}) - 2f_2 + 2f_4 + 4f_7\right)$$

$$f_8 = \frac{1}{4}(g(h^{'2}u^{'}) + 2f_2 - 2f_4 + 4f_6)$$

At the outflow, the distributions f_3, f_6, f_7 are:

$$f_3 = \frac{1}{2}\left(-2hu^{'} + g^{'}\left(h^{'2}u^{'}\right) + 2f_1\right)$$

$$f_6 = \frac{1}{4}\left(-g^{'}(h^2u^{'}) + 2f_2 + 2f_4 + 4f_8\right)$$

$$f_7 = \frac{1}{4}(-g^{'}(h^{'2}u^{'}) + 2f_2 - 2f_4 + 4f_5)$$

where $h^{'} = h^{'}{}_{out}$ and the value of velocity u is derived from the equation:

$$u^{'}{}_{out} = \frac{(f_0 + f_4 + f_2 + 2(f_1 + f_5 + f_8))}{h^{'}} - 1$$

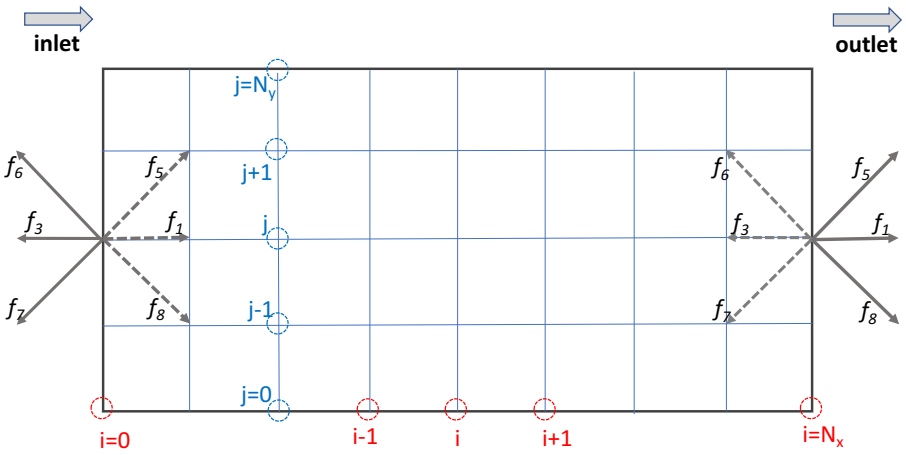

FIGURE 3.3: Distribution functions at inlet and outlet nodes. The dashed lines denote the unknown distributions.

3.3.2 Inflow/outflow BC based on velocity

The i/oBC hereinafter described is based on the bounce-back principle. The equations are derived from the ones in (Geier et al., 2015) with the simplification that the wall is always located at the nodes of the grid and the interpolation is not necessary. For example, at the inlet, directly using the post-collision state of the distributions (indicated by an asterisk), the f_α entering into the domain (see Figure 3.3) can be found using the equations 3.26, 3.27, 3.28:

$$f_{\bar{1}}[0,j] = f_3^*[0,j] - 6 \cdot w_3 \cdot u^{'} \cdot h^{'} \tag{3.26}$$

$$f_{\bar{5}}[0,j] = f_7^*[0,j] - 6 \cdot w_7 \cdot u^{'} \cdot h^{'} \tag{3.27}$$

$$f_{\bar{8}}[0,j] = f_6^*[0,j] - 6 \cdot w_6 \cdot u^{'} \cdot h^{'} \tag{3.28}$$

where the w_α are the weights as defined in section 3.2.1, $u^{'}$ is the velocity at the inlet and $h^{'}$ the imposed depth in order to have a flux equal to $q = h^{'}u^{'}$. Similarly, an OBC at the outlet can be obtained.

3.3.3 Non-reflecting outlet boundary conditions

At the outflow of the domain a traditional strategy is to use an extrapolation boundary condition. The extrapolation replaces the distributions that enter into the domain with those ones from the node close to the outlet. For example, considering the x direction:

$$f_1\left[i,j\right] = f_1\left[i-1,j\right] \tag{3.29}$$

However, this method introduces acoustic reflections. To decrease this effect non-reflecting BC (NRBC) can be used. NRBC let waves propagate smoothly out of the system without being reflected back. Geier (Geier et al., 2015) introduced NRBC based on a linear interpolation between the distributions at the outlet and the distributions from where the pressure wave came from :

$$f_1\left[i,j\right](t) = f_1\left[i-1,j\right](t'-\Delta t)(c_s^{'1/2} - u^{'}) + f_1\left[i,j\right](t'-\Delta t)(1-(c_s^{'1/2} - u^{'})) \tag{3.30}$$

where $c_s^{'}$ is the speed of sound and $u^{'}$ is the velocity at the outlet. The different behaviour of the two BC at outlet can be explained by means of the Figure 3. The simulation was run in a channel 25 m long with slip-BC at wall with τ=0.8, Δx=0.01 m, Δt=0.001 s. At the inlet, the magnitude of the velocity is 1.5 m/s. The difference between the reflection of the two velocity wave is substantial. In fact, the Zou-He BC are characterized by a strong reflection and the value of the wave increases almost two times; on the other hand, the NRBS present a reflection essentially not significant.

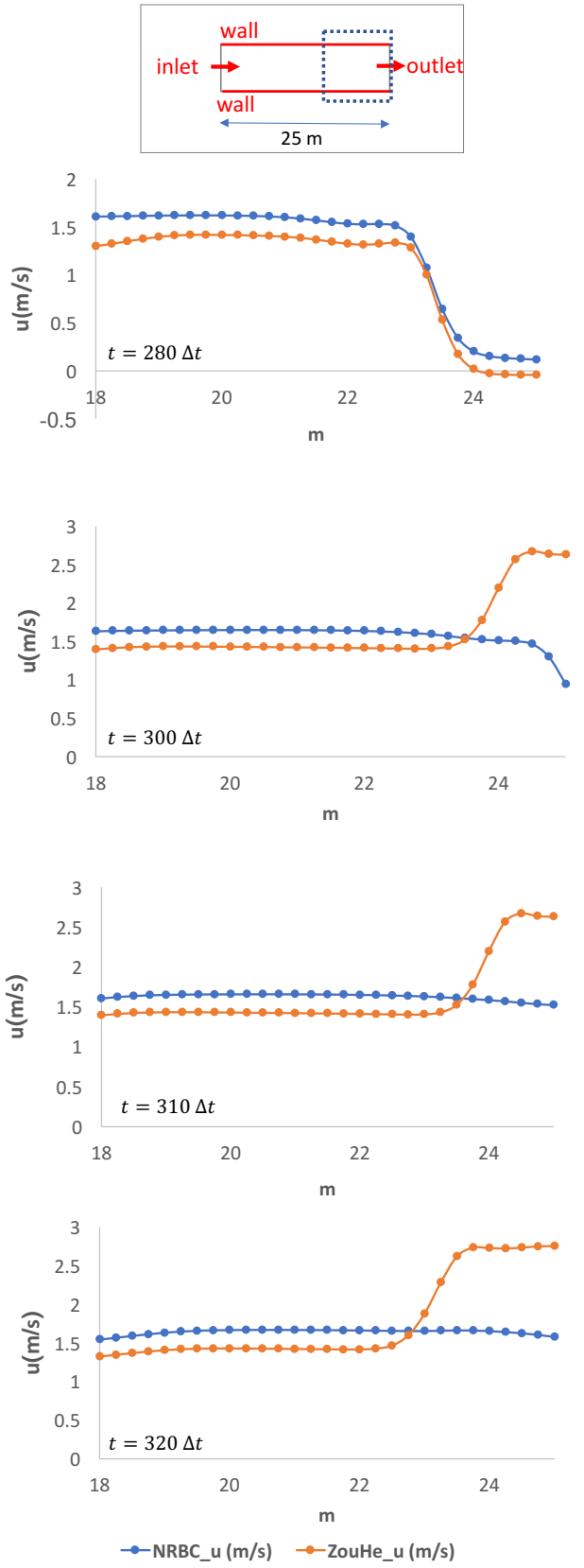

FIGURE 3.4: Evolution of a velocity wave through different times. At the outlet, the difference in velocity reflection between Zou-He BC and NRBC. At the top of the page, the simulation setup. The dashed line shows the channel part taken into consideration in the graphs.

Chapter 4

Convergence study

4.1 Introduction

The accuracy of a numerical simulation allows to understand the sensitivity of the solution to the parameters of the model. We can also evaluate the code implementation, e.g., identifying code mistakes or inconsistencies in the theoretical and numerical algorithm. Generally, the validation and verification of the code are essential topics in computational fluid dynamic (Christopher J.Roy, 2005).

4.2 Diffusive scaling

The convergence of the simulation towards the solution is related to the analysis of the accuracy of the model. The truncation error of a discretization scheme defines the accuracy of a numerical model. The accuracy must increase when the time step (Δt) and the grid spacing (Δx) decrease. The *order of accuracy* can be interpreted as the rate of the decreasing of the discretization error when the grid spacing and time step decrease.
In our case, the error has been measured using the *diffusive scaling*. It means that the time step scales proportionally to the square of the grid spacing $(\Delta t \propto \Delta x^2)$. The setting allows to keep constant the value of the Reynold number and the value of the Mach number low, in order to maintain the simulation in the incompressible limit of the Navier Stokes equations.

4.3 Accuracy evaluation

The measure of the accuracy of a model can be done through different approaches. It can be used an "intrinsic" measure of the error, evaluating the transport parameter of the model (viscosity) and the phase lag; on the other

hand, the quantification of the error can take place comparing the results (i.e. velocity values) with the analytical solution.

4.3.1 Error in viscosity

The asymptotic behaviour of the numerical viscosity ν_n is determined by fitting the logarithm of Fast Fourier Transform (FFT) of the amplitude of the wave to a linear function. The slope is related to the numerical viscosity through the square of the wave vector. The normalized error of the viscosity $ER\nu$, with respect to the theoretical viscosity $\nu = c_s^2 \left(\tau - \frac{1}{2}\right) \frac{\Delta x^2}{\Delta t}$, is defined as: $ER_\nu = |\nu_n - \nu|/\nu$.

4.3.2 Error in phase

The phase lag can be considered a measure of the level of Galilean invariance in the model. In order to test the level of Galilean invariance, the phase lag ER_Φ is calculated every turn, when the wave comes back to its original position. Once the stability of the simulation has been reached, the phase lag is measured by the difference in phase between a wave turn over time and the previous.

4.3.3 Comparison with the analytical solution

In order to quantify the error in comparison with the analytical results, the relative error norms $L_\infty\, L_1\, L_2$ can be used. Given the analytic value, for example the x-axis velocity u_a, function of space and time, and its numerical equivalent u_n, we define the error norms as:

$$\|err\|_{L_\infty} = \frac{max\, \|u_n(x,t) - u_a(x,t)\|}{max\, \|u_n(x,t)\|}$$

$$\|err\|_{L^1} = \frac{\sum_x \|u_n(x,t) - u_a(x,t)\|}{\sum_x \|u_n(x,t)\|}$$

$$\|err\|_{L^2} = \frac{\sqrt{\sum_x \|u_n(x,t) - u_a(x,t)\|^2}}{\sqrt{\sum_x \|u_n(x,t)\|^2}}$$

The sums are defined over the whole spatial domain, where u is determined. Generally, the L_2 norm is preferred. An advantage of this definition is that local errors cannot cancel each other and the error remains conditioned by any deviation from the analytical value (Krüger et al., 2016).

4.4 Shear wave test

In the shear wave test, the asymptotic behaviour in diffusive scaling ($\Delta t \propto \Delta x^2$) of a one dimensional decaying shear wave is investigated. The dimensions of the domain are $L \times 3$ nodes, with L varying from 32 to 256 nodes; the boundary conditions are periodic. The simulation was run for $20000(L/L_0)^2$ time steps and the FFT of the wave amplitude was measured every $1000(L/L_0)^2$ time steps. In order to avoid any influence of the initial conditions on the asymptotic decay, the values of viscosity and phase were measured after $10000(L/L_0)^2$ time steps.
The initial conditions are given by:

$$u^{'}(t=0) = u_0^{'}\frac{L_0}{L} \qquad v^{'}(t=0) = v_0^{'}\frac{L_0}{L}\sin\frac{2\pi x}{L}$$

with $L_0 = 32$, $u_0^{'} = 0.01$ and $v_0^{'} = 0.1$. All the quantities are expressed in lattice units (l.u.). The physical values of the aforementioned quantities are: $L_0\Delta x$, $u_0^{'}(\Delta x/\Delta t)$, $v_0^{'}(\Delta x/\Delta t)$, with $\Delta x = 1$m and Δt given by the relation 2.13.
The analytic solution is:

$$v^{'}(t) = v_0^{'}\frac{L_0}{L}\sin\frac{2\pi x}{L}e^{-\nu^{'}t\left(\frac{2\pi}{L}\right)^2}$$

where x and t are expressed in l.u. Hereafter, the results of the CumLB and BGK SW models are shown. In such one-dimensional simulation, the error in viscosity and in phase for the cascaded and cumulant models are basically very similar. Hence, results of cascaded model are not shown.
To adopt the diffusive scaling, the velocity has to be scaled with L/L_0 and the sampling interval is $K(L/L_0)^2$, $K = 1000$; K is a constant value, suitable to define a sampling interval that allows to measure of the viscosity before the decay of the wave.
The error in viscosity in CumLB model is comparable with the one of BGK model. For example, with $\nu^{'} = 0.01$ and $h^{'} = 1$, in CumLB model the normalized error in viscosity is 0.00284 for $L = 32$ nodes and 0.0000443 for $L = 256$ nodes. In BGK SW model, it is generally slightly higher, 0.0029 for $L = 32$ nodes and 0.0000453 for $L = 256$ nodes. Anyway, all the models show a second order accuracy with the increase of the resolution.
The error in phase (phase lag) is measured when the wave comes back to its original position. The number of time steps in which the wave turns is equal

to $u_0^{'}\frac{L_0}{L}$. The error in phase shows a fourth order accuracy. It should be clarified that a fourth order phase lag is due to the alignment of the wave with the grid and that, in general, the method is second order accurate (Geier et al., 2015). The value of the phase lag is similar in CumLB and BGK SW model. Results related to different depths are not shown. It is preferred to go forward with the two dimensional case of Taylor Green vortex text that results more significant. In fact, it allows to take into consideration, in a non-symmetric domain, the results of a simulation where the main directions of the motion are not aligned with the axes.

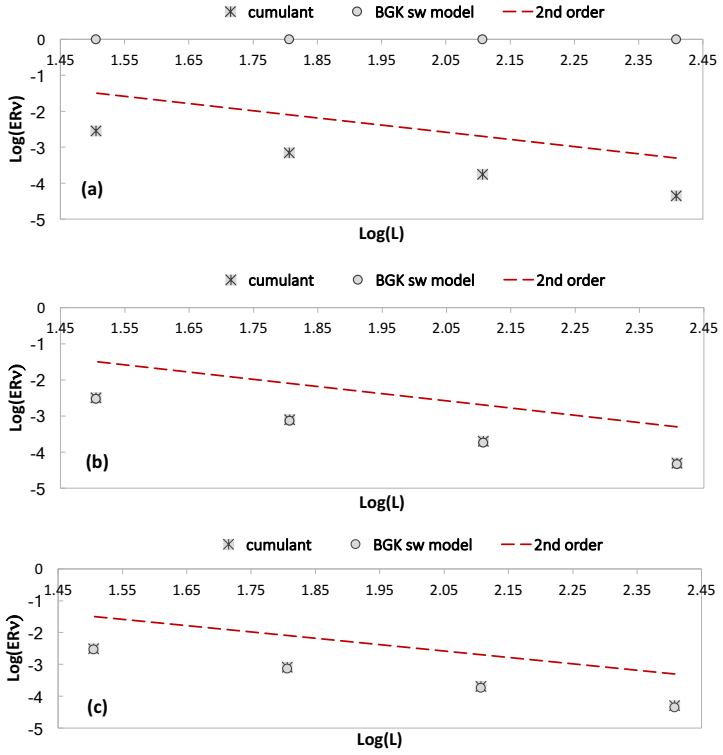

FIGURE 4.1: Comparison of normalized error in viscosity ER_ν, for the three viscosities: $\nu^{'} = 0.01(a)$, $\nu^{'} = 0.001(b)$, $\nu^{'} = 0.0001(c)$ (l.u).

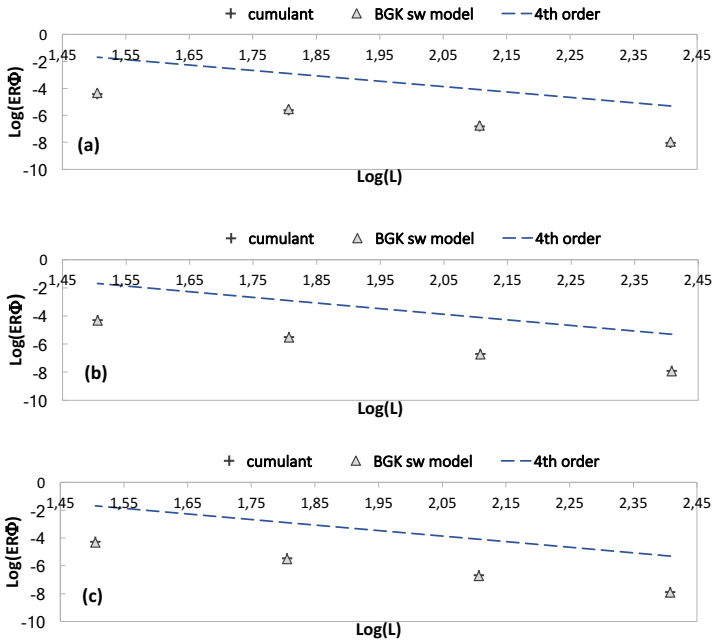

FIGURE 4.2: Comparison of error in phase ER_Φ, for the three viscosities: $\nu^{'} = 0.01(a)$, $\nu^{'} = 0.001(b)$, $\nu^{'} = 0.0001(c)$ (l.u).

4.5 Taylor Green vortex test

The decay of a Taylor Green vortex in a fully periodic domain is here investigated, to assess the accuracy of the transport coefficient (viscosity) and the phase lag. The length of the computational domain in lattice units is L, with L equal to 32, 64, 128, 256 nodes, the width W is equal, respectively, to 48, 96, 192 and 384 nodes. Hence, the components of the wave vectors are:

$$k_x = \frac{2\pi}{L} \qquad k_y = \frac{4\pi}{3L} \qquad \frac{k_x}{k_y} = \frac{3}{2} \tag{4.1}$$

The difference in the dimensions of the domain $(L \neq W)$ allows to check possible defects in the isotropy of the model and the presence of (eventual) preferential directions.
At the beginning of the simulation, the value of the velocity, along the x - axis and y - axis, and the value of the depth, are respectively:

$$u^{'} = u_0^{'}\frac{L_0}{L} - U^{'}\frac{L_0}{L}\sqrt{\frac{k_y}{k_x}}cos\,(k_x x)\,sin\,(k_y y) \tag{4.2}$$

$$v^{'} = U^{'} \frac{L_0}{L} \sqrt{\frac{k_x}{k_y}} sin\left(k_x x\right) cos\left(k_y y\right) \tag{4.3}$$

$$h^{'} = h_0^{'} \left(1 - \frac{\left(U^{'\,2} \frac{L_0^2}{L^2} \right)}{4 c_s^{'\,2}} \left(\frac{k_y}{k_x} cos\left(2k_x x\right) + \frac{k_x}{k_y} sin\left(2k_y y\right) \right) \right) \tag{4.4}$$

where x and y are expressed in lattice units; $L_0 = 32$, $u_0^{'}$ and $U^{'}$ that depend on the chosen velocity set. The slow set expressed in physical units is $u_0^{'} = 0.01\ \Delta x/\Delta t$ and $U^{'} = 0.00035\ \Delta x/\Delta t$; the fast set is: $u_0^{'} = 0.096\ \Delta x/\Delta t$ and $U^{'} = 0.0035\ \Delta x/\Delta t$. The viscosity is $\nu^{'} = c_s^{'\,2} \left(\tau - 1/2\right) \frac{\Delta x^2}{\Delta t}$. The value of the grid spacing is $\Delta x = 1$ m; the value of Δt is given by the formula 2.13.
The value of the analytic solution of the velocity of the wave along the y-axis is given by:

$$U^{'} \frac{L_0}{L} \sqrt{\frac{k_x}{k_y}} sin\left(k_x x\right) cos\left(k_y y\right) e^{\frac{t}{t_D}} \tag{4.5}$$

where t_D (decay time of the wave) is equal to:

$$t_D = \frac{1}{\nu^{'} \left(k_x^2 + k_y^2 \right)} \tag{4.6}$$

whith x and y and t expressed in lattice units. The aforementioned initial conditions are set as in (Krüger, Varnik, and Raabe, 2010), with the difference that our domain is not symmetric.
Simulations are run with viscosities $\nu^{'} = 0.01, 0.001, 0.0001$ and different depths $h^{'} = 1, 0.5, 0.1$.
As in the shear wave test, the simulation setup is performed in order to use the diffusive scaling. Then, velocities and times are always multiplied by a factor, respectively, $\frac{L_0}{L}$ and $\left(\frac{L_0}{L}\right)^2$. It is noteworthy that the asymptotic behaviour of the viscosity of the different models has been compared for various depths of the water h; the reason of such kind of study can be explained with the fact that in shallow water models, the speed of sound changes with the depth (Dellar, 2002); then, it becomes important to analyze the behaviour of the model in relation to the value of the water depth (section 3.1.2).

4.5.1 Error in viscosity

In this section, a comparison between the normalized error in viscosity in three different models is performed: CumLB, CaLB and BGK SW model. In particular, the comparison takes into consideration different viscosities and depths.
In the next figures, the x-axis shows the logarithm of the number of nodes along the x-directions of the domain; the y-axis shows the logarithm of the normalized error of viscosity. Moreover, it is important to clarify that the BGK SW model becomes unstable for a value of $h^{'}$ equal to 1.0, for all the viscosities ($\nu^{'} = 0.01, 0.001, 0.0001$) considered in this section. In section 4.5.3, the conditions under which this model becomes stable, for $h^{'} = 1$, will be clarified. Then, it can be noted that the error in viscosity for cumulant and cascaded models is generally comparable (Geier, Pasquali, and Schönherr, 2017), for all the values of $h^{'}$.

Slow velocity set

For $h^{'} = 1$, in CumLB and CaLB model, the trend of the slope of viscosity error is in between second order and third order accuracy; i.e., in CumLB model, $\nu^{'} = 0.01$, the slope is about -2.35 (Figure 4.3, 4.4 and 4.5); but, it becomes constantly equal to -2 for lower values of the depth. The BGK SW model is characterized, for $h^{'} = 0.1$, by a relative viscosity error much lower than cumulant and cascaded models; for example, if $h^{'} = 0.1$ and $\nu^{'} = 0.01$, $L = 32$, $ER_{\nu} = 0.00049$ for the BGK model and 0.0017 for cumulant/cascaded model (Figure 4.3).

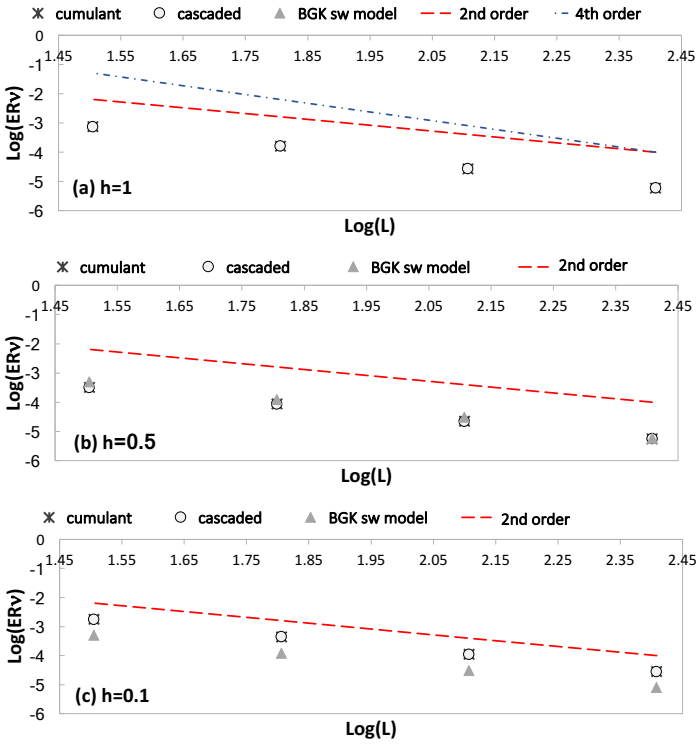

FIGURE 4.3: Slow velocity set - comparison of normalized error in viscosity ER_ν, for the three depths: $h^{'} = 1(a), 0.5(b), 0.1(c)$ - $\nu^{'} = 0.01$.

In Figure 4.4, it should be noted that results for CumLB and CaLB models, for $h^{'}$ = 0.5 and $\nu^{'}$ = 0.001, are characterized by a non uniform slope for a number of nodes equal to L = 64 nodes.
The BGK SW method, if stable, is always characterized by a slope trend equal about to -2.0 and by an accuracy higher than cascaded and cumulant model. It should be noted that, generally, in cumulant and cascaded models the error in viscosity increases with the reduction of viscosity, as it has already been noted in (Geier et al., 2015). On the other hand, the viscosity error in the BGK model changes in a limited manner with the reduction of the viscosity. If $h^{'}$ = 0.1 and $\nu^{'}$ = 0.0001 (Figure 4.5), the CumLB shows an accuracy higher than CaLB model and a slope of the trend higher than -2.

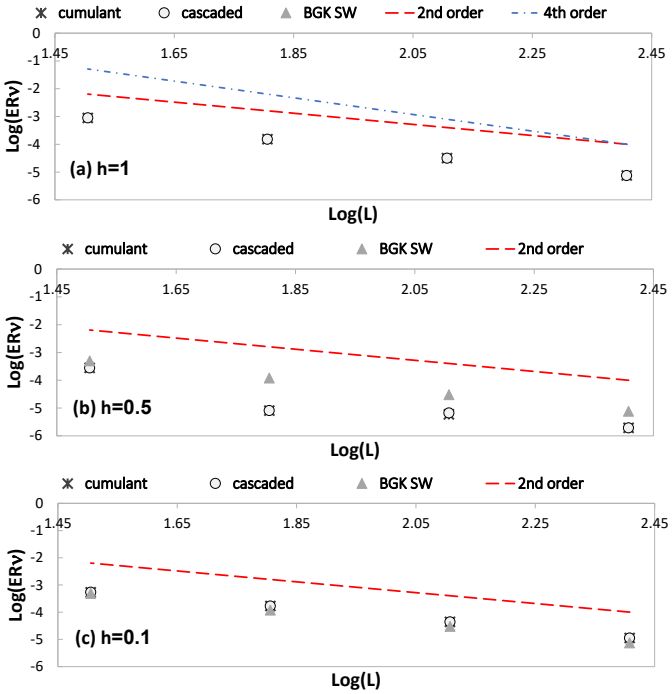

FIGURE 4.4: Slow velocity set - comparison of normalized error in viscosity ER_ν, for the three depths: $h^{'} = 1(a), 0.5(b), 0.1(c)$ - $\nu^{'} = 0.001$.

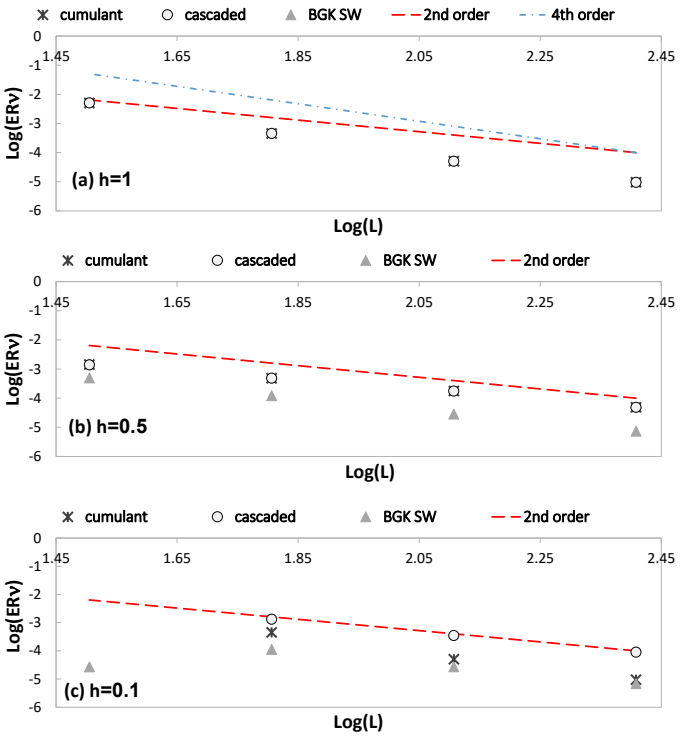

FIGURE 4.5: Slow velocity set - comparison of error in viscosity ER_ν, for the three depths: $h^{'} = 1(a), 0.5(b), 0.1(c)$ - $\nu^{'} = 0.0001$.

Fast velocity set

Simulations performed with a fast velocity set are characterized by some cases missing due to instability; in fact, with a viscosity $\nu^{'} = 0.001$ the case with $h^{'} = 1$ is missing (Figure 4.7) ; with $\nu^{'} = 0.0001$ it was possible to simulate only for a depth value $h^{'} = 0.5$ (Figure 4.8).
For $h^{'} = 1$, in CumLB and CaLB model, the trend of the slope of viscosity error is higher than second order accuracy; for example, in CumLB model, $\nu^{'} = 0.01$, the slope is about -2.2 (Figure 4.6).
Results are characterized, for all the models, by a viscosity error much higher than for the slow set, as it should be expected. For example, taking into consideration the results of CumLB for viscosity $\nu^{'} = 0.01$ and $h^{'} = 1.0$, an increment in the fast set of translational velocity $u_0^{'}$ and of the amplitude of the velocity of the wave $U^{'}$ of about tenth times, leads to a medium increase, for different domain size, of the error of forty times (for comparison, Figure 4.3 and 4.6). Nevertheless, it has to be pointed out that for a simulation that remain always stable, we are speaking about errors that are low and that assume a maximum value of 0.015% for CumLB/CaLB model and 0.02% for BGK SW model.

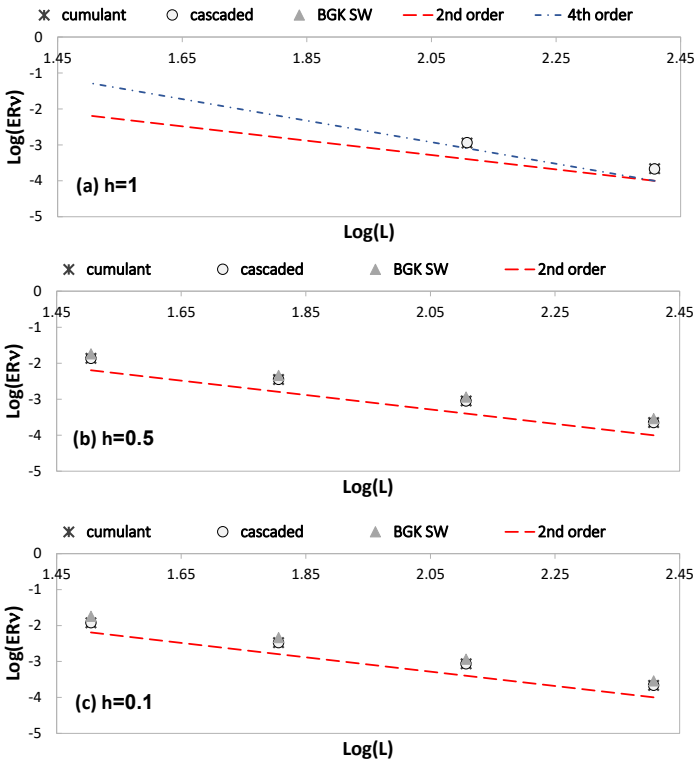

FIGURE 4.6: Fast velocity set - comparison of normalized error in viscosity ER_ν, for the three depths: $h^{'} = 1(a), 0.5(b), 0.1(c)$ - $\nu^{'} = 0.01$.

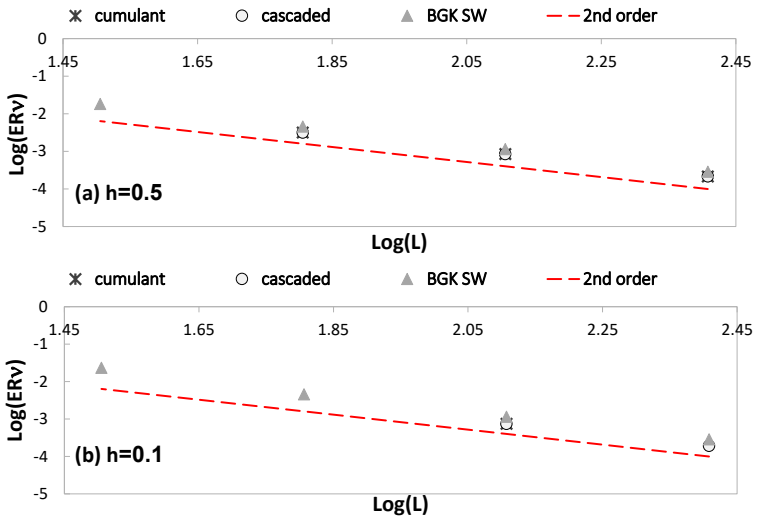

FIGURE 4.7: Fast velocity set - comparison of normalized error in viscosity ER_ν, for the depths: $h^{'} = 0.5(a), 0.1(b)$ - $\nu^{'} = 0.001$.

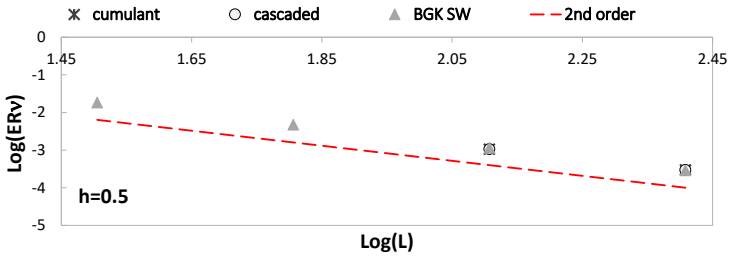

FIGURE 4.8: Fast velocity set - comparison of normalized error in viscosity ER_ν, for the three depths: $h^{'} = 0.5$ - $\nu^{'} = 0.0001$.

4.5.2 Phase lag measure

In this section, a comparison between the error in phase in three different models is performed: CumLB, CaLB and BGK SW model, taking into consideration different viscosities and depths. In the next graphs, the x-axis shows the logarithm of the number of nodes along the x-directions of the domain; the y-axis shows the logarithm of the phase lag.

Slow velocity set

In all the models that have been examined, the error in phase is defined by a slope of the trend equal to -2, as generally expected in lattice Boltzmann models. As observed in the previous section 4.5.1, the instability that characterizes the BGK model for depths between 0.5 and 1.0, does not allow to have measures in such case. At slow velocities, for CumLB and CaLB model, the

error in phase looks to be conditioned by viscosity values: it increases if the viscosity decreases. i.e., the percentual difference between the error for the viscosities $\nu^{'} = 0.01$ and $\nu^{'} = 0.0001$ is about 2.5% for $h^{'} = 1$ and about 40% for $h^{'} = 0.1$ (see Figure 4.9 and 4.11 for comparison). On the other hand, the BGK model is characterized by an error in phase less variable with the depth of the water (for example, it is observable in Figure 4.9). Similar observations can be done for lower viscosities (see Figures 4.10 and 4.11). For $h^{'} = 0.1$, viscosity $\nu^{'} = 0.0001$ and $L = 32$, the cascaded / cumulant models are not stable. (Figure 4.11).

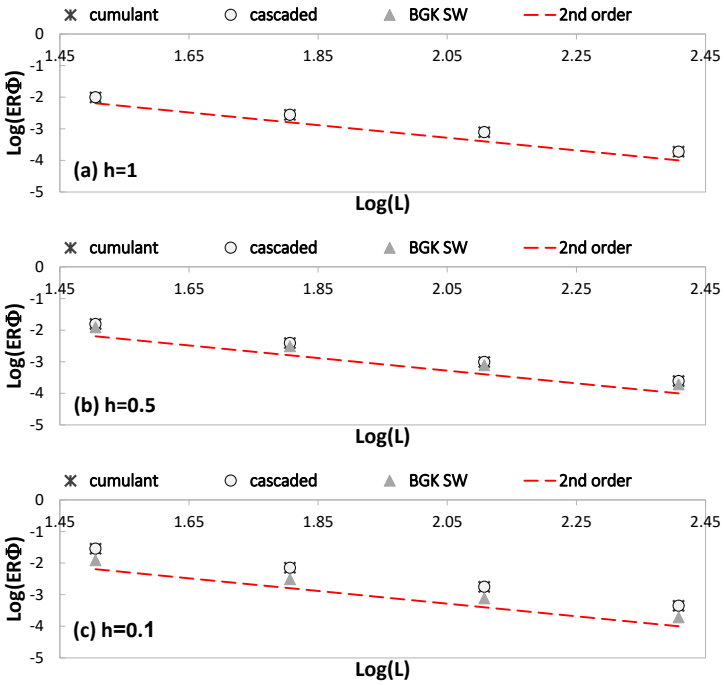

FIGURE 4.9: Slow velocity set - phase lag ER_{Φ}, for the three depths: $h^{'} = 1.0$, $h^{'} = 0.5$, $h^{'} = 0.1$ - $\nu^{'} = 0.01$.

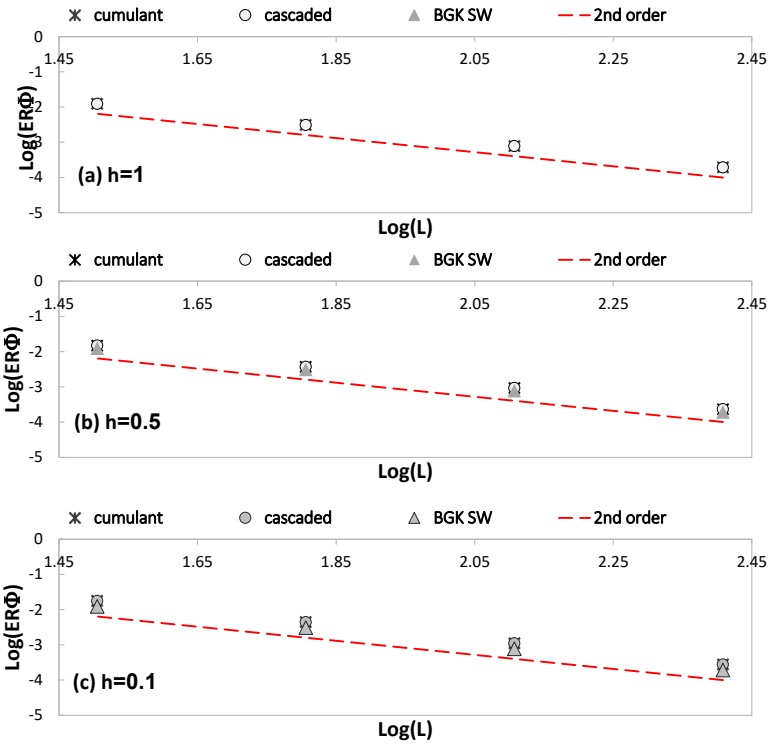

FIGURE 4.10: Slow velocity set - phase lag ER_Φ, for the three depths: $h^{'} = 1.0$, $h^{'} = 0.5$, $h^{'} = 0.1$ - $\nu^{'} = 0.001$.

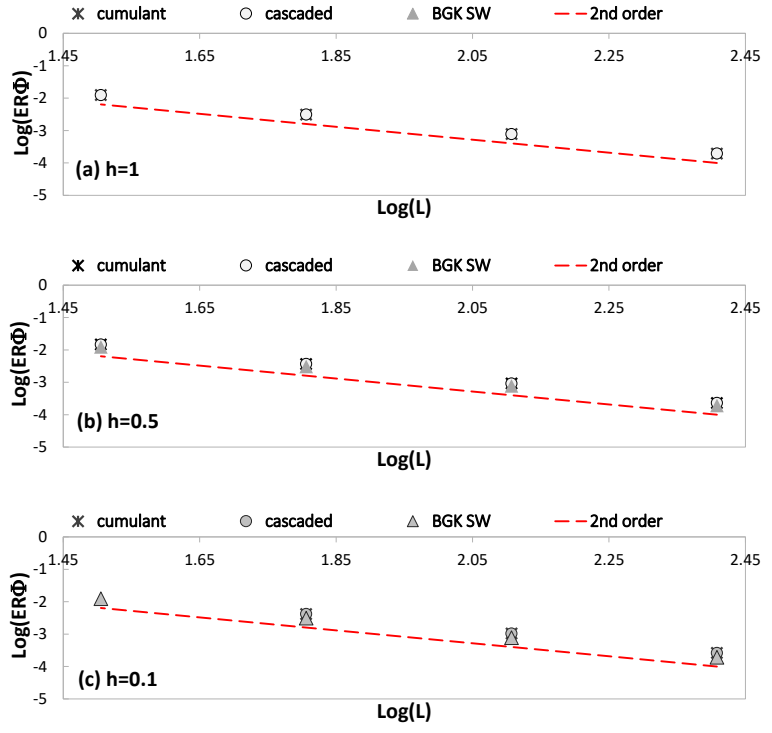

FIGURE 4.11: Slow velocity set - phase lag ER_Φ, for the three depths: $h^{'} = 1.0$, $h^{'} = 0.5$, $h^{'} = 0.1$ - $\nu^{'} = 0.0001$.

Fast velocity set

In all the models, the error in phase increases with the velocity. For example, in CumLB/CaLB models, the phase lag grows in percentage, adopting the fast set of velocities instead of the slow set, of about 0.5% for $h^{'} = 1$; 0.4% for $h^{'} = 0.5$; 0.3% for $h^{'} = 0.1$. The percentage was calculated considering the medium value for all the viscosities. In BGK SW model, the phase lag grows of about 0.5% for all the depths. It has to be pointed out that these percentages do not change significantly with the change in viscosity value (see figures 4.12 and 4.13 and 4.14).

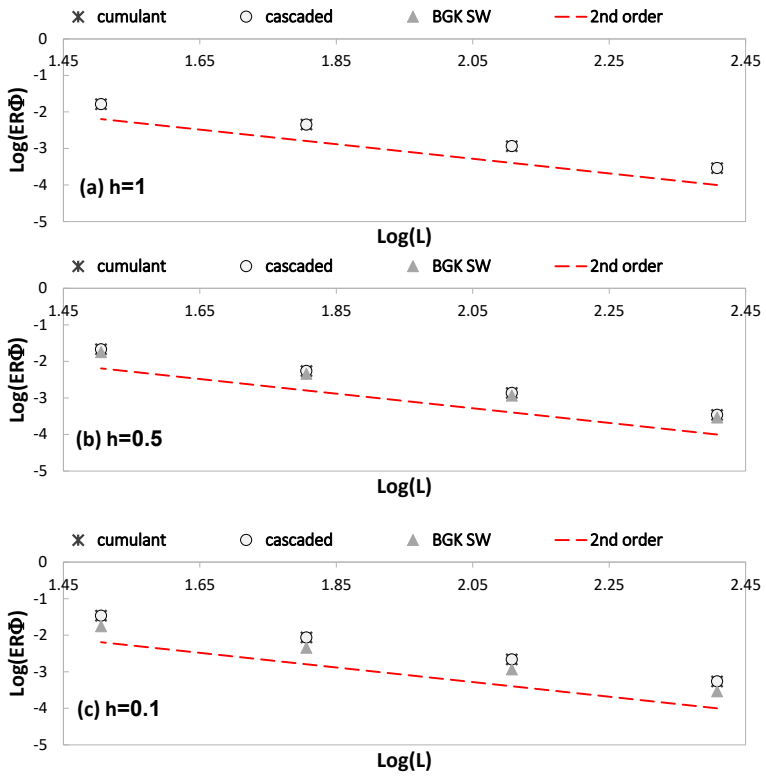

FIGURE 4.12: Fast velocity set - phase lag ER_{Φ}, for the three depths: $h^{'} = 1.0$, $h^{'} = 0.5$, $h^{'} = 0.1$ - $\nu^{'} = 0.01$.

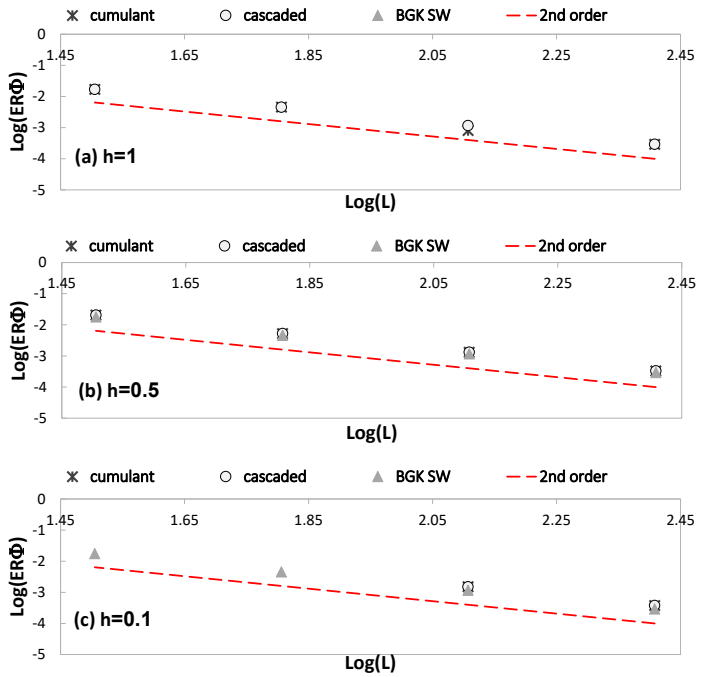

FIGURE 4.13: Fast velocity set - phase lag ER_Φ, for the three depths: $h^{'} = 1.0$, $h^{'} = 0.5$, $h^{'} = 0.1$ - $\nu^{'} = 0.001$.

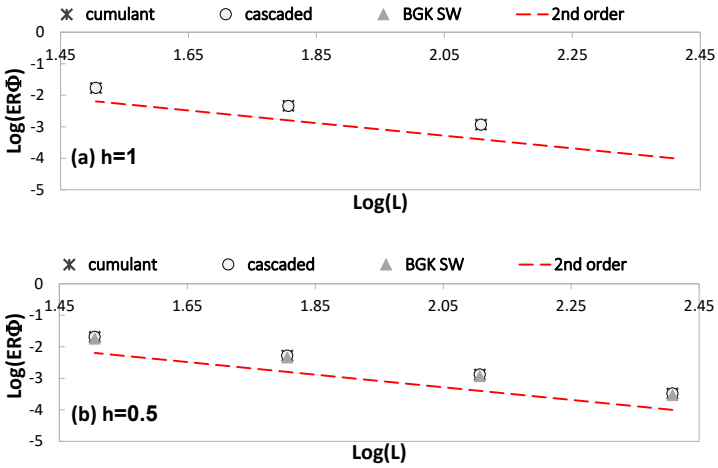

FIGURE 4.14: Fast velocity set - phase lag ER_Φ, for the three depths: $h^{'} = 1.0$, $h^{'} = 0.5$, $h^{'} = 0.1$ - $\nu^{'} = 0.0001$.

4.5.3 Observations about results for high viscosities

First of all, it should be noticed that, in the evaluation of errors for viscosities higher than $\nu^{'} = 0.01$, a shorter time sampling of measurements has to be taken into consideration, as the wave decays with the exponential of the viscosity. In our case, for a viscosity equal to $\nu^{'} = 0.1$, the sampling interval is $K\left(\frac{L}{L_0}\right)^2$ with K =100. In such a case, cumulant and cascaded models continue to display a stable behaviour for the value of viscosity $\nu^{'}$ equal to 0.1 and for $h^{'} \geq 1$ (see the stability range in Figure 4.17). Analyzing simulations results of CumLB and CaLB model for high viscosities, it was noted that the trend illustrated in the previous cases (section 4.5.1 and 4.5.2) was maintained; in fact, an accuracy decrease, both in viscosity and in phase, can be put in evidence adopting viscosity $\nu \geq 0.1$. About BGK SW model, it results stable for $\nu = 0.1$ and h ≥ 1 (stability range in Figure 4.18). Maintaining the trend already observed in previous sections, its behaviour is surely characterized by a slightly higher accuracy than CumLB/CaLB models for the slow velocity set, but it results generally less stable than innovative models for high velocities.

4.5.4 Velocity error in cumulant model

In order to have a further confirmation of the high accuracy of the new models, the velocity error norms (section 4.3) were measured in correspondence of the decay time of the wave t_D, using the diffusive scaling. Figure 4.15, for $h^{'} = 1$ and $\nu^{'} = 0.001$, shows the comparison between the analytical and numerical solution for the cumulant model. The different formulation of the errors, shown in Table 4.1, do not differ significantly. As expected, in CumLB model the value of the errors increase with the decreasing of the viscosity. As shown in the table, the error raises of about 8% if the viscosity becomes tenth times lower. In Figure 4.16, the trend of the value of the L_2 error norm is shown. In logarithmic scale, the slope of the trend is equal to -2.

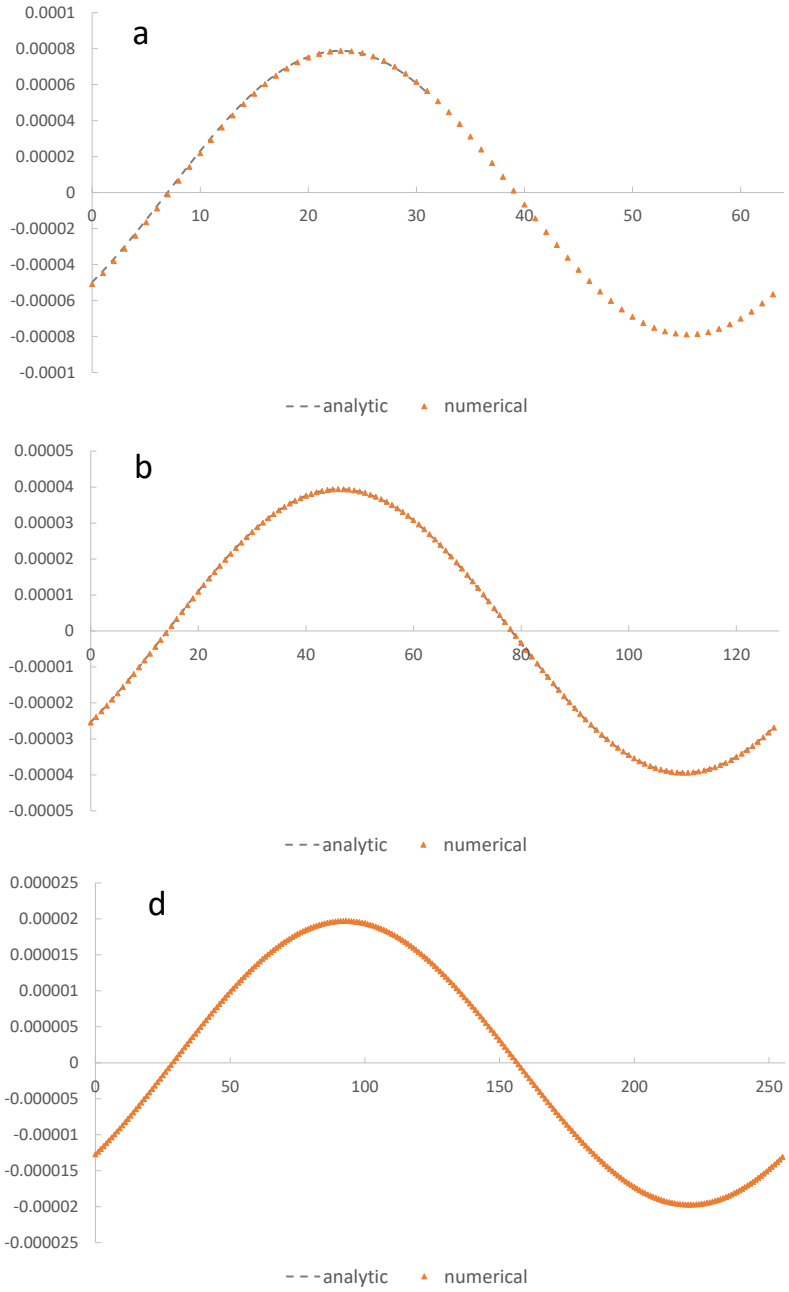

FIGURE 4.15: CumLB - simulated velocity $v^{'}$ of the wave along the y - axis for three values of L; from the top, L = 64, 128, 256 nodes, at the decay time t_D, $h^{'}$ =1, $\nu^{'}$=0.001.

TABLE 4.1: L_∞, L_1, L_2 norms as function of the number of nodes - logarithmic scale.

	$\nu' = 0.01$			$\nu' = 0.001$		
L	**L $_\infty$**	**L1**	**L2**	**L $_\infty$**	**L1**	**L2**
32	0.008520	0.008511	0.008539	0.069956	0.070018	0.069759
64	0.002123	0.002121	0.002125	0.017475	0.017468	0.017489
128	0.000530	0.000530	0.000530	0.004369	0.004368	0.004369
256	0.000132	0.000133	0.000132	0.001091	0.001091	0.001091

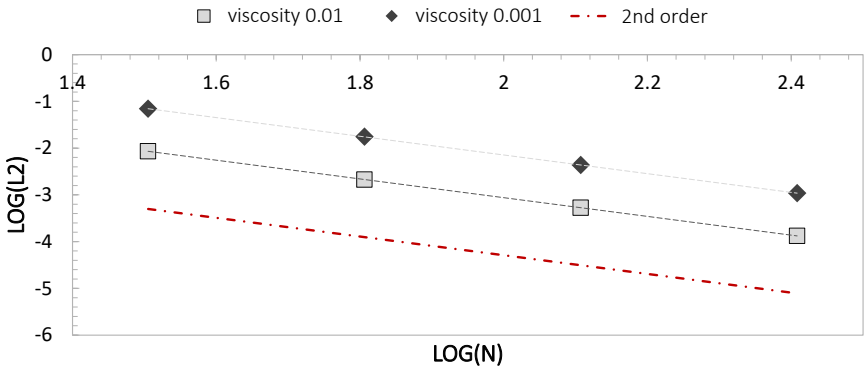

FIGURE 4.16: CumLB model - L_2 norm of the velocity v along the y-axis for the values of L equal to 32, 64, 128, 256 nodes, at the decay time t_D, $h' = 1$, $\nu' = 0.001$ and $\nu' = 0.001$ - logarithmic scale.

4.6 Observations about stability range

In this chapter, different models for the solution of the shallow water lattice Boltzmann equation have been compared, from the point of view of stability and accuracy. In particular, the Taylor Green vortex test in a rectangular domain has been considered significant to evaluate the behaviour of the models from the point of view of isotropy, also along the directions not coincident with the longitudinal and transversal axis of the domain. In Figures 4.17 and 4.18, the stability range of the models is shown. The stability range changes for the different values of depths of the water, h', translational velocity, u_0' and viscosity ν'. It should be noted that, to define the range of stability, an intermediate velocities value (between the fast and slow set) was considered with translational velocity $u_0' = 0.05$ and wave amplitude $U' = 0.00175$. In the graphs, the values of the quantities previously listed are expressed in l.u.

(lattice units); since Δx = 1 m, the value of the depth in l.u. coincides with the physical value. Circles indicate the points where the simulation was performed.

As it is possible to conclude from the previous sections, the CumLB and CaLB models, in their stability range, show, in viscosity and error phase, a second order accuracy, as generally expected in a lattice Boltzmann model (Krüger et al., 2016). Moreover, the stability range of CumLB and CaLB model is similar and is represented with the same graph. But it has been pointed out that cascaded model, for the lowest depths, shows an higher viscosity error (section 4.5.1). The depth $h^{'}$ characterized by the most stable behaviour is 0.5, for which the simulations are stable for all the value of the viscosities taken into consideration. If the value of the depth moves towards lower or higher values, the stability properties change. In particular, for low depths ($h^{'}$ = 0.1), CaLB and CumLB models are stable for the lowest viscosities ($\nu^{'}$ = 0.001 and $\nu^{'}$ = 0.0001) only using low translational velocities. For depths going towards values around 1 m, the models are always stable for the slow set of translational velocities, but for the fast set, we have to arrive to a viscosity value $\nu^{'}$ equal to 0.01 to reach a stable behaviour. Moreover, for depths higher than 1, it can be generally noted a decreasing in accuracy. The BGK SW model is generally characterized by a more limited range of stability, for the different depths. In particular, it exhibits instability for $h^{'}$ equal to 1 and low viscosities ($\nu^{'}$ = 0.01, $\nu^{'}$ = 0.001 and $\nu^{'}$= 0.0001). It starts to become stable only for viscosities $\nu^{'}$ equal or higher than 0.1. In the end, the models based on a variable speed of sound are surely characterized by a wider stability range, also if, as put in evidence in the previous sections, the error is obviously depending on the value of depth more than the BGK model. Moreover, when it is stable, the BGK model shows a slightly lower error in viscosity and in phase than cumulant and cascaded models.

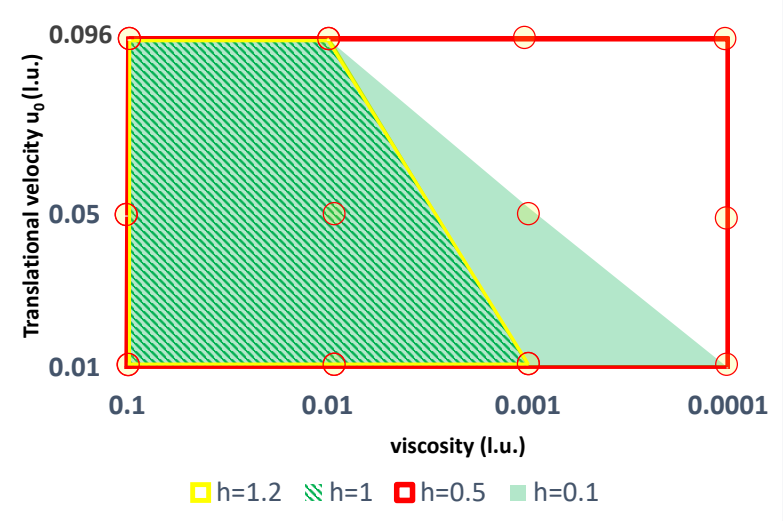

FIGURE 4.17: Stability range of CumLB/CaLB model with the variation of viscosity and translational velocity (l.u.).

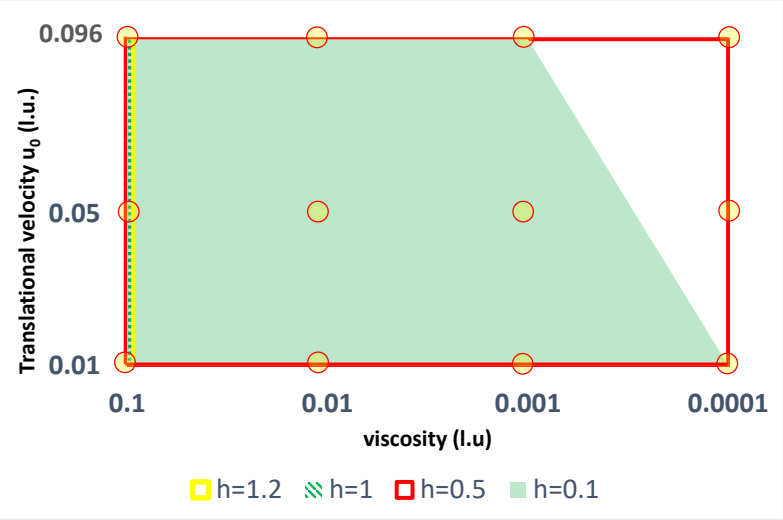

FIGURE 4.18: Stability range of BGK SW model with the variation of viscosity and translational velocity (l.u.).

Chapter 5

Model validation

In the next sections, the cumulant or the cascaded collision operator are used in the numerical model (respectively, CaLB or CumLB). The model is specified at each section.
It has to be pointed out that in all the test cases the quantities (depth, velocity, etc.) are expressed in physical units, except if it is differently specified.

5.1 One-dimensional validation

Hereafter, the standard benchmark of the Stoker dam break and of the flow over a bump in a channel are presented. Both the tests have an analytical solution. The numerical results of the Stoker dam-break are compared with the solution at a certain time (non-stationary solution), while the water surface (WS) and velocities in the bump test are measured once the steady state is reached (stationary solution).

5.1.1 Stoker dam break

The one dimensional (1D) shock tube for a incompressible isothermal fluid is a standard benchmark test for hydrodynamic codes. Analytic solutions of the one dimensional dam break problem can be found in Stoker (Stoker J. J., 1957). A fluid domain of 200 m x 200 m was taken into account. At t=0, the flow region is characterized by two different water levels, h_l= 10 m and h_r= 5 m, with the presence of a step-wise discontinuity located at x = 100 m (Figure 5.1). A transient flow arises, consisting of two waves. The former reflects from the discontinuity to the region with the higher water level. The latter is a shock wave moving in the opposite direction. Assuming a flat bed surface without friction, this phenomenon can be considered as a Riemann

problem. The initial conditions are:

$$\begin{cases} u = 0 & everywhere \\ h_l = 10 & 200 > x \geq 100 \\ h_r = 5 & 100 > x \geq 0 \end{cases}$$

with h_l, h_r, x expressed in m and u in m/s. At the boundaries, it is imposed a no-slip BC. The relaxation rate τ was set equal to 0.7 and different values of the grid space were considered: Δx=2, 1, 0.5, 0.25 and 0.125 m.

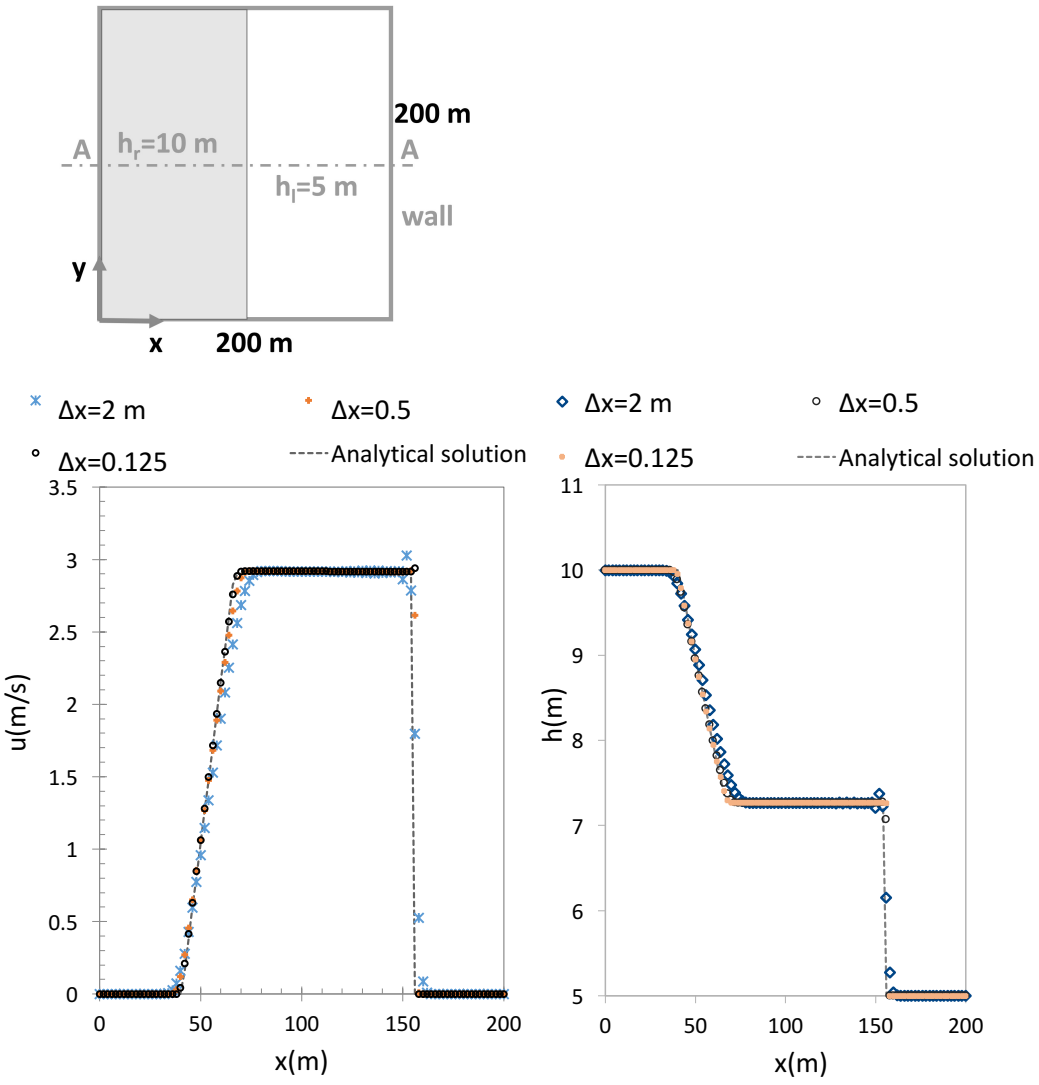

FIGURE 5.1: Dam Break Stoker test case. Top: simulation setup. Bottom: solution comparison at section A - A for different grid spacing - water depth h (m) and velocity u (m/s).

The analytical solution of the problem is reported in (Delestre et al., 2013).

The sensitivity of the numerical solution to the grid size is analyzed by gradually decreasing the Δx, as it is reported before. After 6 s, the values of the water depth and fluid velocity, in correspondence of the vertical section A-A located at the centre of the domain, are shown (Figure 5.1). The analytical solution exhibits four knees. The presence of such marked gradients makes the solution difficult to be estimated. Anyway, the flat zones of both the curves (h and u) are well represented by the CaLB, even for relatively coarse grids. On the contrary, an high resolution is required in order to catch the sharp knees. In fact, for the highest resolutions Δx=0.125 m, the value of the L_2 norm (section 4.3.3) of h and u is, respectively, 0.02 and 0.1.

5.1.2 Flow over a bump

A numerical scheme is considered to be well balanced if it can reproduce an exact solution to a stationary case in an uneven bed (Zhou, 2004). For this reason, the 1D test case of a still flow over a channel is considered.
The setup of the simulation is the same as in (Randall J.LeVeque, 1998). The channel is 1 m long. The BC are periodic at the east and west boundaries; on the south/north boundaries the bounce-back BC are imposed. In the numerical model, Δx=0.01 m, Δt =0.026 s and τ = 0.85 and the bed topography is expressed by the equation:

$$z_b(x) = \begin{cases} 0.25\left(\cos\frac{\pi(x-0.5)}{0.1}+1\right) & |x-0.5| \leq 0.1 \\ 0 & otherwise \end{cases} \tag{5.1}$$

with x, z_b expressed in m. Initially, the water is still ($\mathbf{u}$ = 0) with the water level (WS) equal to 1 m, i.e. WS=$h + z_b = 1$, where h is the water depth. The exact solution for this case is $\mathbf{u}$ = 0 and $h + z_b = 1$. The model used in this test-case is the CumLB.
The formulation of gravity force derives from the equation 2.3 and can be expressed by different discretization schemes. Then, three different schemes can be considered in order to simulate the force due to the gravity: the basic scheme, the central scheme and the second order scheme (Zhou, 2004). In the basic scheme, the force term is evaluated at the lattice point and it can be discretized in the following form:

$$F_i = -gh(i,j)\frac{[z_b(i+e_\alpha\Delta x, j) - z_b(i-e_{\alpha i}\Delta x, j)]}{2\Delta x} \qquad \alpha = 0,...,8 \tag{5.2}$$

where the subscript i indicates the component of the force along the i-direction. Zhou demonstrated that the use of this scheme leads to a LB equation only first order-accurate; on the other hand, the use of a suitable form for the force term can make the lattice Boltzmann equation second order accurate in the recovery of macroscopic continuity and momentum equation. In the second order scheme the force term assumes the averaged value of the two values at the lattice point and its neighbouring lattice point, respectively:

$$F_i = -\frac{1}{2}gh\left(i + e_\alpha \Delta x, j\right)\frac{\left[z_b\left(i + 2e_\alpha \Delta x, j\right) - z_b\left(i, j\right)\right]}{2\Delta x} \qquad \alpha = 0, ..., 8 \quad (5.3)$$

Finally, in the centred scheme, the force term is evaluated at the mid point between the lattice point and its neighbouring lattice point:

$$F_i = -g\frac{\left[\left(h\left(i + e_\alpha \Delta x, j\right) + h\left(i, j\right)\right)\right]}{2} \cdot \frac{\left[z_b\left(i + e_\alpha \Delta x, j\right) - z_b\left(i, j\right)\right]}{\Delta x} \qquad \alpha = 0, ..., 8 \quad (5.4)$$

It has to be pointed out that for constant forces, the three schemes are identical; for a linear force term, the centred and the second-order schemes are equivalent, but they becomes different for a non-linear force (i.e. the gravity force).

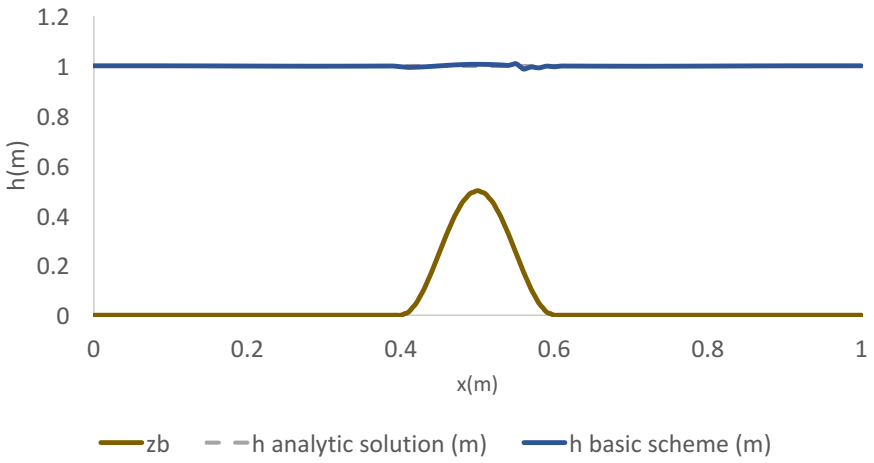

FIGURE 5.2: Basic-scheme: WS after 5000 time steps.

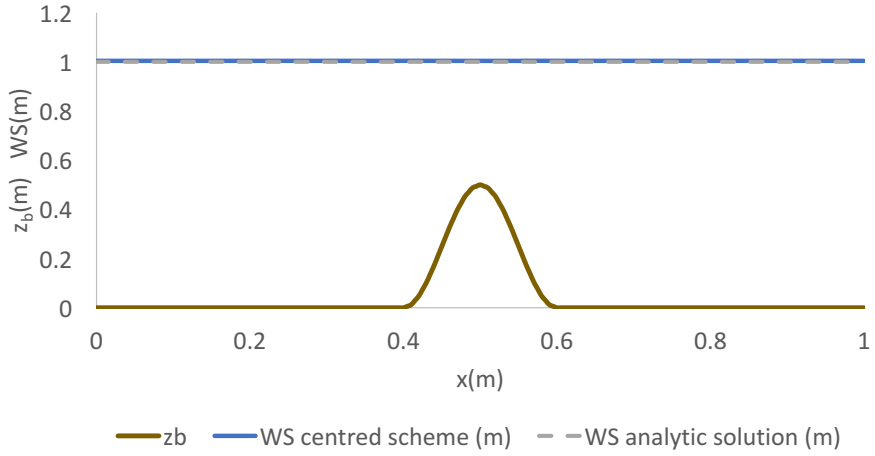

FIGURE 5.3: Centred-scheme: WS after 1000 time steps.

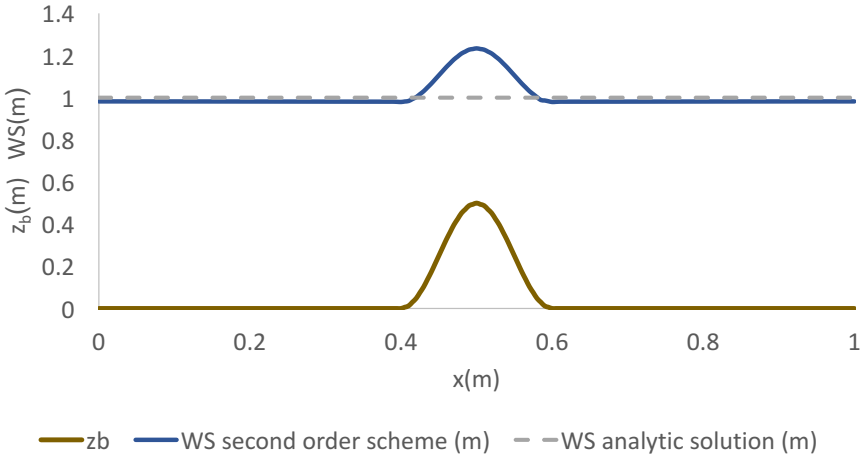

FIGURE 5.4: Second order scheme: WS after 5000 time steps.

The Figure 5.2 shows the WS in CumLB model that uses the basic scheme in order to model the force. The steady state is reached after 5000 time steps. The WS shows an irregular trend over the bump. The simulation becomes unstable after 9000 time steps. In fact, the artificial velocity created along the x-axis leads to the instability of the numerical simulation. In Figure 5.3 it is shown the steady-state solution for the centred scheme of the force, reached after 1000 time steps, is in agreement with the solution. In fact, in this scheme the value of the velocity remains very low ($<= 10^{-3}$) as predicted from the analytical solution. Moreover, the simulation runs until 10000 time steps, remaining always stable. On the contrary (see Figure 5.4) the second order scheme leads to a profile of the water surface not corrected; it produces a solution with a relative error as large as about 20 %. Then, the steady-state

solution takes a time much longer than in the centred scheme ($\cong$ 5000 time steps) to be reached. The artificial velocities result much more higher than in centred scheme ($\cong$ 0.06 m/s). As in (Zhou, 2004), it is found that only the centred scheme can produce accurate results in agreement with the analytical solution.

5.2 Two-dimensional validation

About the two-dimensional (2D) validation, the Pouseuille flow between two plan plates was used to test the Zou-He BC and the external force model. Moreover, the external force model was tested in a domain with a 2D bump; the results refer to a steady solution (stationary case). On the other hand, the asymmetrical dam-break of Fennema-Chaudhry allows to test the model referring to an unsteady solution.

5.2.1 Pouseuille flow

Zou-He BC

In order to test the Zou-He BC based on the non-equilibrium bounce back and introduced in chapter 3, they were used in the standard benchmark of a laminar flow between two parallel flat plates (Pouseuille flow). The channel of the test-case is 8 m long and 0.8 m wide, the discharge at the inlet and the water stage imposed at the outlet are, respectively, $Q = 0.06\ m^3/s$ and $h = 0.05$ m. The viscosity considered is $\nu = 0.05$ expressed in lattice units. At the inlet, the velocity profile entering corresponds to the analytical Pouseuille law and, at the wall, a no-slip boundary condition based on bounce back rule is applied. Under diffusive scaling, the velocity profiles at the section A - A, B - B and C - C (Figure 5.5) are measured and compared with the analytical solution, using different grids ($\Delta x = 0.02$ m, 0.01 m, 0.005 m). The accuracy of the boundary conditions can be evaluated using the relative global error in term of the Euclidean second norm, defined in chapter 4. It represents the difference between the numerical and the analytical value of the velocity (Table 5.1).

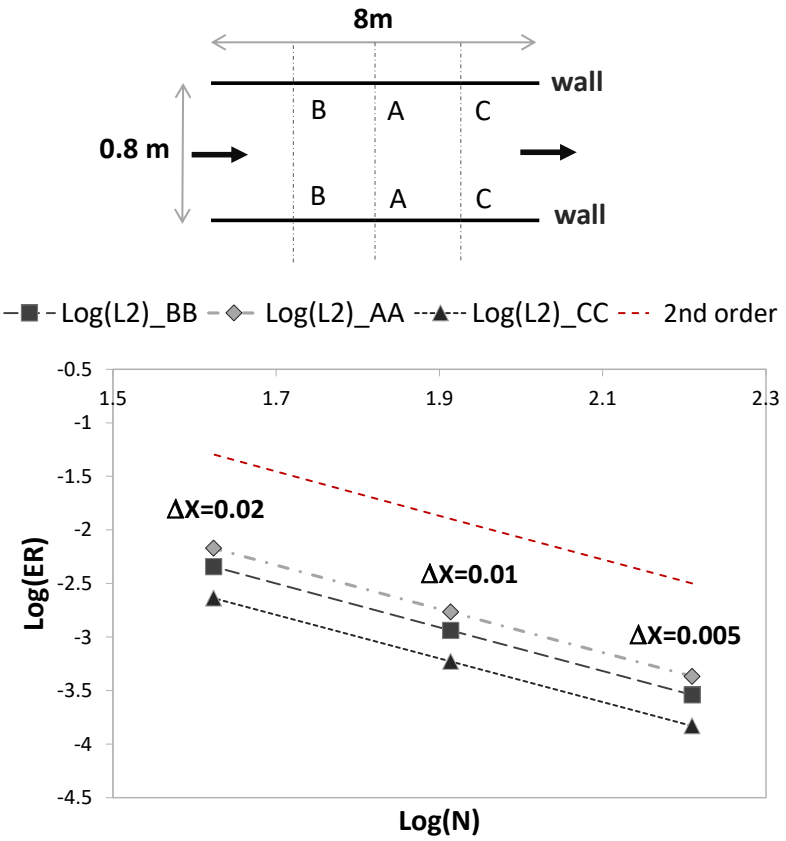

FIGURE 5.5: Left: setup of the simulation. Right: grid convergence analysis for different sections. x-axis: number of nodes of the channel length; y-axis: L_2 norm - logarithmic scale. Δx expressed in meters.

TABLE 5.1: Grid convergence analysis for different channel sections - L_2 norm values.

Δx (m)	$L_2B - B$	$L_2A - A$	$L_2C - C$
0.005	0.000289	0.000429	0.00148
0.01	0.001153	0.001713	0.000593
0.02	0.00453	0.006734	0.002307

The Figures 5.5, 5.6 and Table 5.1 highlight the satisfying accordance between the analytical velocity profile and the simulations, for different resolutions. The second norms, in logarithmic scale and for all the considered sections, have slopes close to -2 (second order accuracy). Moreover, it should be noted that the accuracy of the presented boundary conditions slightly increases from the inlet to the outlet of the channel.

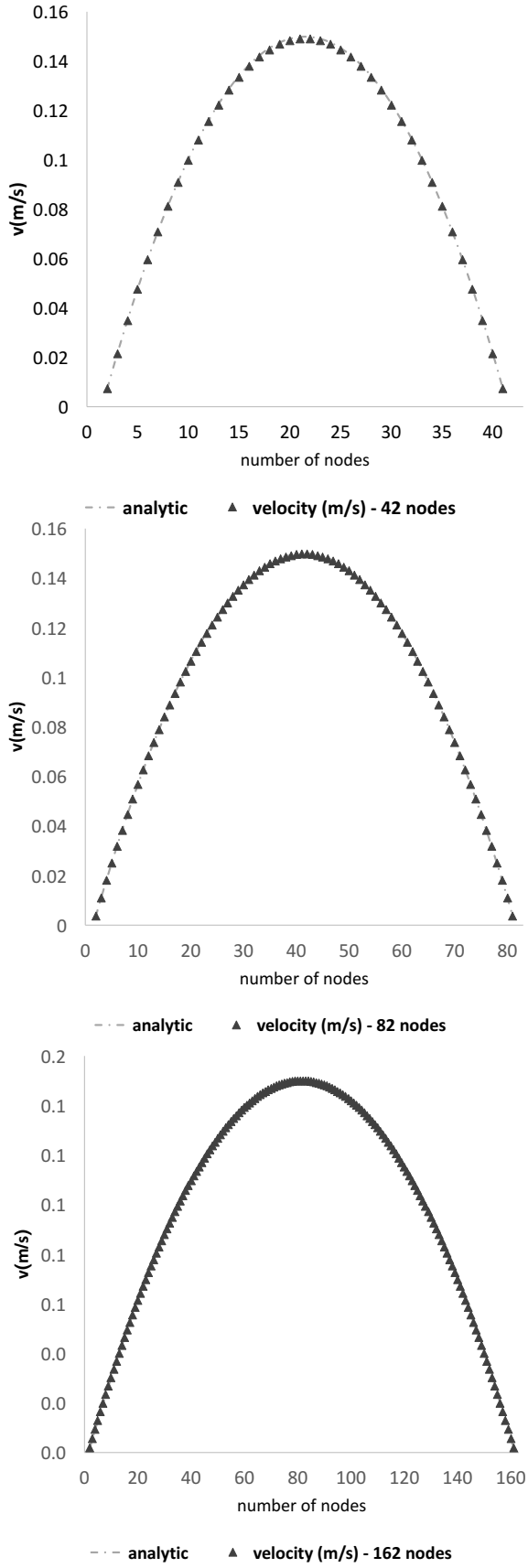

FIGURE 5.6: [Section A-A (Figure 5.5): accordance of the velocity profiles v (m/s) with the analytical solution, for different resolutions (42, 82 and 162 nodes).

Pouseuille flow with external force

Not many analytical solutions for non-linear kinetic equations are known. One of them is the steady plane Poiseuille flow in a channel of $2L$ width and with constant water depth (Liu, 2009). Consequently, the shallow water equations simplify an ordinary differential equation of the flow velocity in the y-direction (v):

$$\nu \frac{\partial^2 u}{\partial y^2} + F_x = 0$$

where F_x is the source term in the x direction. If a no-slip boundary condition is applied at $y = \pm L$ (L is the lateral distance from the middle of the channel width), i.e. $v(y) = 0$ when $y = \pm L$, the analytical solution is a parabola:

$$v\,(y) = \frac{F_x}{2\nu}\left(L^2 - y^2\right) \tag{5.5}$$

The geometry setup is the same for both the test cases (Figure 5.7, Figure 5.8) and the parameters of the simulations are: h = 1 m, Δx=1 m and Δt=1 s.
The results of the first test case are shown in Figure 5.7. It highlights that the profile of the velocities of the numerical model perfectly corresponds to the analytical solution, for different viscosities. The value of the F_x is equal to 0.001 (l.u.); the viscosities taken into consideration were 0.15, 0.117, 0.083, 0.05 (l.u.) respectively correspondent to a τ value equal to 0.95, 0.85, 0.75, 0.65.
The L_2 norm of the velocity value v (refer to chapter 3 for errors calculation) slightly increases with the reduction of the viscosity as it is shown in Table 5.2.

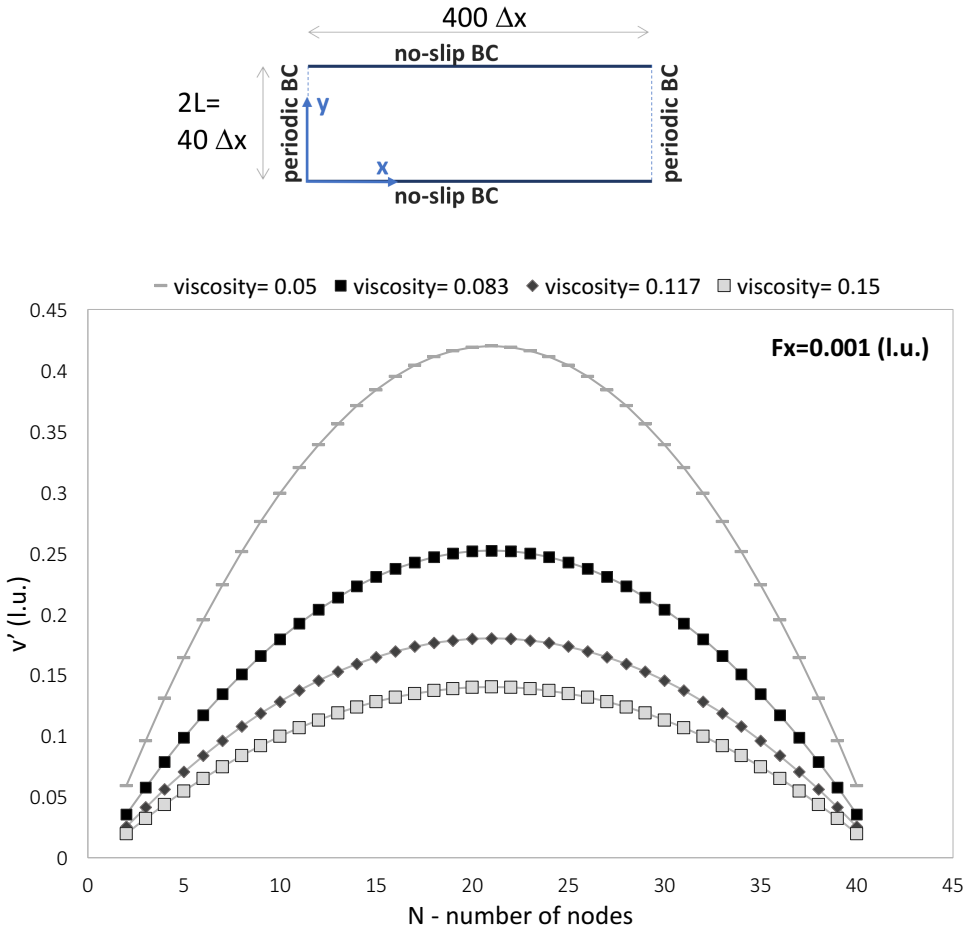

FIGURE 5.7: Top: Setup of the simulation. Bottom: Velocity profiles for different viscosities τ=0.95, 0.85, 0.75, 0.65 in correspondence of the transversal section of the channel. The analytic solution is indicated with a continuous line. Velocity values expressed in l.u.

TABLE 5.2: L_2 norm for different viscosities.

τ	L_2 norm
0.95	0.00017
0.85	0.00020
0.75	0.00029
0.65	0.00052

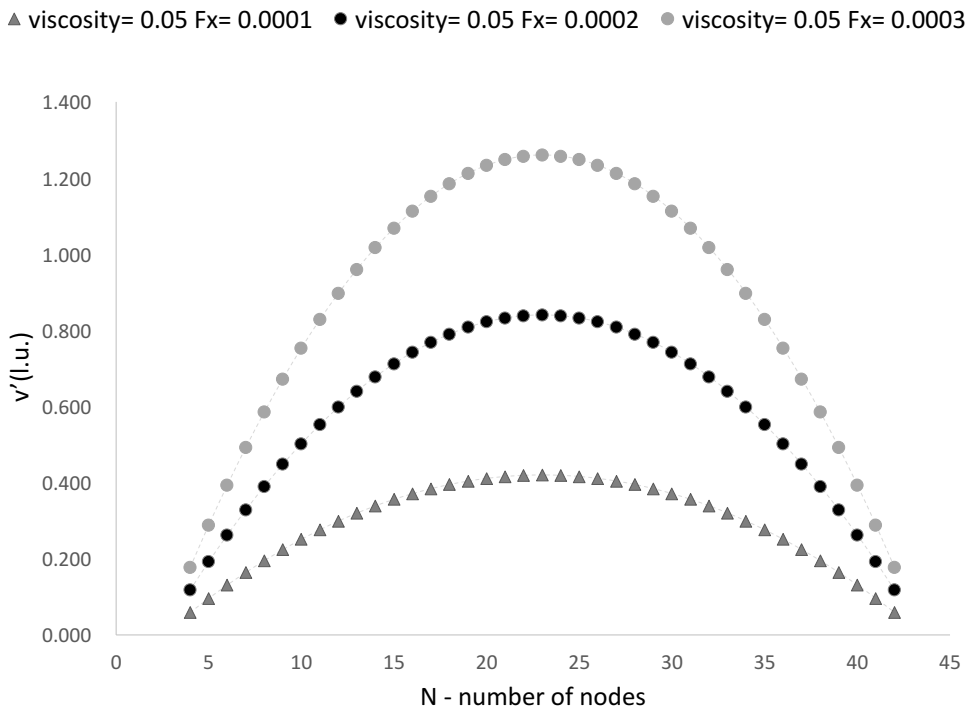

FIGURE 5.8: Velocity profiles for different force values F_x= 0.0001, 0.0002, 0.0003 and ν=0.05 (l.u) in correspondence of the transversal section of the channel. The analytic solution is indicated with a continuous line. Velocity values expressed in l.u.

In Figure 5.8 it can be observed that the profile of the velocities of the numerical model, for increasing values of the force, perfectly corresponds to the analytical solution. As expected, the L_2 norm of the velocity v slightly increases with the increase of the value of the force (Table 5.3):

TABLE 5.3: L_2 norm for different value of the force F_x - Forces expressed in lattice units.

Force F_x	L_2 norm
0.0001	0.00053
0.0002	0.00058
0.0003	0.00070

5.2.2 Flow over a two dimensional bump-stationary case

The simple two-dimensional case of still water over a variable bottom is here investigated. The setup of the simulation is illustrated in (Liu and Zhou, 2014). The domain is a 10 m long and 10 m wide basin. In the basin, the

initial water level is 0.6 m. The equation that describes the bed is:

$$z_b(x) = \begin{cases} 0.5\, e^{-2\left[(x-5)^2+(y-5)^2\right]} & (x-5)^2+(y-5)^2 \leq 4 \\ 0 & otherwise \end{cases}$$

where z_b, x and y are expressed in meters (m). In the numerical model, Δx=0.05 m, Δt = 0.013 s and τ = 0.85. Periodic conditions are applied at the boundaries (fully periodic domain). About the force model, the basic and centred schemes are considered. The steady state is reached after a few time steps ($\cong$ 100 time step), for both schemes. It is observed that, in such test, also the basic scheme is stable and leads to a correct profile of the water surface. However, the spurious velocities assume very high values, not acceptable and not in agreement with the analytical solution that predicts a velocity equal to 0 (Figure 5.9).

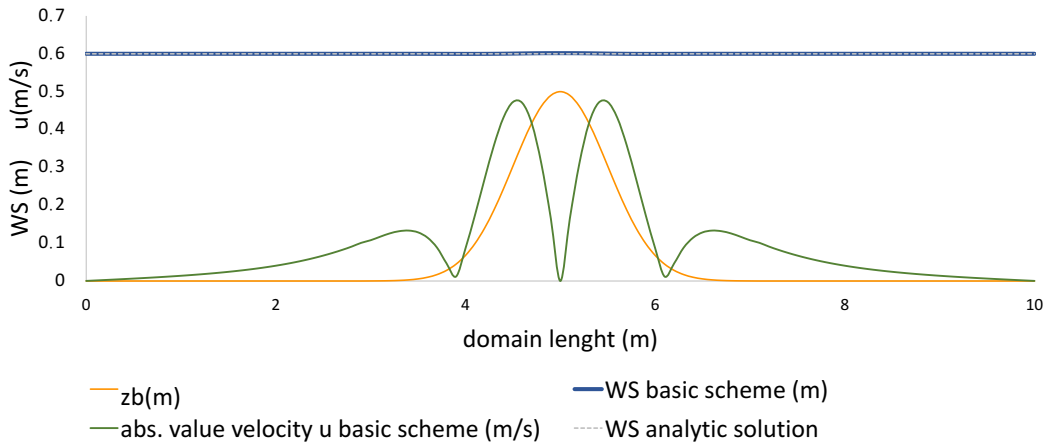

FIGURE 5.9: Basic scheme - z_b bottom level (m) , WS (m), spurious velocities (m/s) and analytic solution.

On the contrary, the centred scheme leads to an acceptable solution, with negligible values of the spurious velocities. In fact, the maximum value is negligible and equal to 0.0022 m/s. Anyway, it has to be pointed out that the incidence of the spurious velocities on the solution of the numerical problem should be evaluated on a case by case basis.

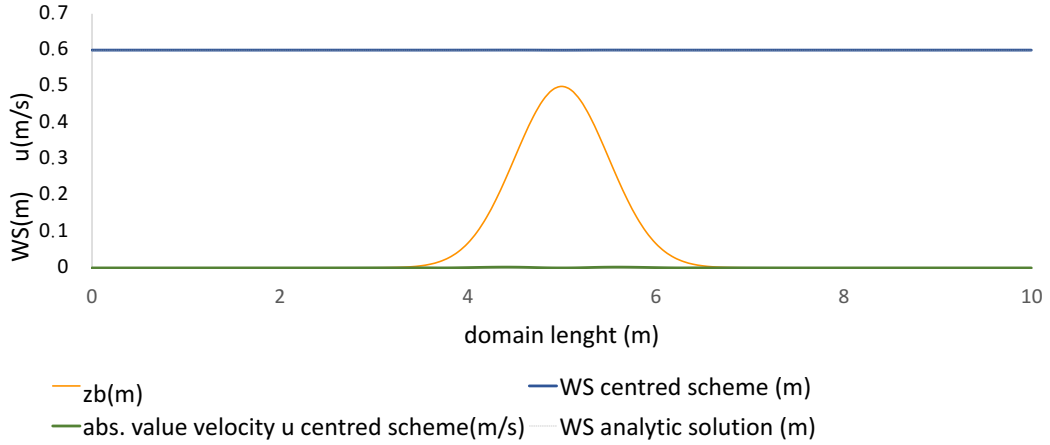

FIGURE 5.10: Centred scheme - z_b bottom level (m) , WS (m), spurious velocities (m/s) and analytic solution.

The errors (L_∞, L_1, L_2 norms) for the basic and central scheme are shown in the following Table 5.4:

TABLE 5.4: WS L_∞, L_1, L_2 norms - correspondence of numerical results with analytical solution.

norm	L $_\infty$	L1	L2
centred scheme	0.00031	0.00035	0.000082
basic scheme	0.00275	0.00246	0.00071

5.2.3 Asymmetrical dam break of Fennema - Chaudhry

The submersion wave due to the partial collapse of a dam in a closed box without friction is here simulated. This test-case has been largely used in literature with the shallow water approach (Fennema and Chaudhry, 1990), (Alcrudo and Garcia-Navarro, 1993). The spatial domain is a 200 m x 200 m flat region, with a dam in the middle (Di Francesco, Biscarini, and Manciola, 2015). In the numerical simulation, Δx=1 m, Δt=0.0082 s and τ=0.7. At the beginning of the simulation the water surface level is set 10 m and 5 m for the upstream and the downstream region, respectively (Figure 5.12, simulation set-up). The asymmetrical dam-break was simulated using the CumLB model. The accordance between the numerical solution and the benchmark test case is satisfying. In fact, the cumulant solution appears more realistic than the one in (Biscarini, Di Francesco, and Manciola, 2010). In particular, the profile in section A-A (Figure 5.15) shows at the wave front a pick higher than the finite volume (FV) solution, more in accordance with the pick height of the benchmark (Figure 5.11, the height of the downstream knee in

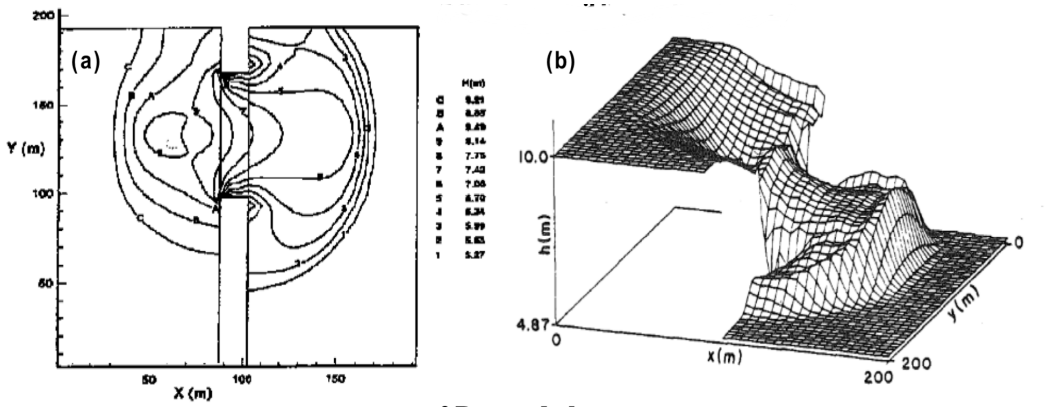

FIGURE 5.11: Asymmetrical dam break - Fennema - Chaudhry, 1990.

Fennema-Chaudhry dam break is 7.75 m). In Figure 5.15 the good agreement between the contours level of Fennema - Chaudhry and of the numerical simulation can be put in evidence. In Figure 5.14 the glyph representation of velocity vector in CumLB model at 7.2 s can be observed. In Figure 5.16 the distribution of the values of the Froude number F_r (see section 2.2) during the simulation of the asymmetrical dam break is shown; it is possible to observe that the simulation remains stable even for F_r higher than one; in particular, the simulation runs correctly until a value of the F_r equal to 2. However, it must be stated that the value of the Froude number higher than one cannot be considered a correct result from the physical point of view. In fact, the D2Q9 model is characterized by a number of speeds too low to allow a correct propagation of the wave of trans-critical and supercritical flows. Referring to (La Rocca et al., 2015), a two-dimensional multi-speed model is presented as a possible solution for the numerical simulation of flows with a Froude number equal or higher than one.

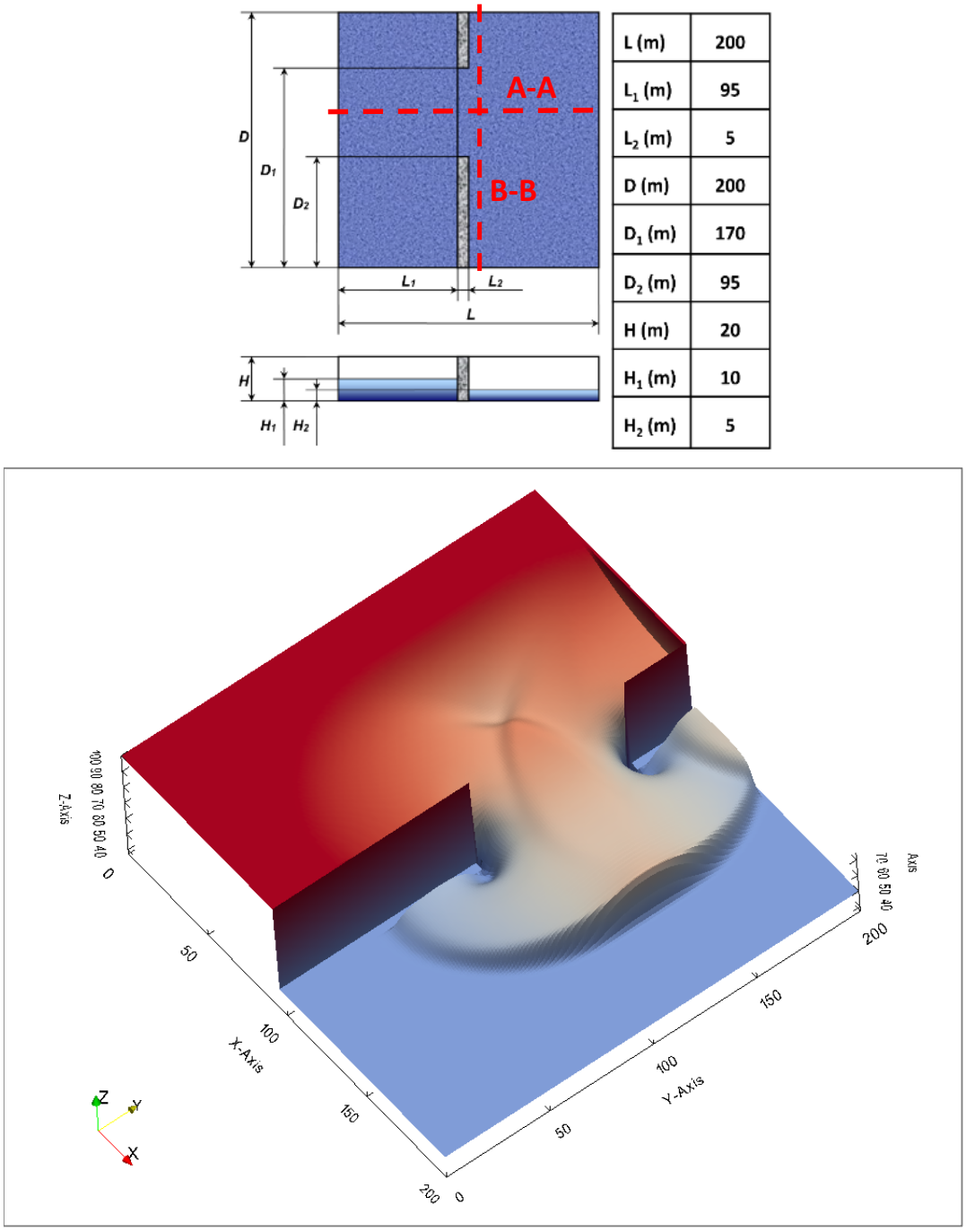

L (m)	200
L_1 (m)	95
L_2 (m)	5
D (m)	200
D_1 (m)	170
D_2 (m)	95
H (m)	20
H_1 (m)	10
H_2 (m)	5

FIGURE 5.12: At the top: Dam-break simulation setup; at the bottom: Three-dimensional view of the dam-break simulation at 7.2 s.

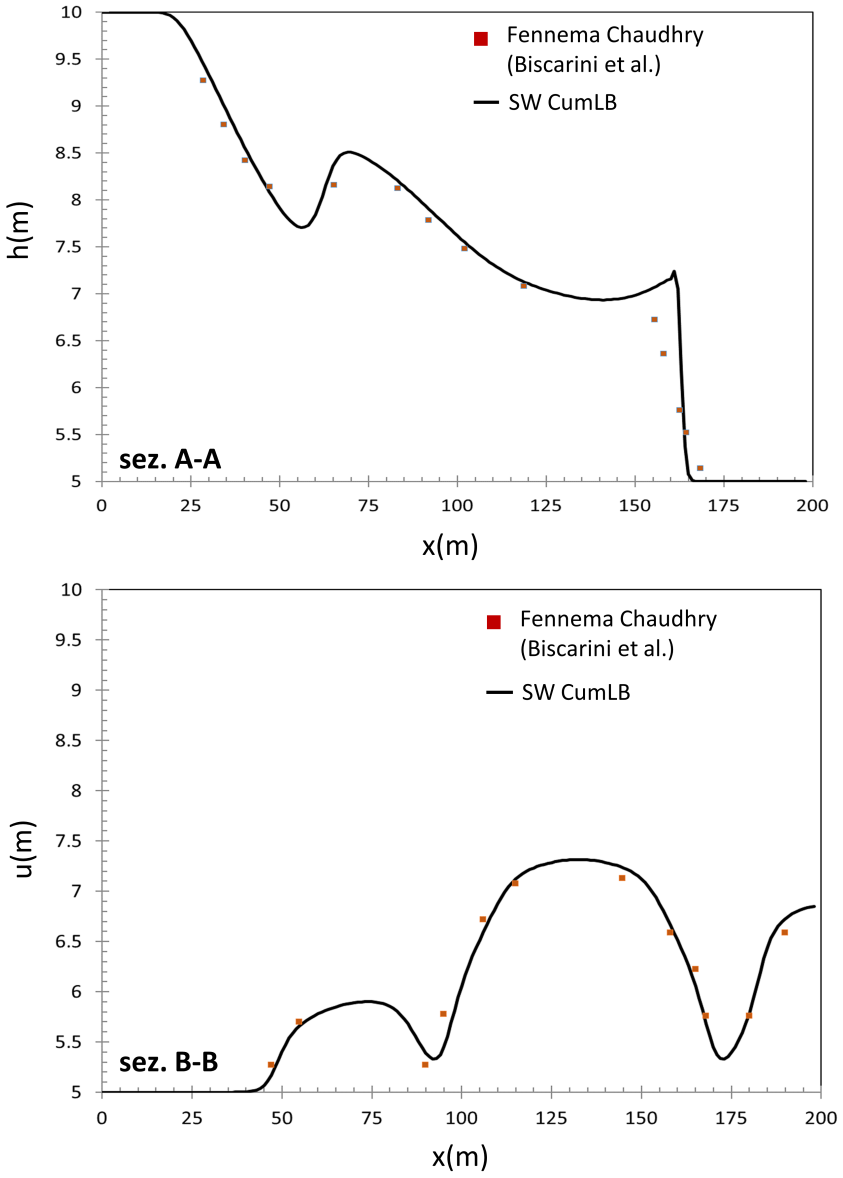

FIGURE 5.13: At the top: section A-A; at the bottom: section B-B, as specified in the simulation setup. Comparison between the numerical solution of cumulant model (continuous line) and a finite volume solution of shallow waters (Biscarini, Di Francesco, and Manciola, 2010) (red dots).

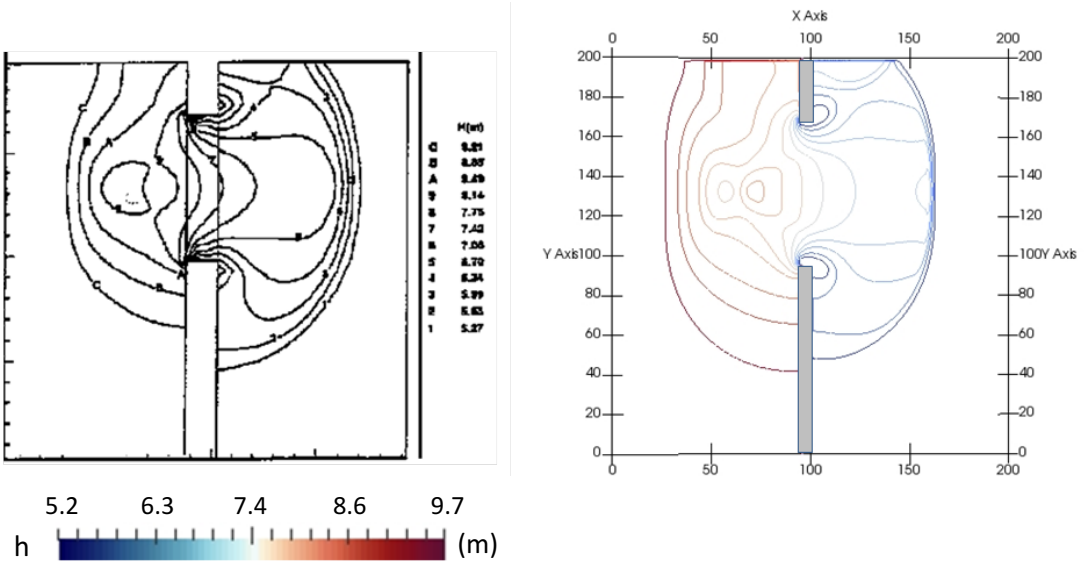

FIGURE 5.14: Comparison between contours level of Fennema-Chaudhry (left) and CumLB (right) at 7.2 s.

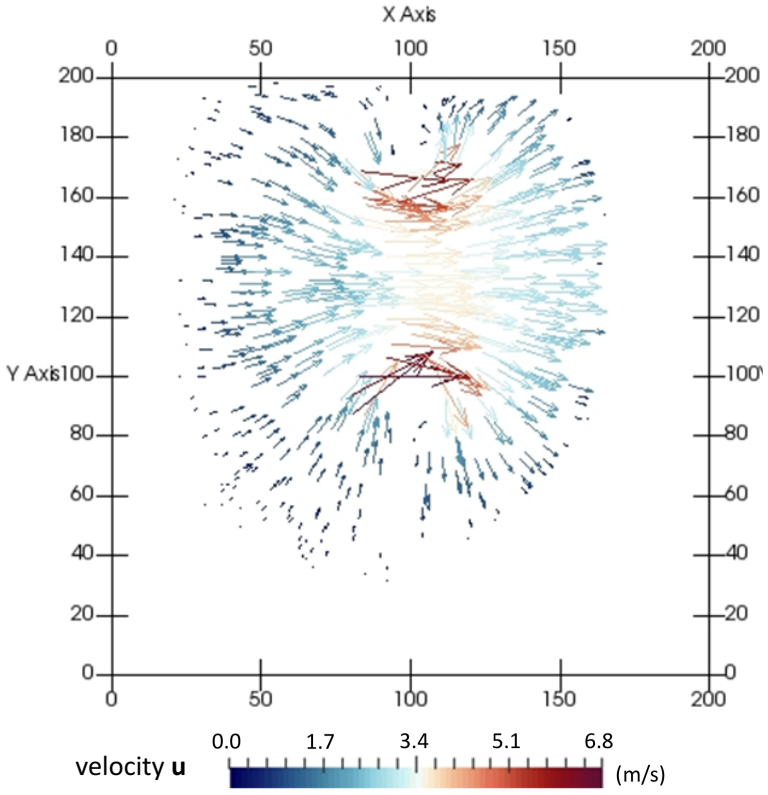

FIGURE 5.15: CumLB: Glyph representation of velocity vector (m/s) at 7.2 s.

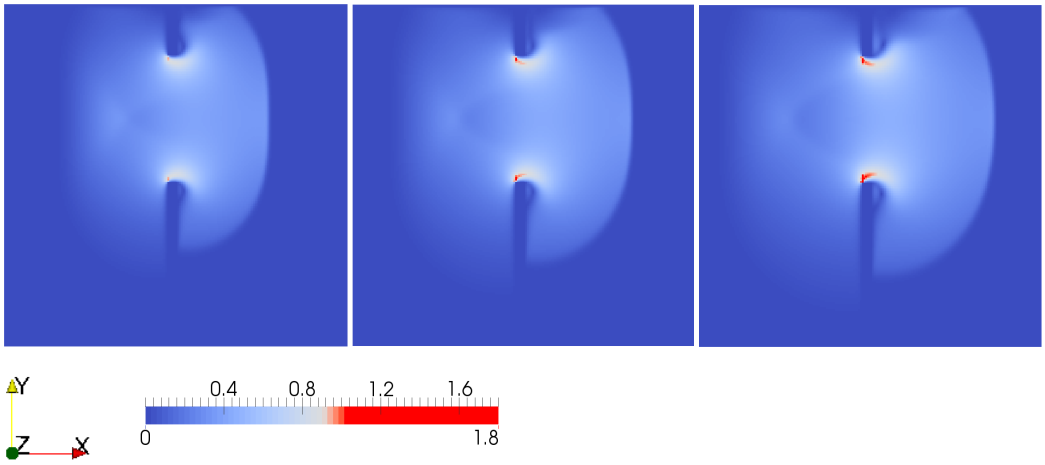

FIGURE 5.16: Distribution values of the F_r at different times. (a) 6.2 s; (b) 7.2 s; (c) 8.2 s.

Chapter 6

Wet-dry approach

6.1 Introduction

An important natural process in shallow-water flows of rivers and coastal regions is the wetting–drying process in water flows such as wave run-up and flooding. In a real situation, the position of the moving wet–dry boundary is decided by a large number of factors (i.e. external forces, dispersion effect due to wave breaking on steep slopes). For example, external forces include gravity, bed friction, wind stress and they greatly influence the position and movement of water fronts. In addition, a long wave could be dispersed through wave breaking, which also leads to the difficulty in water front prediction. Therefore, the movement of wetting–drying fronts (run-up/run-down) is a highly complex phenomenon and a correct simulation of such process plays a crucial role in practical engineering studies.
Several models were developed for wave run-up with conventional numerical methods. Most models need a moving boundary algorithm at the shoreline, as for example discussed by Lynett (Lynett, Wu, and Liu, 2002), who employed a technique based on linear extrapolation. Madsen et al. (Madsen and Sorensen, 1997) used a permeable beach with small porosity, (Que and Xu, 2006) used a thin film in the dry areas of the beach slope. Carrier et al. (Carrier, 2003) proposed a semi-analytic solution technique to evaluate tsunami run-up and down motions on a uniformly sloping beach, based on non linear shallow-water wave theory.

6.2 Lattice Boltzmann approaches of wetting-drying process

Some attempts have been done to solve wet-dry processes with lattice Boltzmann methods. In 2008, Frandsen (Frandsen, 2008) proposed a $D1Q3$ lattice Boltzmann model for wave run-up and simulated a one dimensional tsunami on a plane beach with the standard BGK LBM, without a turbulence model. She incorporated both the linear extrapolation scheme and the thin water film method. Shafiai (Shafiai, 2011) adopted similar schemes and compared the solutions of the different techniques (thin film, interpolation technique). Geveler et al. (Geveler et al., 2011) adopted a mixed method comprehensive of a thin film delimited by a threshold value and a limiter for the velocity. Liu (Liu and Zhou, 2014) presented a new method where the Chapman–Enskog analysis is applied to set up a relation of the particle distribution functions between a dry bed cell and its neighbouring wet cells in a manner consistent with the LBM. External forces such as bed friction can be included straightforwardly in this method.
The approach described in the next sections to model wet-dry boundaries is based on a threshold value of the water depth and on the limitation of the Froude number. The method is validated in stationary and non stationary flow through the test-case of the 2D flow over a bump (section 6.5.1) and of the dam-break over a triangular obstacle (section 6.5.2).
About the system of units, the examples and the test cases introduced for the validation of the model are always presented in physical units. For sake of simplicity, the formulas are expressed in lattice units but the superscript $'$ is omitted.

6.3 Depth-velocity limiter strategy

At wet-dry boundaries, the value of the water depth is limited by a threshold value h_{lim} that allows the code to avoid the error due to the division by zero. Then, if the value of the depth is below the threshold value h_{lim}, the value of the probability distribution functions are updated, in the equilibrium, as follows:

$$f_\alpha^{eq}\left(h = h_{lim}, \quad u = 0, \quad v = 0\right) \tag{6.1}$$

The nodes below the threshold in depth are treated as dry nodes (dry nodes as slightly wet nodes) in order to keep the flow from creeping up slopes.

The effect of the limit on the depth can be observed in the simulation of the flow over a triangular obstacle (Figure 6.1), the test case treated in deep in the next section 6.5.2. The difference between the cumulant model with the limiter and the one without is evident. In fact, the model without the limiter is characterized by the presence of spurious velocities where the depth is equal to zero. In addition, the water surface moves slower if compared with the simulation in section 6.5.2.
Then, in order to avoid inadmissible velocity values due to very low values of the water depth, the approach chosen in this work makes use of a velocity-limiter based on the value of the Froude number (section 2.2). A value of the Froude number is chosen as limiter (i.e. Fr_{lim}); it represents a threshold that cannot be overcome. If the values of the velocity $\mathbf{u}$ leads to a Froude number higher than the limiter, the velocity is newly computed by the Fr_{lim} imposed (Figure 6.2). The value of the updated velocity $\mathbf{u}^*$ is expressed as a percentage $1-\delta$ of the actual velocity by means of the ratio $\frac{Fr_{lim}}{Fr}$:

$$\|\mathbf{u}^*\| = \|\mathbf{u}\| \cdot (1-\delta)$$

the Froude number limiter can be written as:

$$Fr_{lim} = \sqrt{\frac{\|\mathbf{u}\| \cdot (1-\delta)\,\|\mathbf{u}\| \cdot (1-\delta)}{gh}} = (1-\delta) \cdot \sqrt{\frac{\|\mathbf{u}\| \cdot \|\mathbf{u}\|}{gh}}$$

and the value of δ is:

$$\delta = 1 - Fr_{lim}\sqrt{\frac{gh}{\|\mathbf{u}\| \cdot \|\mathbf{u}\|}}$$

$$\|\mathbf{u}^*\| = \|\mathbf{u}\| \cdot \left(1 - 1 + Fr_{lim}\sqrt{\frac{gh}{\|\mathbf{u}\| \cdot \|\mathbf{u}\|}}\right) = \|\mathbf{u}\| \cdot \frac{Fr_{lim}}{Fr} \tag{6.2}$$

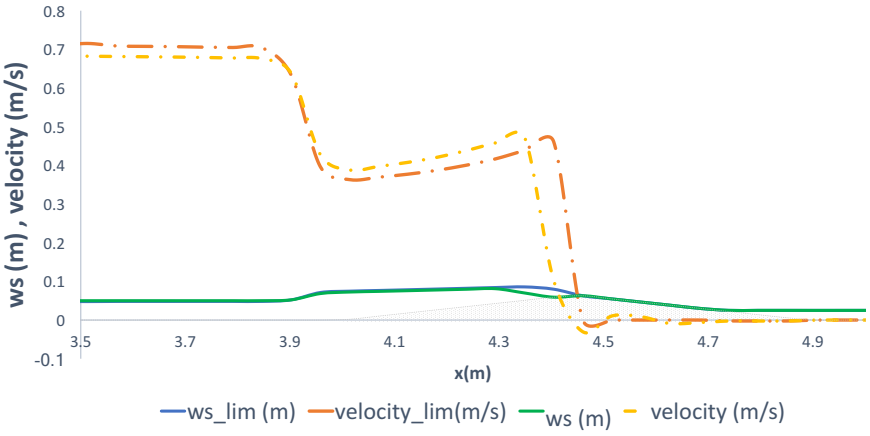

FIGURE 6.1: Comparison of the behaviour of the models with and without the limiter on the height.

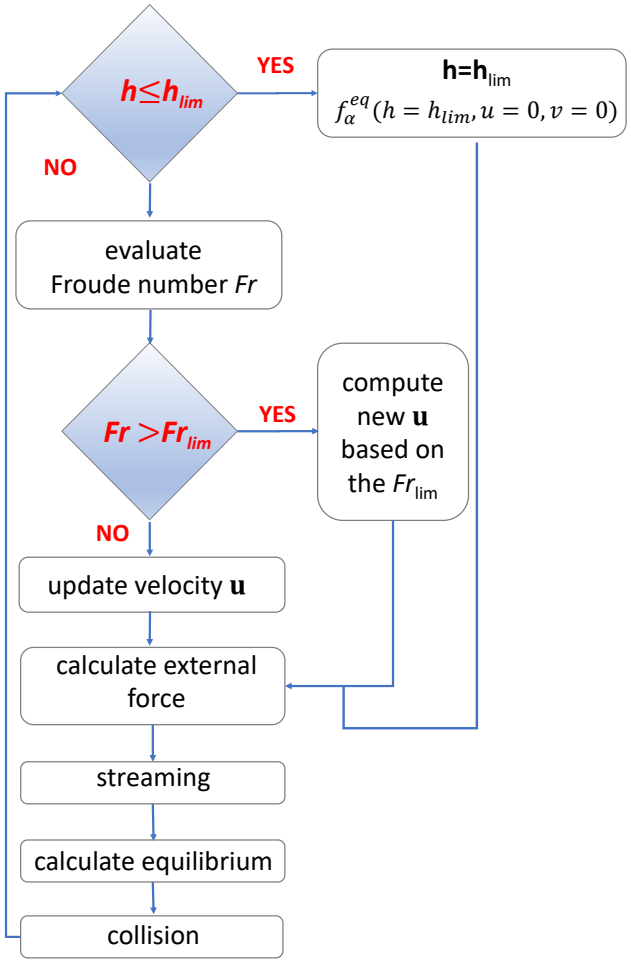

FIGURE 6.2: Solution procedure of cumulant LB model incorporating the wet-dry boundary model.

6.4 Isotropy improvement of the collision in CumLB model

As it is explained in section 3.1.9, it could be possible to consider both De Rosis model (section 2.1.2) and cumulant model in the collision step, in order to investigate the different behaviours and take advantage of the positive features of each model.
In Figure 6.3 the evolution in time of the asymmetrical dam-break of Fennema-Chaudhry is shown. The geometry setup is the same as in section 5.2.3; the water height upstream of the breach is h_u = 10 m, downstream it is approximately equal to zero (h_d=0.0001 m). The parameters of the model are: Δx=1 m; Δt=0.00824 s and τ=0.75. In correspondence of the wet-dry boundary, the model with the cumulant CO is characterized by a lightly stronger anisotropy; on the other hand, the MRT model based on De Rosis work (De Rosis, 2017) shows a behaviour more isotropic, but it results less stable than the model based on cumulants. The geometric scheme setup and viscosity parameter are equal for both the models.

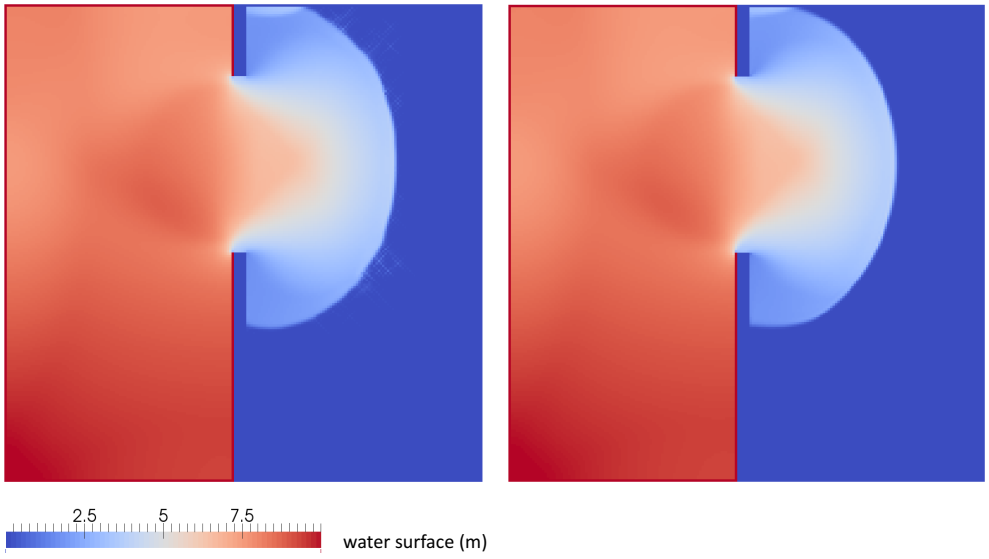

FIGURE 6.3: Evolution of the wave due to the dam-break at t=1.23 s. On the left, cumulant model; on the right, De Rosis model.

6.5 Validation of the wet-dry approach

6.5.1 Flow over a bump in a lake at rest-stationary case

The setup of the simulation is the same as in section 5.2.2 but the initial water height is 0.3 m, in order to leave the bump partially emerged. Periodic conditions are applied at the boundaries, to have a fully periodic domain. In the numerical model, Δx=0.05 m, Δt = 0.013 s and τ = 0.85.
The steady state is reached after a few time steps ($\cong$ 100 time step), as for the submerged bump. Likewise, the maximum value of the spurious velocities is comparable with the one shown in section 5.2.2 and is equal to 0.0026 m/s. In Figure 6.4 the water surface is shown, once the stationary condition has been reached. The water surface is horizontal (as expected) and the spurious velocities assume values acceptably low.

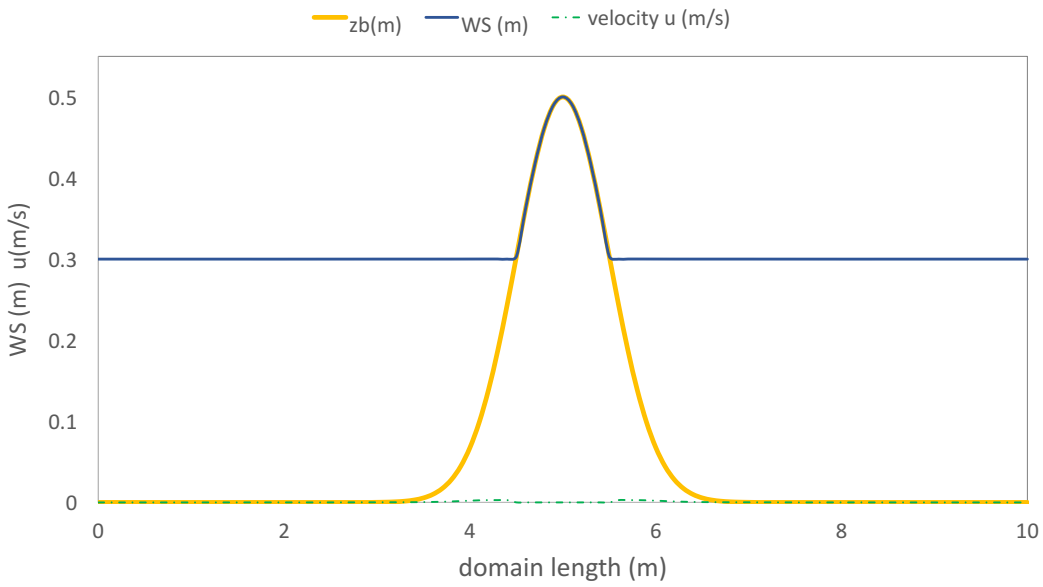

FIGURE 6.4: Water surface WS (m) and velocity u (m/s) in stationary condition.

The force modelling is the centred scheme, already analyzed in section 5.1.2. The adopted scheme leads, as expected, to a correct level of the water surface in correspondence of the two-dimensional bump.

6.5.2 Dam break over a triangular bottom sill

The test case described in the present section is an experimental dam break over a triangular obstacle performed at the Université Catholique de Louvain, in the laboratory of the Civil Engineering Department (Soares Frazao,

2000). The experimental setup consists in a closed rectangular channel 5.6 m long and 0.5 m wide, with glass walls. The upstream reservoir extends over 2.39 m and is initially filled with 0.111 m of water at rest. Downstream from the gate, there is a symmetrical bump 0.065 m high with a bed slope of 0.014. The obstacle and the end walls define a second pool which contains 0.025 m of water. The gate separating the reservoir from the channel is pulled up rapidly, causing the water block to disintegrate and a fast running wave to be generated. Therefore, it is a closed system where the water flows between the two tanks is reflected against the obstacle and the walls of the channel. The setup of the simulation is illustrated in Figure 6.5. Hereafter, a comparison between the two dimensional model CCHE2D (Yafei Jia, 1999) and the cumulant model is performed. The CCHE2D and the experiment test refer to (Biscarini, Di Francesco, and Manciola, 2010), where the accuracy of a 3D BGK lattice Boltzmann is evaluated in comparison with a 2D model.
In our test case, the model considered is the CumLB.

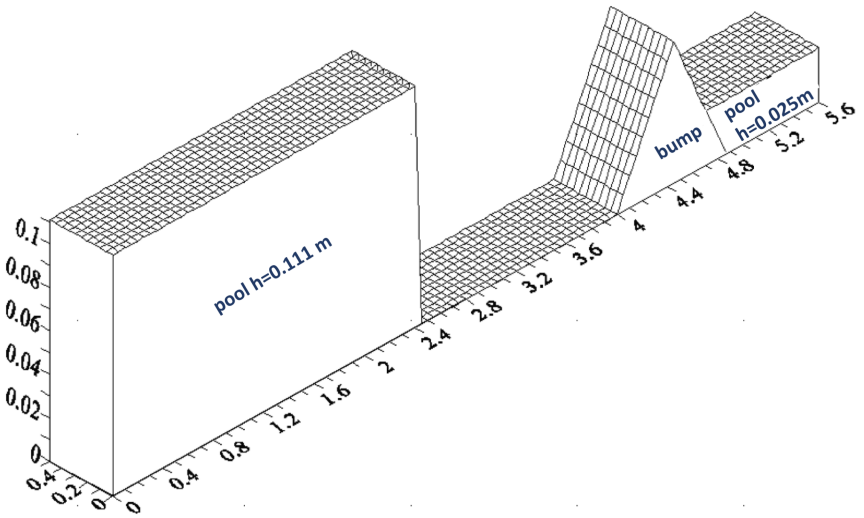

FIGURE 6.5: Experimental set-up and initial conditions for the dam break over a triangular obstacle test case.

The simulation has been performed on a 447 x 120 lattice node domain, corresponding to lattice spacing of 0.0125 m. The water surface level shows a good correspondence with the CCHE2D model, in particular in the first times: t = 1.8 s, 3 s, 3.5 s (Figures 6.6, 6.7, 6.8). In Figure 6.6 the excellent correspondence between the CCHE2D model and lattice Boltzmann model at t=1.8 s is shown. However, the wave approaching the triangular bump appears to travel more slightly in the two dimensional models than in the real one, as it has already been shown in (Biscarini, Di Francesco, and Manciola,

2010).

At t=3.0 s, the correspondence between the two shallow water models is maintained and the 2D model results are more in agreement with the experimental ones. Moreover, the 2D wave moves synchronized with the real wave. However, the experiment shows an higher crest at the obstacle and, respectively, a level lower upstream and higher downstream (Figure 6.7).

At t=3.5 s, the 2D shallow water wave continues to move together with the experiment. The CCHE2D model water surface is in acceptable accordance with the LB model, but the first shows a crest downstream the obstacle. The crest does not appear in the experimental model; in such sense, the LB model fits better the real model (Figure 6.8).

At t=8.4 s (Figure 6.9), the CumLB model is synchronized with CCHE2D model, but, upstream of the obstacle, the level of the water surface is different in the two model. The level of the water surface of the CumLB model seems more in accordance with the experimental one. Downstream, the 2D models shows an acceptable agreement. At t=15.5 s, the 2D models seem synchronized again but they are completely different.

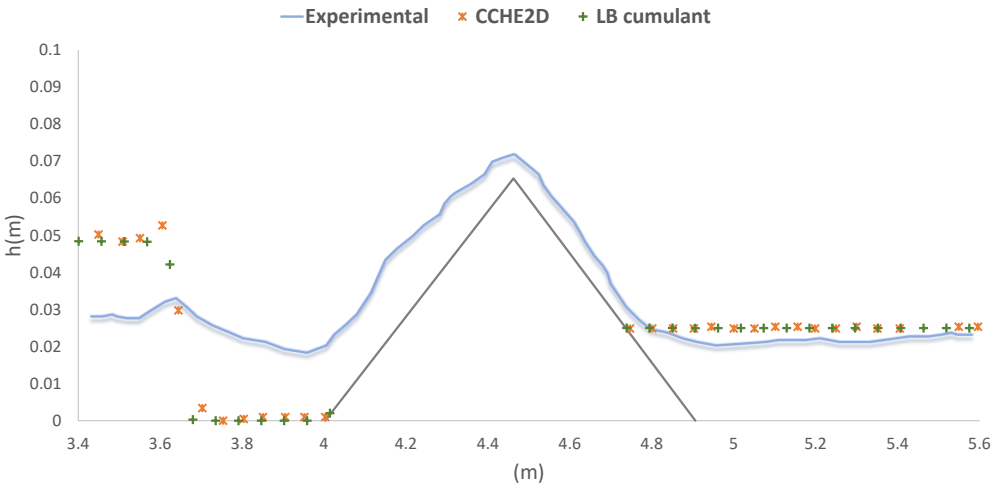

FIGURE 6.6: t=1.8 s - excellent corrispondence between CCHE2D and CumLB results.

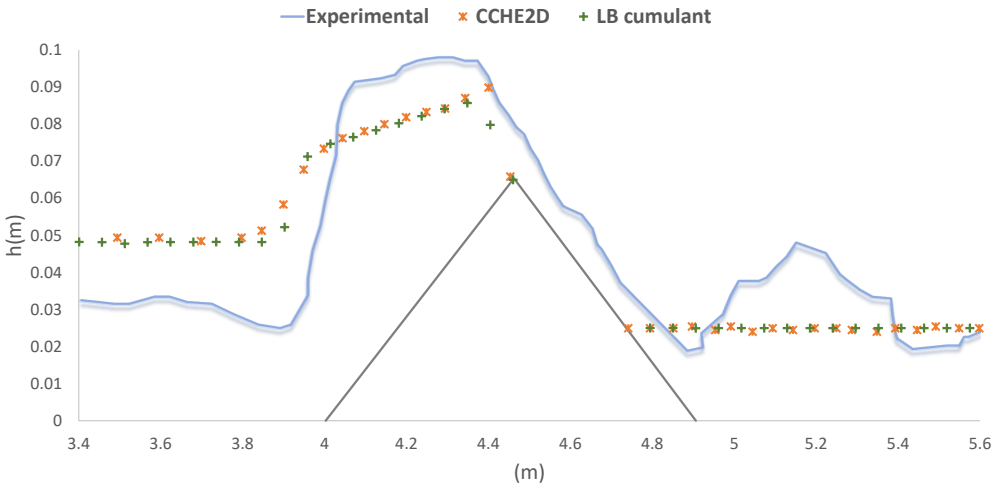

FIGURE 6.7: t=3.0 s - satisfying agreement of experimental results, CCHE2D and CumLB model.

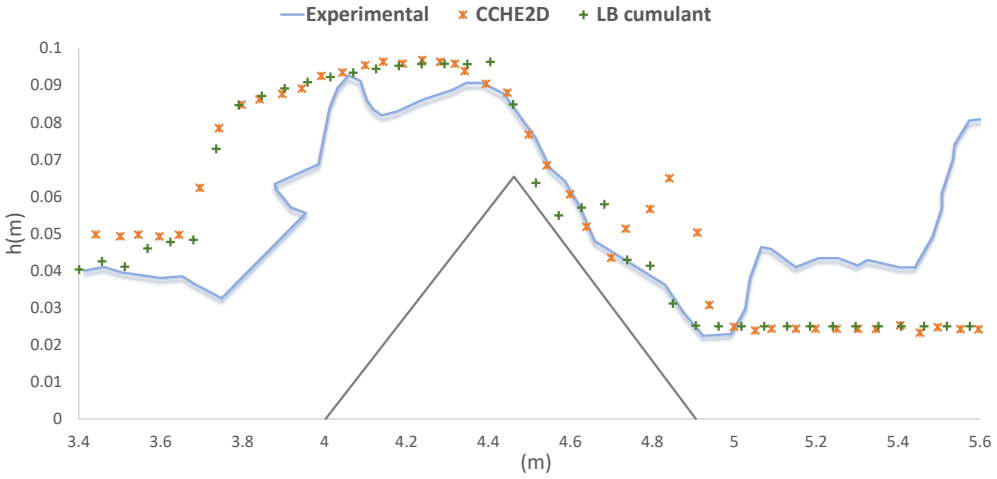

FIGURE 6.8: t=3.5 s - 2D models appear slower than experimental one.

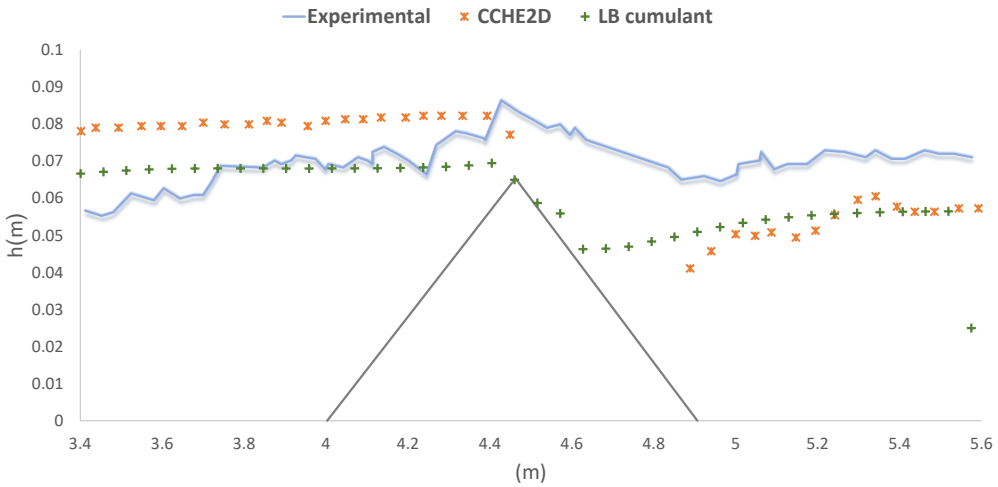

FIGURE 6.9: t=8.4 s - acceptable agreement between 2D models downstream the obstacle.

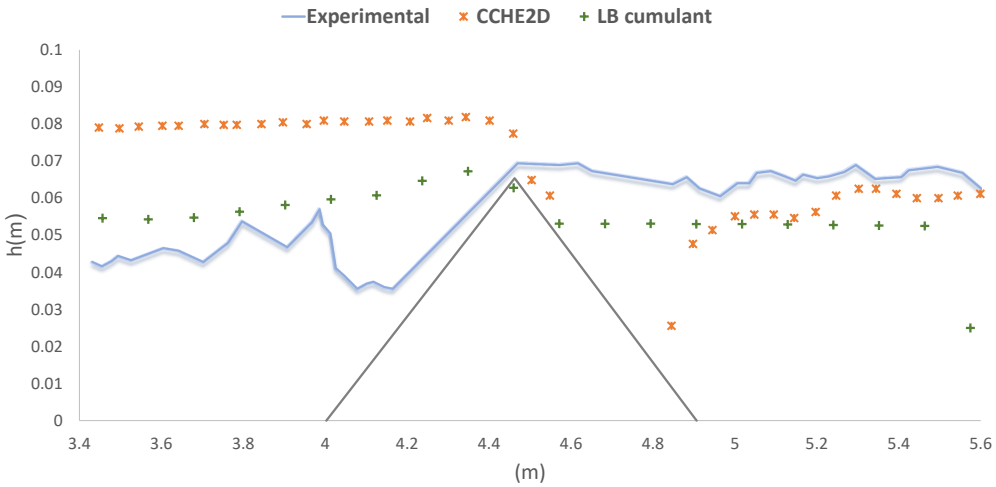

FIGURE 6.10: t=15.5 s - 2D models seem synchronized but they are completely different.

6.6 Discussion

The proposed modelling of wetting-drying boundary gives satisfying results in the stationary case, in particular in determining the level of the water depth h. The spurious velocities are characterized by low values, even if their effect should be assessed in different benchmarks. In the unsteady case, the LB model leads to results comparable with shallow water solvers, at least in the first time-steps of the simulation. However, in the analyzed test-case,

the difference between the experimental and simulation results is slightly important. Further analyses should be performed in order to test the effective capability of the model to simulate dam- break or dam-breach problems.

Chapter 7

Parallel code computation

7.1 Lattice Boltzmann method parallelization

Generally, for practical use of Lattice Boltzmann methods in large scale hydraulic analyses, a huge number of lattices are required and it needs a remarkable computational power. In such cases, the parallelization of the code is useful, for all types of numerical methods. One of the most appealing features of the LBM is that it is easy to implement the parallel computation. In fact, in LB methods, the current value of the distribution function varies only with the previous conditions and the collision step is completely local. In these methods, the parallel calculation can further be improved by using the CPU-based processing structures, which has attracted the interest of many researchers (Succi, 2001), (Wellein et al., 2006). The parallel calculation on CPU architectures could be realized on both distributed and shared memory systems. Moreover, the lattice Boltzmann algorithm is particularly suitable for implementation on GPGPUs (Banari et al., 2014), (Tölke and Krafczyk, 2008), (Schönherr et al., 2011), thanks to its utilization of Cartesian lattices and its typical interaction between nodes based on the restriction of the movement of the particles only towards the next neighbour directions. In (Banari et al., 2014), the computational efficiency of a GPU and a multi-core implementation of the LBM for non-uniform grids is highlighted. The computational performance, frequently considered as a measure of the efficiency of an LBM code, results unaffected by refinement procedure of the grid. The parallel computation of LBM for shallow water based on CPU and GPU was used by Tubbs (Tubbs, 2010). More recently, in (Janssen, Grilli, and Krafczyk, 2012) an efficient GPGPU implementation (NVIDIA CUDA framework) of a Lattice Boltzmann model for the solution of the non-linear shallow water (NSW) equations is presented, including a simple model for the treatment of wet-dry interface.

7.2 CPU parallel computing

In this thesis, a LBM SW code using C-Language was written, following the theoretical framework described in chapter 2.
Just to simplify the explanation, we can consider the information at each node of the grid contained in a cell of a matrix, representing the whole grid. In an LB code, the calculation of the value of the cell of the matrix does not depend on the value of the other cells of the same matrix at the same time, but it only depend on values at the cell calculated at the previous time; in other words, every cell of the matrix does not depend from other cells of the same matrix. Then, in theory it would be possible to calculate all the cells of the matrix at the same time.
The SW LB code used in this work is based on the calculation in parallel of a number of cells equal to the number of processors. In order to achieve the parallelization target, every matrix was divided in a number of sections equal to the CPU threads available. Every section consists of a subset of columns and rows. For each section, a thread is instantiated in order to compute the actual cells value. In this way, the whole matrix is computed in parallel by the code algorithm.
In Figure 7.1, the flow chart of the LBM code is shown. The red blocks indicate the segments of the algorithm that can be parallelized using the previous procedure; the green blocks indicate the segments that cannot be treated in this straightforward way. The segments in which the code has been divided are:

1. parallel preparation: execution of the variables update and calculation of the force;

2. preparation: execution of the streaming step;

3. parallel iteration: update equilibrium and execution of the collision step;

4. finalization: generation of the reports (*.vtk file) for the visualization in the Toolkit Paraview.

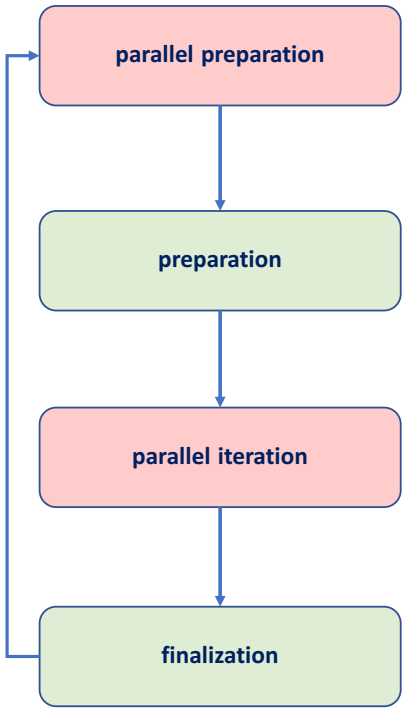

FIGURE 7.1: Flow chart of the implemented SW LBM code.

7.3 Amdahl's law

If f is the fraction of code that can be performed in parallel, the time spent using P processors is:

$$T(P) = T(1)\left(\frac{f}{P} + (1-f)\right) \tag{7.1}$$

As consequence, the "parallel speed up" is given by:

$$S(P) = \frac{T(1)}{T(P)} = \frac{1}{f/P + (1-f)} \tag{7.2}$$

The equation show that, even in the limit of an infinite number of processors ($P \to \infty$), the asymptotic speed-up flattens at the upper limit of $1/1-f$.

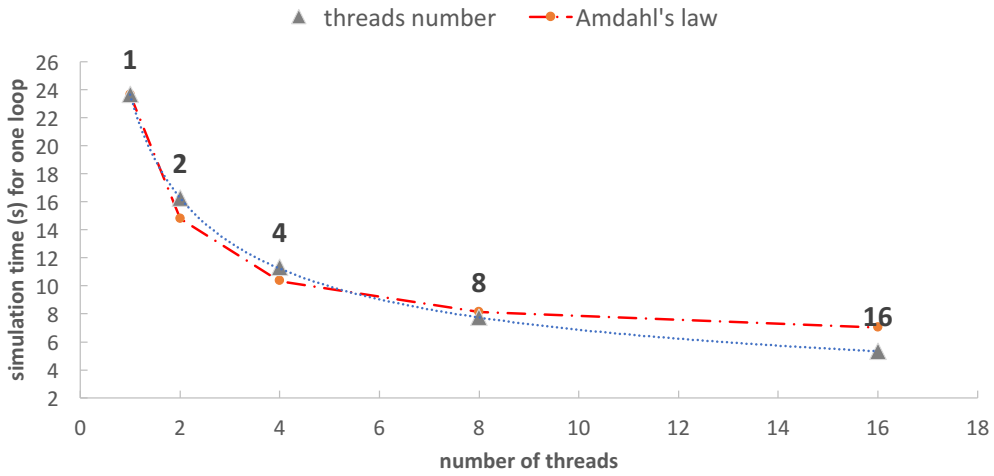

FIGURE 7.2: Taylor Green vortex test case: average simulation time for one iteration v.s. number of threads - Intel(R) Xeon(R) CPU E5-2687W, 8 core, 2 x 8 threads, RAM 64Gb.

The data shown in the graph are obtained using the two-dimensional Taylor Green Vortex test - case, in a 256 x 384 nodes domain. The calculation was performed by means of an Intel(R) Xeon(R) CPU E5-2687W v3 @ 3.10GHz, 8 core, 2 x 8 threads, RAM 64Gb DDR3.
The code has been parallelized only in the portion of the code dealing with the collision phase. The graph is based on the use of the Amdahl's law. In fact, before, the simulation times measured for the various numbers of processors have been used to obtain the (mean) parallelized fraction of the code f; the percentage obtained is $\cong 75\%$. Then, using the equation 7.1, it is possible to find the trend in equation 7.2.
It can be observed that there is a similar trend between the real parallel speed-up and the Amdahl's law, even if the asymptotic value of simulation time has not yet been reached, and, with an higher number of threads, the velocity could still increase.

Chapter 8

Case study

8.1 Introduction

The final purpose of this work was the implementation and the subsequent application of a semi-automatic procedure for modelling flood events. The lattice Boltzmann method with Cumulant CO is chosen as a numerical technique for the solution of the hydrodynamic problem. The chosen mesoscopic model, thanks to the peculiar characteristic of LBM codes of being easily parallelized also in GPGPUs, could allow to considerably reduce the calculation time compared to the classical continuous formulation. The method could allow a full wave prediction accurate and realistic, introducing the possible application for the assessment of hydraulic risk.

8.2 GIS-LB routine: pre and post processing

The preparation and the assessment of the input data (pre-processing) and the analysis of the modelling results (post-processing) are assisted by an interchange routines using the open source Qgis platform (version 2.18.14).
In pre-processing part, information derived from digital terrain model (DTM), land use and hydrological parameters are organized and geographically superimposed by means of a GIS platform.
GIS is an acronym for Geographical Information System and aims the superimposition of geographical georeferenced data characterized by attributes. In Qgis – LB routine, the Qgis platform allows to set the information related to topography, initial conditions (water depth and velocity values distribution), boundary conditions (position and type of solid and inlet/outlet boundaries), external force (value and distribution of roughness coefficients, obstacles position) and to make this data available for the execution of the numerical model. In particular, by means of a python procedure, the data set

is automatically converted in raster format with resolution coincident with the size of the calculation mesh; this allows to assign the information directly to the grid node. Once the simulation has taken place, the modelling results are exported in raster format, in order to be managed again through the Qgis platform.
The post processing allows the construction of thematic maps (i.e. flooding maps) for a fast evaluation of the hydraulic hazard, the first step in the assessment of floods risk and mitigation plans.
Figure 8.1 shows the conceptual scheme of the described procedure.

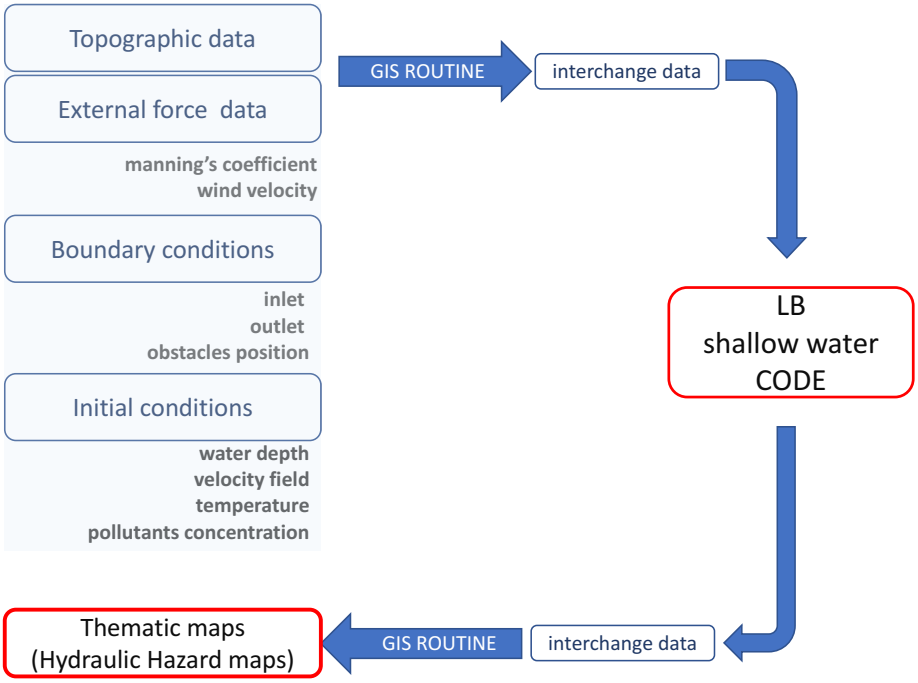

FIGURE 8.1: GIS-LBM routine: semi-automatic procedure for thematic maps of hydraulic interest (i.e. floods maps, pollutants concentration).

8.3 The Malpasset Dam break

The Malpasset dam was an arch dam built in the period from 1952 to 1954 in the Reyran River Valley, located about 12 km upstream of the Frejus in the Cote d'Azur area in the southern France. It was a doubly curved equal angle arch type with variable radius; it was initially constructed to supply water and irrigation for the region and for flood risk management, in order to manage the potential inundation hazard of the Reyran river. Downstream of the

dam, the valley has two narrow curves; then it expands, before narrowing again at the arrival to the sea.
On 21 December of 1959, the dam failed explosively giving rise to a flooding wave more than 40 m high. The wave arrived at the Frejus gulf about 21 min after the dam break. During the event, about 50 millions m^3 of water crossed the river valley down to the town of Frejus; 421 people were killed and the wave produced a damage close to $ 70 millions (Biscarini et al., 2016). Only a small portion of the dam arch still remained in its original position. Several inquests were successively managed to understand the cause of the disaster. The reports state that the engineers did not properly assessed the exceptional rainfall that occurred before the failure. Furthermore, the lack of an accurate geological survey negatively influenced the safety of the dam.
The Reyran valley morphology changed drastically, because of the strength of the flood wave caused from collapse of the dam.
The computational mesh in pre-event is due to an historical 1:20000 map, dated 1931, provided by the Institut Geographique National (IGN) and later digitized in the Laboratoire National d'Hydraulique of *EDF* (Electricité de France), (Alcrudo and Gil, 1999). The valley geometry provided by *EDF* (Hervouet, 2000) is a non-structured grid of 13000 points reported in Figure 8.2. The bounding box of the domain of interest is 17500 m wide and 10000 m high; the topographic elevation ranges from 0 to 100 m above sea level; the 100 m level is the upstream boundary condition corresponding to the initial reservoir water level. The rest of the valley is assumed to be in dry conditions although a certain discharge was flowing out of the dam at failure time.

8.3.1 Results and discussion

Several field data are available for this test case. The flood wave arrival times are available as the three hydroelectric plants along the Reyran were turned off by the flood impact. Then, maximum water depth values were registered by the police after the flooding event in about one hundred points of the right and left bank of the river valley (Hervouet and Petitjean, 1999). The uncertainty of such water elevation field data is not available. Moreover, the National Hydraulic and Environment Laboratory of *EDF* in 1964 built a 1:400 physical scale model of the case study, simulating the flood wave and measuring both water depth and arrival time values in the domain (Goutal, 1999). These field and laboratory data are utilized to verify the performances of the

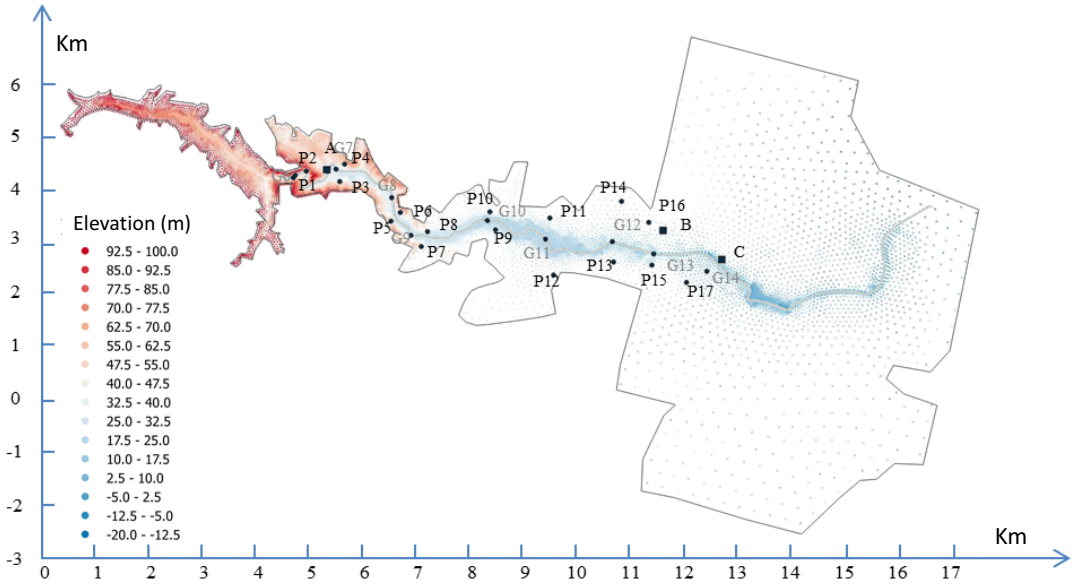

FIGURE 8.2: Map of the region of interest in a local coordinate system (reproduced from (Biscarini et al., 2016)). The points surveyed by the police after the dam break are indicated as Pi with i = 1,...,17. The gauge points of the laboratory-scale model built in the laboratory of *EDF* are indicated as Gi with i = 1,...,14. A, B and C are the Electrical Transformers (ETs) of three hydroelectric plants placed along the Reyran River.

hydraulic modelling and, in particular, efficiency and accuracy in simulating unsteady complex flood flows within domains of very complex geometry (Biscarini et al., 2016).

A transient two-dimensional simulation of the flood propagation, starting from the collapse of the dam, is performed in the entire domain (Figure 8.2). The flow is initialized with water at rest and with a 100 m water depth in the reservoir. The parameter of the CumLB simulation are: two different grid spacing Δx= 20 m and Δx= 10 m and respectively, time step Δt= 0.736 s and Δt= 0.368 s, relaxation time τ= 0.8. The friction force is based on the formula 2.10, simulated with a Manning parameter n_f=0.03 $s\ m^{-1/3}$ according to (Hervouet and Petitjean, 1999). In Table 8.1 are reported the available data of the flood wave arrival times (AT_{obs}) at the three electrical transformers, including the position of the *ET*s. The distance from each *ET* and the following one on the centreline is named Δs. The flood wave arrival time at each transformer obtained with the 2D CumLB model (grid spacing Δx=20 m) is compared with the observations. It is interesting to note that the numerical results match the surveyed data, especially at *ET*s A and C.

TABLE 8.1: Summary information of the flood wave travel time obtained at each Electrical Transformer (*ET*) A, B and C, placed downstream the dam. The flood wave arrival coincides with the shutdown time (*ST*) of each *ET*. Δs is the distance from each *ET* and the following one.

ET	X	Y	AT_{obs}	AT_{sim}	Δs
-	-	-	[s]	[s]	[m]
A	5500	4400	100	98.6	—
B	11900	3250	1240	1314	6502
C	13000	2700	1420	1465	1230

A further validation of the numerical simulation is performed at points surveyed by police, denoted as P1–P17 (Figure 8.2). The coordinates of the points Pi and the maximum water depth at observed stages are listed in Table 8.2. The maximum WS predicted by the 2D model at gauge points Pi is compared with the in situ surveys (WS_{obs}) in Table 8.2. With a grid spacing Δx=20 m, the difference between 2D model results and the field data measured by the police is less than 5% at points P1, P2, P5, P7, P8, P9, P10, P11 and P17 with a mean error of 4.7%. With a grid spacing Δx=10 m, this difference is less than 5% at points P1, P2, P3, P5, P6, P8, P9, P10 and P11 with a mean error of 4%. It can be noted that in correspondence of the points P2, P4, P5, P7, P10 and P13, where the relative error is higher for Δx=10 m than for Δx=20 m, the WS simulated results more in agreement with the model from Literature in (Valiani, Caleffi, and Zanni, 2002). In Figure 8.3 a graphical representation of the values of the water surface observed (WS_{obs}), the water surface simulated (WS_{sim}) and from literature (WS_{Lit}), listed in Table 8.2. Figures 8.4 and 8.5 show the flood hydrograph predicted by the 2D model at points P8 and P11 (left bank) and P1, P5, P9 (right bank). The dashed line shows the observed reference value (WS_{obs}). The hydrograph represents the water surface elevation as a function of time. It is interesting to note that the maximum value predicted by the model is generally very close to the one surveyed by the police after the failure break (Pi points). Table 8.3 refers to the points G6-G14, representing the arrival time AT_{lab} and the WS measured in the LNH laboratory of *EDF*. The accordance between the arrival time simulated and measured in laboratory is satisfying at almost all the points, even if the model looks generally slightly slower than the laboratory model (8.6). Figure 8.7 shows the flood hydrograph at points G10 and G13. The red line refers to the arrival time, at which the measure is taken (*AT*). Finally the

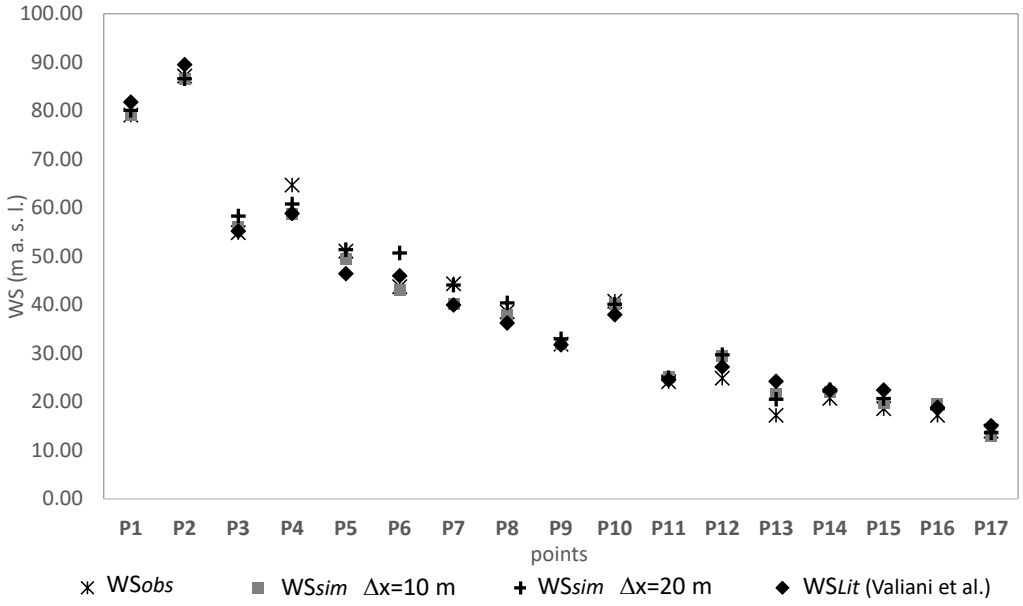

FIGURE 8.3: Comparison of the WS (m a.s.l.) between the WS_{obs}, WS_{sim}, WS_{Lit}.

TABLE 8.2: Coordinates X and Y of the points P1-P17 surveyed by the police and corresponding observed maximum Water Stage (WS_{obs}), maximum WS from numerical model (WS_{sim}) and WS_{Lit} from Literature (Valiani et al.).

PTs	X	Y	Bank	WS_{obs}	$WS20_{sim}$	$WS10_{sim}$	WS_{Lit}
P1	4913.1	4244	right	79.15	80.12	79.172	81.82
P2	5159.7	4369.6	left	87.2	86.66	86.64	89.55
P3	5790.6	4177.7	right	54.9	58.31	55.982	55.21
P4	5886.5	4503.9	left	64.7	60.8	58.735	58.84
P5	6763	3429.6	right	51.1	51.39	49.389	46.42
P6	6929.9	3591.8	left	43.75	50.7	43.048	45.98
P7	7326	2948.7	right	44.35	44.1	40.166	40
P8	7451	3232.1	left	38.6	38.7	37.808	36.26
P9	8735.9	3264.6	right	31.9	33	31.882	31.79
P10	8628.6	3604.6	left	40.75	40.14	40.111	37.99
P11	9761.1	3480.3	left	24.15	25	25.116	24.53
P12	9832.9	2414.7	right	24.9	27	29.515	27.2
P13	10957.2	2651.9	right	17.25	20.55	21.729	24.25
P14	11115.7	3800.7	left	20.7	22.52	21.978	22.4
P15	11689	2592.3	right	18.6	20.7	19.856	22.45
P16	11626	3406.8	left	17.25	18.63	19.557	18.89
P17	12333.7	2269.7	right	14	13.65	12.897	15.08

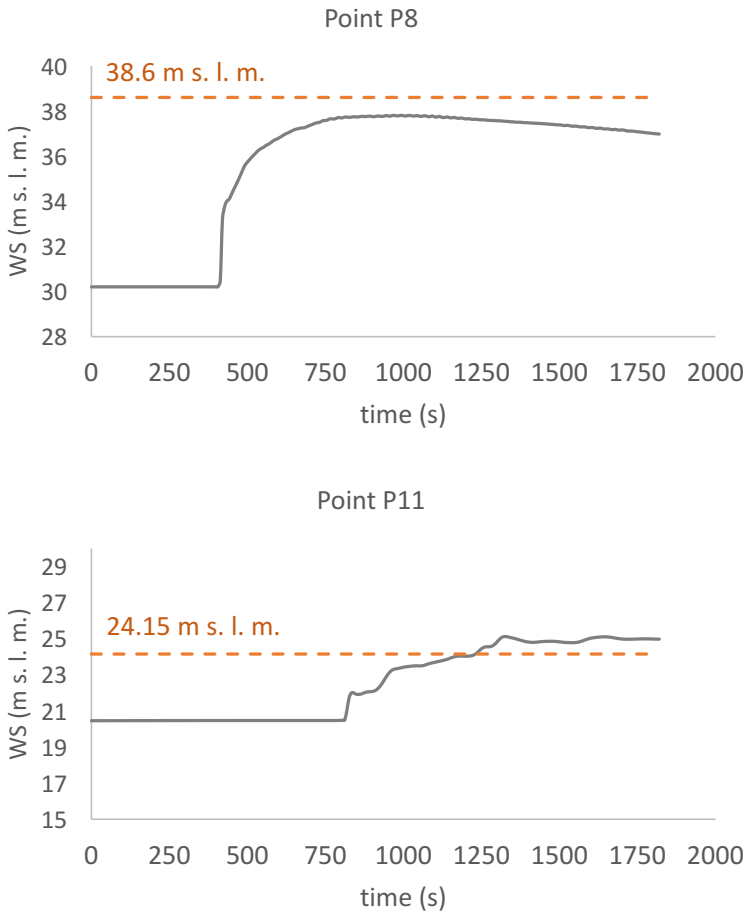

FIGURE 8.4: Water Surface hydrograph points P8 and P11 (left bank). The dashed line shows the observed WS.

TABLE 8.3: Coordinates X and Y of the points G6-G14, arrival time AT_{lab} and WS_{lab} from LNH of *EDF* and the simulated WS. Δx=20m.

PTs	X	Y	AT_{lab}	WS_{lab}	AT_{sim}
G6	4947.4	4289.7	10.2	84.2	14
G7	5717.3	4407.6	102	49.1	119
G8	6775.1	3869.2	182	54	250
G9	7128.2	3162	263	40.2	266
G10	8585.3	3443.1	404	34.9	413
G11	9675	3085.9	600	27.4	650
G12	10939.1	3044.8	845	21.5	850
G13	11724.4	2810.4	972	16.1	994
G14	12723.7	2485.1	1139	12.9	1365

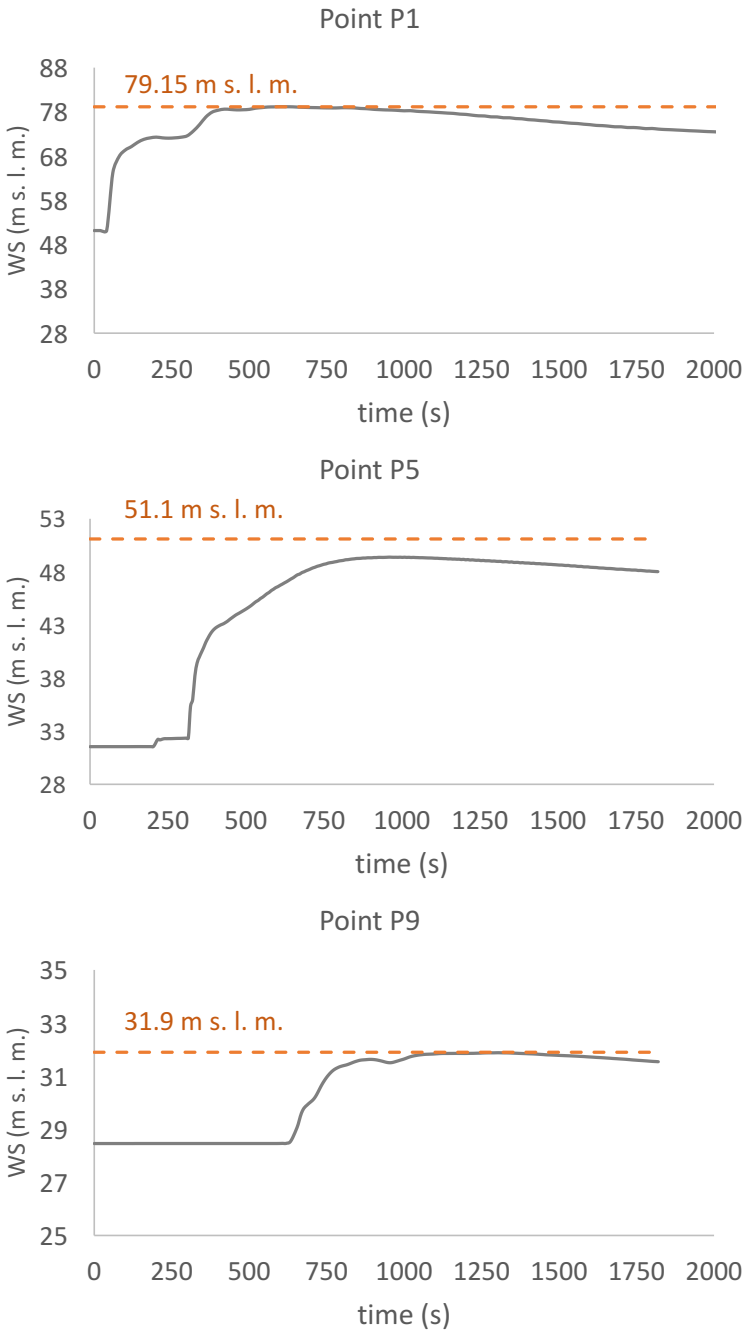

FIGURE 8.5: Water Surface hydrograph points P1, P5 and P9 (right bank). The dashed line shows the observed WS.

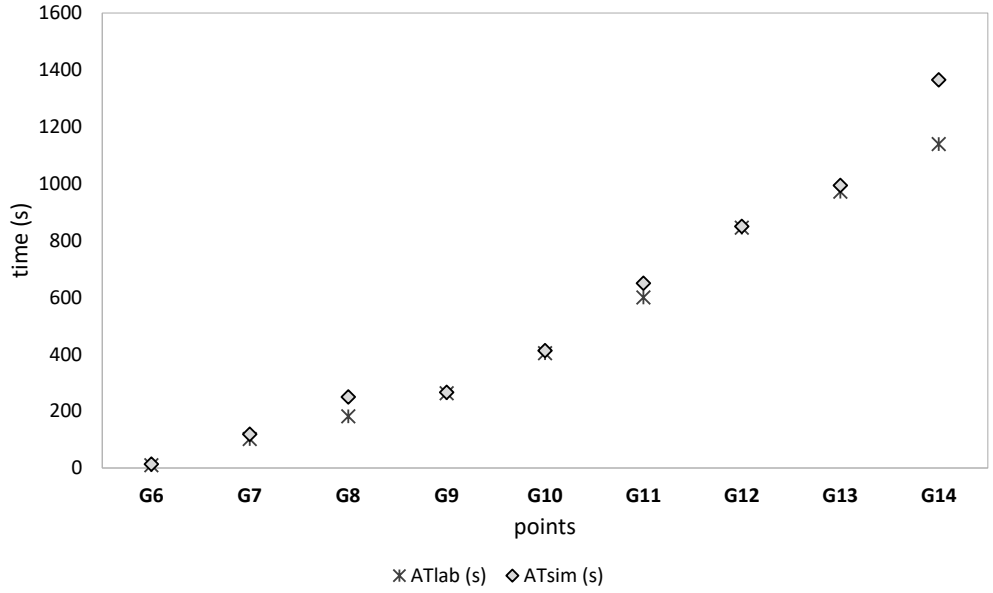

FIGURE 8.6: Comparison of the arrival time A_t (s) between the AT_{obs}, AT_{sim} at points G6, ..., G14.

wave propagation in the Reyran valley at different times (50 s, 200 s, 1500 s, 2400 s) after the collapse of the dam is given, showing the opportunity of obtaining a detailed picture of the flood event (Figure 8.8). Moreover, a three-dimensional representation at different times of the flood evolution is given in Figure 8.9. Referring to Figure 8.8, at time t=200 s after the dam collapse, the flood wave has already overtopped the yard of the A8 highway. In Figure 8.10, the flood at t=200 s is superimposed to an aerial historical image of the Malpasset area, showing the good coincidence between the water extension and the destroyed area. The flood wave has propagated towards the valley and reached the town of Frejus about 21 minutes after the rupture of the dam (see the flooded area at 1500 s). The simulation results are also consistent with the damage reported during the flood, when 3 km of the mainline rail were destroyed between 1500 s and 2000 s after the dam collapse.

It is possible to conclude that this 2D representation of the flood propagation is consistent with surveyed and laboratory data. Then, the 2D CumLB model seems suitable to be used for flood mapping, activity strictly connected to the prediction of hazard over the flooded area of a catastrophic event. Obviously, further validations with different test-case would be advantageous, in order to investigate eventual deficiencies of the model and to promote the appropriate improvements in the model.

An additional development of this study could be the identification of parameters to define how to couple 2D and 3D hydraulic models, in order to

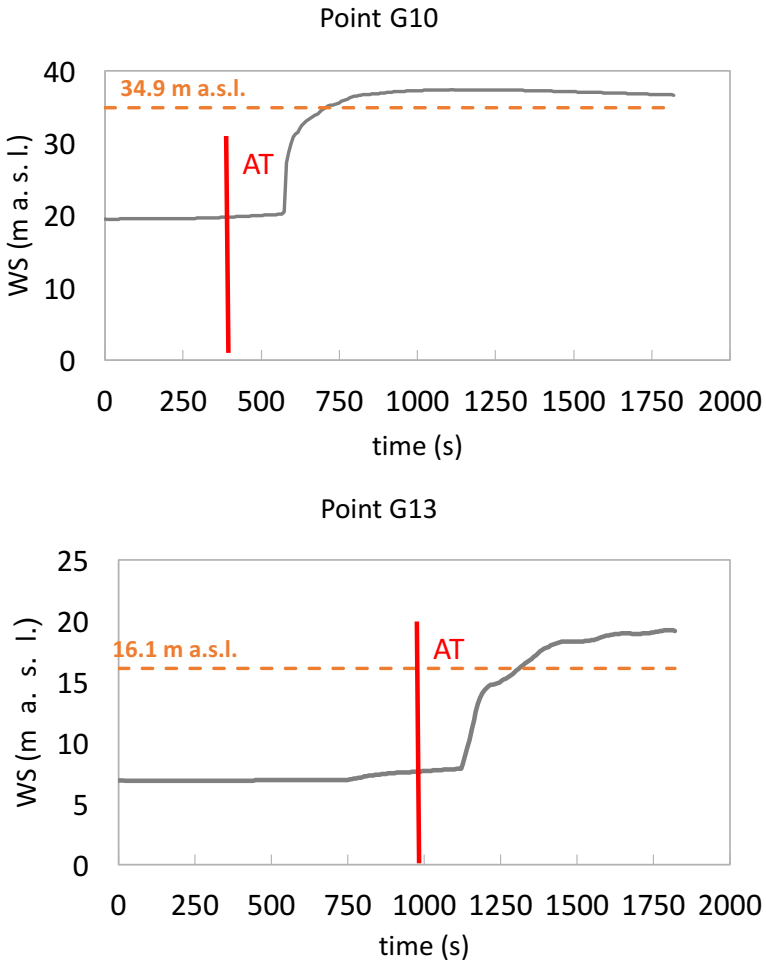

FIGURE 8.7: Comparison between AT_{lab} (red line) and AT_{sim} (hydrograph in gray line) at points G10 and G13.

make more efficient numerical simulations. In fact, 3D models allow the simulation of fairly complex phenomena, especially in meandering river channels (Biscarini et al., 2016), but are absolutely characterized by higher computational costs.

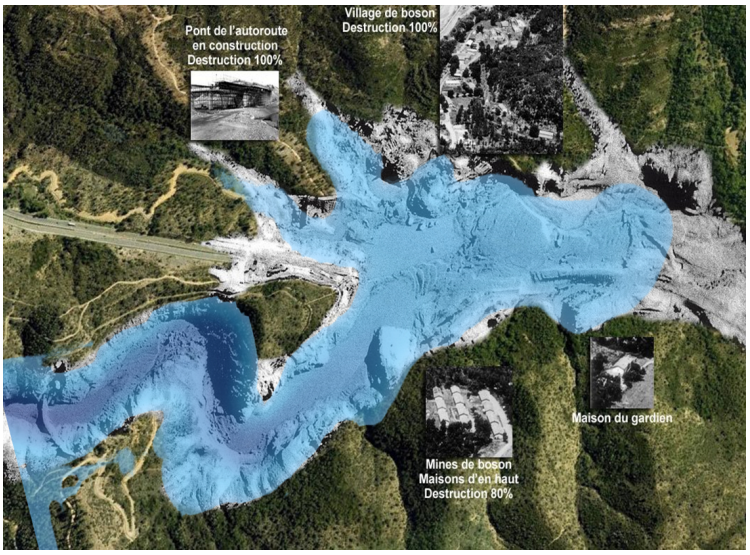

FIGURE 8.10: Comparison of simulated flood extent at t=200 s with historical aerial photo of the Malpasset area (picture from http://frejus59.fr).

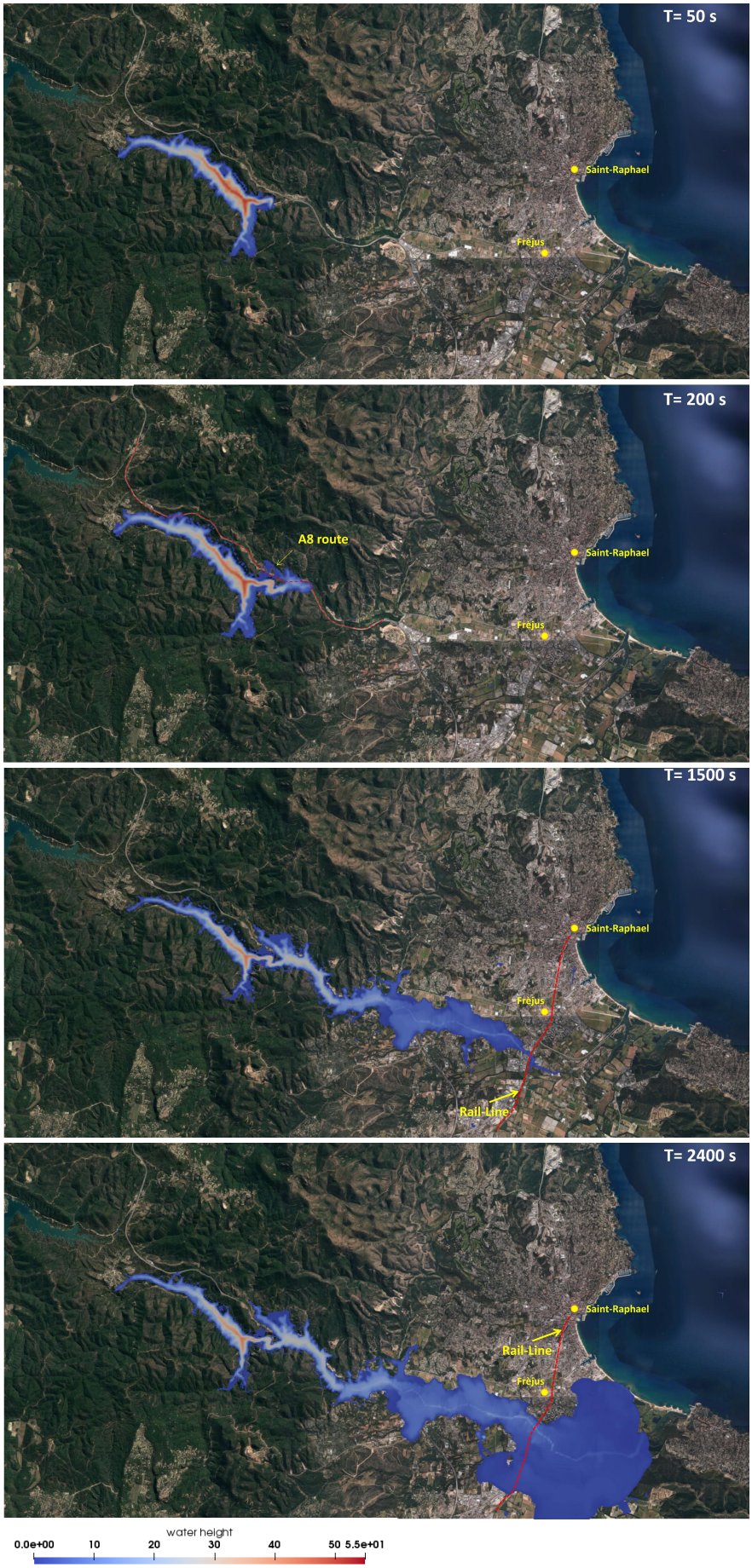

FIGURE 8.8: Flooded area at different time steps after dam break - Google Maps Orthophoto.

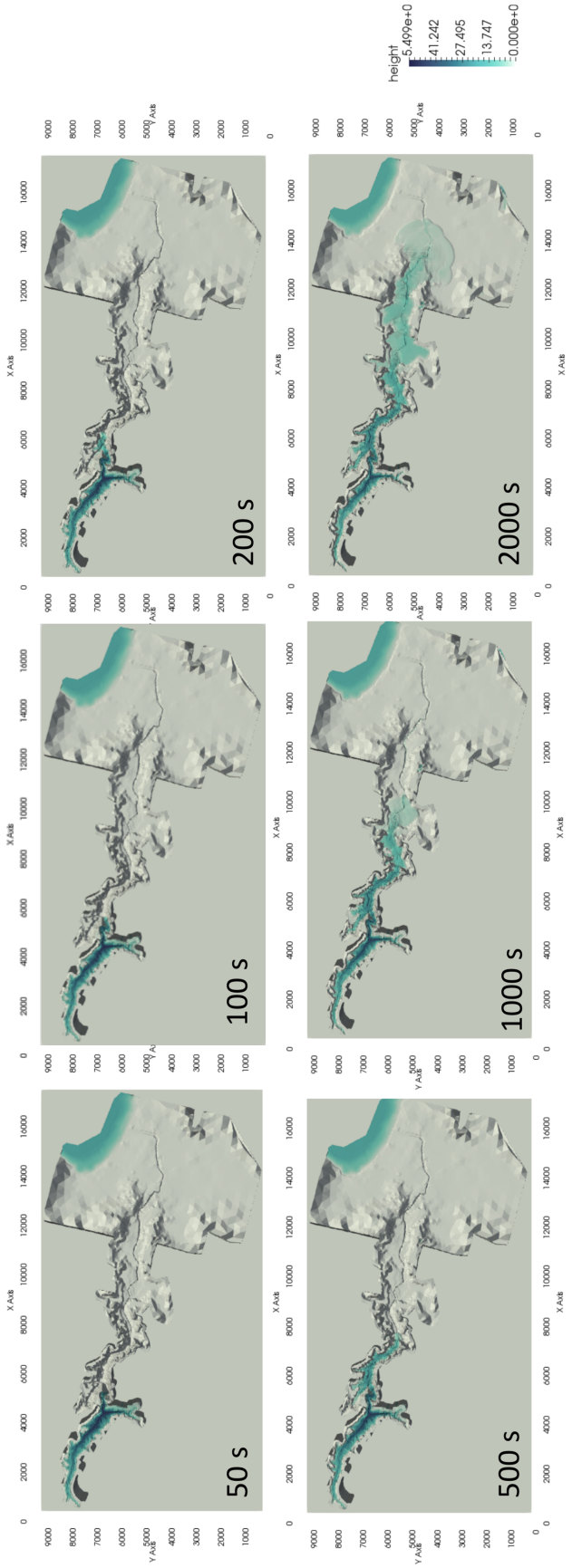

FIGURE 8.9: Malpasset flooding at 50, 100, 200, 500, 1000 and 2000 s after the dam collapse.

Conclusions

This thesis dealt with the construction, from the point of view of the theoretical perspective and implementation, of a shallow water Lattice Boltzmann model to be applied to large scale hydraulic analyses and a case study for hydraulic engineers. The LB model mainly used until now to solve the shallow water (SW) equations is based on the SRT BGK collision operator (CO). A restricted number of researchers use a multi-relaxation time CO in LB shallow water models. In this respect, this work is innovative. The present thesis examined an innovative lattice Boltzmann approach based on the use of non-conventional MRT collision operators (CO), the cascaded and the cumulant CO (respectively, CaLB and CumLB). The cascaded model, operating in a frame co-moving with the fluid, overcame the Galilean invariance violation of the standard MRT models; the model based on cumulants as observable quantities also assured the hypothesis of statistical independence between different degrees of freedom in the collision step. A convergence analysis based on the test cases of the Shear Wave and the Taylor Green vortex was performed using the diffusive scaling, that allows to maintain the simulation in the incompressible limit of the Navier Stokes equations; the accuracy and the stability of the two new presented models, CaLB and CumLB SW, was verified in comparison with the standard BGK SW model. In particular, the observation of the Taylor Green vortex test results leads to the conclusion that all models, in their stability range, show a second order accuracy in viscosity and phase error. The CaLB and CumLB present comparable characteristics, as it can be expected in a two-dimensional model. But, in comparison with the CaLB and CumLB models, the traditional BGK SW model is generally characterized by a more limited range of stability, for different depths and velocity fields. In particular, the standard BGK model is less stable for low viscosities. It is possible to conclude that the BGK model, due to its lower stability properties, seems to be less suitable to such kind of large scale analyses, that generally involve complex bed topography and complex boundary conditions, in addition to the treatment of a wide variety of external forces; this makes it necessary that the model has well determined properties of accuracy, stability and consistency. In this work, the new

models were originally described in its principal and innovative features and the main theoretical differences from the standard BGK were underlined. A particular attention was given to explain how, in the SW model, a speed of sound that depends on the water depth (a dependence that comes from the derivation of the SW from the NSE, that consider average macroscopic quantities on the vertical direction) intervenes in the definition of the equilibrium central moments/cumulants and in the collision step of the evolution equation. In fact, it is necessary to introduce the functional dependence of the speed of sound from the water depth in the relaxation rates connected to the transport parameter, in order to conserve the characteristics of isotropy of the model. The validation of the central moments and cumulants models with the external force and boundary conditions treatment was executed on 1D and 2D test cases, in stationary and non-stationary states; the simulations, in the examined conditions, gave accurate results and presented good stability characteristics. The suggested schematization of wetting-drying boundaries, based on a double limiter on the water depth and on the velocity (by means of the Froude number), gave adequate outcomes in the stationary condition, in comparison with the analytical solution of a 2D bump test case. In the unsteady case, the LB model leads to results comparable with other shallow water solvers. However, in the test-case of a dam-break over a triangular bump, the difference between experimental and simulation results highlights the insufficient suitability of a two-dimensional model to simulate condition where the three-dimensional effects are not negligible. Finally, a real flood event, the Malpasset Dam break, was simulated using the CumLB model. Such an event is of intrinsic interest, for the tragic importance of the caused damages. Moreover, this is an important test-case for the availability of experimental data and field data sets. The first results are encouraging, showing, generally, good accordance between recorded water level and simulated water level. However, the procedure should be tested considering different resolutions of the DTM (Digital Elevation Model) of the bed topography, in order to assess the accuracy of the method. Anyway, the proposed procedure is promising. The shallow water Lattice Boltzmann model method based on non-conventional CO exhibits characteristics of accuracy and stability that allow to realistically and accurately predict a flood wave, introducing the possible application for the assessment of the hydraulic risk.

Appendix A

From PDF to CMs and vice versa

In cascaded/cumulant model, the PDF is transformed into central moments/cumulants before the collision using the following equations:

$$\kappa_{00} = f_7 + f_3 + f_6 + f_4 + f_0 + f_2 + f_8 + f_1 + f_5 \tag{A.1}$$

$$\kappa_{10} = 0 \tag{A.2}$$

$$\kappa_{01} = 0 \tag{A.3}$$

$$\begin{aligned}\kappa_{20} = {} & (-1-u)^2 f_7 + (-1-u)^2 f_3 + \\ & + (-1-u)^2 f_6 + u^2 f_4 + u^2 f_0 + u^2 f_2 + \\ & + (1-u)^2 f_8 + (1-u)^2 f_1 + (1-u)^2 f_5\end{aligned} \tag{A.4}$$

$$\begin{aligned}\kappa_{02} = {} & (-1-v)^2 f_7 + v^2 f_3 + \\ & + (1-v)^2 f_6 + (-1-v)^2 f_4 + v^2 f_0 + (1-v)^2 f_2 + \\ & + (-1-v)^2 f_8 + v^2 f_1 + (1-v)^2 f_5\end{aligned} \tag{A.5}$$

$$\begin{aligned}\kappa_{11} = {} & (-1-u)(-1-v) f_7 - (-1-u) v f_3 + (-1-u)(1-v) f_6 + \\ & - u(-1-v) f_4 + uv f_0 - u(1-v) f_2 + (1-u)(-1-v) f_8 + \\ & - (1-u) v f_1 + (1-u)(1-v) f_5\end{aligned} \tag{A.6}$$

$$\begin{aligned}\kappa_{21} = {} & (-1-u)^2(-1-v)f_7 - (-1-u)^2 v f_3 + (-1-u)^2(1-v)f_6 + \\ & + u^2(-1-v)f_4 - u^2 v f_0 + u^2(1-v)f_2 + (1-u)^2(-1-v)f_8 + \\ & - (1-u)^2 v f_1 + (1-u)^2(1-v)f_5\end{aligned} \tag{A.7}$$

$$\begin{aligned}\kappa_{12} = {} & (-1-u)(-1-v)^2 f_7 + (-1-u)v^2 f_3 \\ & + (-1-u)(1-v)^2 f_6 - u(-1-v)^2 f_4 - u v^2 f_0 - u(1-v)^2 f_2 \\ & + (1-u)(-1-v)^2 f_8 + (1-u)v^2 f_1 + (1-u)(1-v)^2 f_5\end{aligned} \tag{A.8}$$

$$\begin{aligned}\kappa_{22} = {} & (-1-u)^2(-1-v)^2 f_7 + (-1-u)^2 v^2 f_3 \\ & + (-1-u)^2(1-v)^2 f_6 + u^2(-1-v)^2 f_4 + u^2 v^2 f_0 \\ & + u^2(1-v)^2 f_2 + (1-u)^2(-1-v)^2 f_8 + \\ & (1-u)^2 v^2 f_1 + (1-u)^2(1-v)^2 f_5\end{aligned} \tag{A.9}$$

After the collision, the PDF is found using the following equations:

$$\begin{aligned}f_0 = {} & -\kappa_{20} + \kappa_{22} + 2\kappa_{12}u + \kappa_{02}(-1+u^2) + 2\kappa_{21}v + 4\kappa_{11}uv + \kappa_{20}v^2 + \\ & + \kappa_{00}\left(-1+u^2\right)\left(-1+v^2\right)\end{aligned} \tag{A.10}$$

$$\begin{aligned}f_1 = {} & \frac{1}{2}\left(\kappa_{20} - \kappa_{22} + \kappa_{00}u - \kappa_{02}u + \right. \\ & + \kappa_{00}u^2 - \kappa_{02}u^2 + \\ & \left. - \kappa_{12}(1+2u) - 2\kappa_{11}v - 2\kappa_{21}v - 4\kappa_{11}uv - \kappa_{20}v^2 - \kappa_{00}uv^2 - \kappa_{00}u^2v^2\right)\end{aligned} \tag{A.11}$$

$$\begin{aligned}f_2 = {} & \frac{1}{2}\left(\kappa_{02} - \kappa_{22} - 2\kappa_{11}u - 2\kappa_{12}u + \right. \\ & - \kappa_{02}u^2 + \kappa_{00}v - \kappa_{20}v - 4\kappa_{11}uv + \\ & \left. - \kappa_{00}u^2v + \kappa_{00}v^2 - \kappa_{20}v^2 - \kappa_{00}u^2v^2 - \kappa_{21}\left(1+2v\right)\right)\end{aligned} \tag{A.12}$$

$$f_3 = \frac{1}{2}\Big(\kappa_{12} + \kappa_{20} - \kappa_{22} - \kappa_{00}u + \kappa_{02}u - 2\kappa_{12}u + \kappa_{00}u^2 + \\ -\kappa_{02}u^2 + 2\kappa_{11}v - 2\kappa_{21}v - 4\kappa_{11}uv - \kappa_{20}v^2 + \kappa_{00}uv^2 - \kappa_{00}u^2v^2\Big) \tag{A.13}$$

$$f_4 = \frac{1}{2}\Big(\kappa_{02} + k21 - \kappa_{22} + 2\kappa_{11}u - 2\kappa_{12}u - \kappa_{02}u^2 - \kappa_{00}v + \kappa_{20}v - 2\kappa_{21}v + \\ -4\kappa_{11}uv + \kappa_{00}u^2v + \kappa_{00}v^2 - \kappa_{20}v^2 - \kappa_{00}u^2v^2\Big) \tag{A.14}$$

$$f_5 = \frac{1}{4}\Big(\kappa_{12} + \kappa_{21} + \kappa_{22} + \kappa_{02}u + 2\kappa_{12}u + \kappa_{02}u^2 + \kappa_{20}v + 2\kappa_{21}v + \\ +\kappa_{00}uv + \kappa_{00}u^2v + \kappa_{20}v^2 + \kappa_{00}uv^2 + \\ +\kappa_{00}u^2v^2 + \kappa_{11}\left(1+2u\right)\left(1+2v\right)\Big) \tag{A.15}$$

$$f_6 = \frac{1}{4}\Big(\kappa_{21} + \kappa_{22} - \kappa_{02}u + \kappa_{02}u^2 + \kappa_{12}(-1+2u) + \kappa_{20}v + 2\kappa_{21}v + \\ -\kappa_{00}uv + \kappa_{00}u^2v + \kappa_{20}v^2 - \kappa_{00}uv^2 + \\ +\kappa_{00}u^2v^2 + \kappa_{11}\left(-1+2u\right)\left(1+2v\right)\Big) \tag{A.16}$$

$$f_7 = \frac{1}{4}\Big(-\kappa_{21} + \kappa_{22} - \kappa_{02}u + \kappa_{02}u^2 + \kappa_{12}\left(-1+2u\right) - \kappa_{20}v + \\ +2\kappa_{21}v + \kappa_{00}uv - \kappa_{00}u^2v + \kappa_{20}v^2 - \kappa_{00}uv^2 + \\ +\kappa_{00}u^2v^2 + \kappa_{11}\left(-1+2u\right)\left(-1+2v\right)\Big) \tag{A.17}$$

$$f_8 = \frac{1}{4}\Big(\kappa_{12} - \kappa_{21} + \kappa_{22} + \kappa_{02}u + 2\kappa_{12}u + \kappa_{02}u^2 - \kappa_{20}v + 2\kappa21v + \\ -\kappa_{00}uv - \kappa_{00}u^2v + \kappa_{20}v^2 + \kappa_{00}uv^2 + \\ +\kappa_{00}u^2v^2 + \kappa_{11}\left(1+2u\right)\left(-1+2v\right)\Big) \tag{A.18}$$

Appendix B

From PDF to CMs and vice versa - with external force

In cascaded/cumulant model with external force, the PDF is transformed into central moments/cumulants before the collision using equations that differ from the one in Appendix A only for the moments/cumulants κ_{10} and κ_{01}:

$$\begin{aligned}\kappa_{10} = &-f_0 u + f_1(1-u) - f_2 u + f_3(-u-1) - f_4 u + f_5(1-u) + \\ &+ f_6(-u-1) + f_7(-u-1) + f_8(1-u)\end{aligned} \tag{B.1}$$

$$\begin{aligned}\kappa_{01} = &-f_0 v - f_1 v + f_2(1-v) - f_3 v + f_4(-v-1) + f_5(1-v) + \\ &+ f_6(1-v) + f_7(-v-1) + f_8(-v-1)\end{aligned} \tag{B.2}$$

In the previous equations B.1 and B.2 the velocities are calculated using the relations in section 3.22. After the collision, the PDF is found from central moments/cumulants using the following equations:

$$\begin{aligned}f_0 = &\kappa_{00}\left(u^2-1\right)\left(v^2-1\right) + 2\kappa_{01}u^2 v - 2\kappa_{01}v + \kappa_{02}\left(u^2-1\right) + \\ &+ 2\kappa_{10}uv^2 - 2\kappa_{10}u + 4\kappa_{11}uv + 2\kappa_{12}u + \kappa_{20}v^2 - \kappa_{20} + 2\kappa_{21}v + \kappa_{22}\end{aligned} \tag{B.3}$$

$$\begin{aligned}f_1 = &\frac{1}{2}\left(-\kappa_{00}u^2v^2 + \kappa_{00}u^2 - \kappa_{00}uv^2\right) + \\ &+ \frac{1}{2}\left(\kappa_{00}u - 2\kappa_{01}u^2 v - 2\kappa_{01}uv - \kappa_{02}u^2 - \kappa_{02}u\right) + \\ &+ \frac{1}{2}(-\kappa_{10}(2u+1)\left(v^2-1\right) - 4\kappa_{11}uv - 2\kappa_{11}v) + \\ &+ \frac{1}{2}\left(-\kappa_{12}(2u+1) - \kappa_{20}v^2 + \kappa_{20} - 2\kappa_{21}v - \kappa_{22}\right)\end{aligned} \tag{B.4}$$

$$
\begin{aligned}
f_2 = & \frac{1}{2}\left(-\kappa_{00}u^2v^2 - \kappa_{00}u^2v + \kappa_{00}v^2\right) + \\
& + \frac{1}{2}\left(\kappa_{00}v - \kappa_{01}\left(u^2-1\right)(2v+1) - \kappa_{02}u^2 + \kappa_{02} - 2\kappa_{10}uv^2\right) + \\
& + \frac{1}{2}\left(-2\kappa_{10}uv - 4\kappa_{11}uv - 2\kappa_{11}u - 2\kappa_{12}u\right) + \\
& + \frac{1}{2}\left(-\kappa_{20}v^2 - \kappa_{20}v - 2\kappa_{21}v - \kappa_{21} - \kappa_{22}\right)
\end{aligned}
\tag{B.5}
$$

$$
\begin{aligned}
f_3 = & \frac{1}{2}\left(-\kappa_{00}u^2v^2 + \kappa_{00}u^2 + \kappa_{00}uv^2 - \kappa_{00}u - 2\kappa_{01}u^2v\right) + \\
& + \frac{1}{2}\left(2\kappa_{01}uv - \kappa_{02}u^2 + \kappa_{02}u - \kappa_{10}(2u-1)\left(v^2-1\right)\right) + \\
& + \frac{1}{2}\left(-4\kappa_{11}uv + 2\kappa_{11}v - 2\kappa_{12}u + \kappa_{12} - \kappa_{20}v^2 + \kappa_{20} - 2\kappa_{21}v - \kappa_{22}\right)
\end{aligned}
\tag{B.6}
$$

$$
\begin{aligned}
f_4 = & \frac{1}{2}\left(-\kappa_{00}u^2v^2 + \kappa_{00}u^2v + \kappa_{00}v^2 - \kappa_{00}v - \kappa_{01}\left(u^2-1\right)(2v-1)\right) + \\
& + \frac{1}{2}\left(-\kappa_{02}u^2 + \kappa_{02} - 2\kappa_{10}uv^2 + 2\kappa_{10}uv - 4\kappa_{11}uv\right) + \\
& + \frac{1}{2}\left(2\kappa_{11}u - 2\kappa_{12}u - \kappa_{20}v^2 + \kappa_{20}v - 2\kappa_{21}v + \kappa_{21} - \kappa_{22}\right)
\end{aligned}
\tag{B.7}
$$

$$
\begin{aligned}
f_5 = & \frac{1}{2}\left(\kappa_{00}u^2v^2 + \kappa_{00}u^2v + \kappa_{00}uv^2 + \kappa_{00}uv + 2\kappa_{01}u^2v + \kappa_{01}u^2 + 2\kappa_{01}uv\right) + \\
& + \frac{1}{2}\left(\kappa_{01}u + \kappa_{02}u^2 + \kappa_{02}u + 2\kappa_{10}uv^2 + 2\kappa_{10}uv\right) + \\
& + \frac{1}{2}\left(\kappa_{10}v^2 + \kappa_{10}v + \kappa_{11}(2u+1)(2v+1)\right) + \\
& + \frac{1}{2}\left(2\kappa_{12}u + \kappa_{12} + \kappa_{20}v^2 + \kappa_{20}v + 2\kappa_{21}v + \kappa_{21} + \kappa_{22}\right)
\end{aligned}
\tag{B.8}
$$

$$
\begin{aligned}
f_6 = & \frac{1}{4}\left(\kappa_{00}u^2v^2 + \kappa_{00}u^2v - \kappa_{00}uv^2 - \kappa_{00}uv + 2\kappa_{01}u^2v + \kappa_{01}u^2\right) + \\
& + \frac{1}{4}\left(-2\kappa_{01}uv - \kappa_{01}u + \kappa_{02}u^2 - \kappa_{02}u + 2\kappa_{10}uv^2 + 2\kappa_{10}uv - \kappa_{10}v^2 - \kappa_{10}v\right) + \\
& + \frac{1}{4}\left(\kappa_{11}(2u-1)(2v+1) + \kappa_{12}(2u-1) + \kappa_{20}v^2 + \kappa_{20}v + 2\kappa_{21}v + \kappa_{21} + \kappa_{22}\right)
\end{aligned}
\tag{B.9}
$$

$$f_7 = \frac{1}{4}\left(\kappa_{00}u^2v^2 - \kappa_{00}u^2v - \kappa_{00}uv^2 + \kappa_{00}uv + 2\kappa_{01}u^2v - \kappa_{01}u^2 - 2\kappa_{01}uv\right) + \\ + \frac{1}{4}\left(\kappa_{01}u + \kappa_{02}u^2 - \kappa_{02}u + 2\kappa_{10}uv^2 - 2\kappa_{10}uv - \kappa_{10}v^2 + \kappa_{10}v\right) + \\ + \frac{1}{4}\left(\kappa_{11}(2u-1)(2v-1) + \kappa_{12}(2u-1) + \kappa_{20}v^2 - \kappa_{20}v + 2\kappa_{21}v - \kappa_{21} + \kappa_{22}\right) \tag{B.10}$$

$$f_8 = \frac{1}{4}\left(\kappa_{00}u^2v^2 - \kappa_{00}u^2v + \kappa_{00}uv^2 - \kappa_{00}uv + 2\kappa_{01}u^2v - \kappa_{01}u^2\right) + \\ + \frac{1}{4}\left(2\kappa_{01}uv - \kappa_{01}u + \kappa_{02}u^2 + \kappa_{02}u + 2\kappa_{10}uv^2 - 2\kappa_{10}uv + \kappa_{10}v^2 - \kappa_{10}v\right) + \\ + \frac{1}{4}\left(\kappa_{11}(2u+1)(2v-1) + 2\kappa_{12}u + \kappa_{12} + \kappa_{20}v^2 - \kappa_{20}v + 2\kappa_{21}v - \kappa_{21} + \kappa_{22}\right) \tag{B.11}$$

In order to effectively apply the force, the central moments/cumulants κ_{10} and κ_{01} in equations B.1 and B.2 have to change the sign. In fact, half of the force is applied before the collision and half after the collision. The method is symmetric in time and then second order accurate in time (Geier et al., 2015).

Bibliography

Alcrudo, Francisco and Pilar Garcia-Navarro (1993). "A high-resolution Godunov-type scheme in finite volumes for the 2D shallow-water equations". In: *International Journal for Numerical Methods in Fluids* 16.6, pp. 489–505.

Alcrudo, Francisco and Elena Gil (1999). "The Malpasset dam break case study". In: *High Performance Computing in Science and Engineering '14*. Proceedings of the Fourth CADAM Meeting, Zaragoza, Spain, pp. 95–109.

Banari, Amir et al. (2014). "Efficient GPGPU implementation of a lattice Boltzmann model for multiphase flows with high density ratios". In: *Computers and Fluids* 93, pp. 1–17. ISSN: 00457930. DOI: 10.1016/j.compfluid.2014.01.004.

Benkhaldoun, Fayssal, Imad Elmahi, and Mohammed Seaïd (2010). "A new finite volume method for flux-gradient and source-term balancing in shallow water equations". In: *Computer Methods in Applied Mechanics and Engineering* 199.49, pp. 3324–3335.

Benkhaldoun, Fayssal, Imad Elmahi, Mohammed Seaid, et al. (2007). "Well-balanced finite volume schemes for pollutant transport by shallow water equations on unstructured meshes". In: *Journal of computational physics* 226.1, pp. 180–203.

Bermudez, Alfredo and Ma Elena Vazquez (1994). "Upwind methods for hyperbolic conservation laws with source terms". In: *Computers & Fluids* 23.8, pp. 1049–1071. ISSN: 0045-7930.

Bhatnagar, P. L., E. P. Gross, and M. Krook (1954). "A Model for Collision Processes in Gases. I. Small Amplitude Processes in Charged and Neutral One-Component Systems". In: *Phys. Rev.* 94 (3), pp. 511–525.

Biscarini, Chiara, Silvia Di Francesco, and Piergiorgio Manciola (2010). "CFD modelling approach for dam break flow studies". In: *Hydrol. Earth Syst. Sci* 14, pp. 705–718.

Biscarini, Chiara et al. (2016). "On the Simulation of Floods in a Narrow Bending Valley: The Malpasset Dam Break Case Study". In: *Water* 8.11, p. 545.

Boltzmann, Ludwig (1872). *Further Studies on the Thermal Equilibrium of Gas Molecules. Kinetic Theory*, 2:88–175.

Boltzmann, Ludwig (1896). *Vorlesungen über Gastheorie*. Vol. 1.

Brocchini, Maurizio and Nicholas Dodd (2008). "Nonlinear Shallow Water Equation Modeling for Coastal Engineering". In: 134.

Buick, JM and CA Greated (2000). "Gravity in a lattice Boltzmann model". In: *Physical Review E* 61.5, p. 5307.

Chen, Shiyi and Gary D. Doolen (1998). "Lattice boltzmann Method for Fluid Flow". In: *Annual Review of Fluid Mechanics* 30.1, pp. 329–364.

Christopher J.Roy (2005). "Review of code and solution verification procedures for computational simulation". In: *Journal of Computational Physics* 205.1, pp. 131–156. ISSN: 0021-9991. DOI: 10.1016/J.JCP.2004.10.036.

D 'Humieres, Dominique et al. (2002). "Multiple-relaxation-time Lattice Boltzmann Models in 3D". In: *Philosophical Transactions of the Royal Society of London A: Mathematical, Physical and Engineering Sciences* 360.1792, pp. 437–451.

De Rosis, Alessandro (2017). "A central moments-based lattice Boltzmann scheme for shallow water equations". In: *Comput. Methods Appl. Mech. Engrg.* 319, pp. 379–392. ISSN: 0045-7825. DOI: http://dx.doi.org/10.1016/j.cma.2017.03.001.

Delestre, Olivier et al. (2013). "SWASHES: A compilation of shallow water analytic solutions for hydraulic and environmental studies". In: *International Journal for Numerical Methods in Fluids* 72.3, pp. 269–300. ISSN: 02712091. DOI: 10.1002/fld.3741. arXiv: arXiv:1110.0288v3.

Dellar, Paul J. (2002). "Nonhydrodynamic modes and a priori construction of shallow water lattice Boltzmann equations". In: *Physical Review E - Statistical, Nonlinear, and Soft Matter Physics* 65.3. ISSN: 15393755. DOI: 10.1103/PhysRevE.65.036309.

D'Humières, Dominique (1994). "Generalized lattice-Boltzmann equations". In: *Progress in Astronautics and Aeronautics* 159, pp. 450–450.

Di Francesco, Silvia, Chiara Biscarini, and Piergiorgio Manciola (2015). "Numerical simulation of water free-surface flows through a front-tracking lattice Boltzmann approach". In: *Journal of Hydroinformatics* 17.1, p. 1. ISSN: 1464-7141. DOI: 10.2166/hydro.2014.028.

Dupré, Maurice J (2010). *TRANSFORMS AND MOMENT GENERATING FUNCTIONS*. Tech. rep.

Falcucci, Giacomo, Stefano Ubertini, and Sauro Succi (2010). "Lattice Boltzmann simulations of phase-separating flows at large density ratios: the case of doubly-attractive pseudo-potentials". In: *Soft Matter* 6.18, pp. 4357–4365.

Fennema, Robert J and M Hanif Chaudhry (1990). "Explicit methods for 2-D transient free surface flows". In: *Journal of Hydraulic Engineering* 116.8, pp. 1013–1034.

Frandsen, J.B. (2008). "A simple LBE wave runup model". In: *Progress in Computational Fluid Dynamics, An International Journal* 8.January 2008, p. 222. DOI: 10.1504/PCFD.2008.018093.

Gallivan, Martha A. et al. (1997). "An evaluation of the bounce back boundary condition for lattice Boltzmann simulations". In: *International Journal for Numerical Methods in Fluids* 25.3, pp. 249–263. ISSN: 0271-2091. DOI: 10.1002/(SICI)1097-0363(19970815)25:3<249::AID-FLD546>3.0.CO;2-7.

Geier, M (2006). "Ab initio derivation of the cascaded Lattice Boltzmann Automaton". PhD thesis. University of Freiburg.

Geier, M., A. Fakhari, and T. Lee (2015). "Conservative phase-field lattice Boltzmann model for interface tracking equation". In: *PHYSICAL REVIEW E* 91.063309. DOI: 10.1103/PhysRevE.91.063309.

Geier, M, A Greiner, and JG Korvink (2009). "A factorized central moment lattice Boltzmann method". In: *The European Physical Journal-Special Topics* 171.1, pp. 55–61.

Geier, Martin, Andreas Greiner, and Jan G Korvink (2006). "Cascaded digital lattice Boltzmann automata for high Reynolds number flow". In: *Physical Review E* 73.6, p. 066705.

Geier, Martin and Andrea Pasquali (2018). *Fourth order Galilean invariance for the lattice Boltzmann method*. Tech. rep., pp. 139–151.

Geier, Martin, Andrea Pasquali, and Martin Schönherr (2017). "Parametrization of the cumulant lattice Boltzmann method for fourth order accurate diffusion part I: Derivation and validation". In: *Journal of Computational Physics* 348, pp. 862–888. DOI: 10.1016/j.jcp.2017.05.040.

Geier, Martin et al. (2015). "The cumulant lattice Boltzmann equation in three dimensions: Theory and validation". In: *Computers & Mathematics with Applications* 70.4, pp. 507–547. DOI: 10.1016/j.camwa.2015.05.001.

George, David L (2006). "Finite volume methods and adaptive refinement for global tsunami propagation and local inundation". PhD thesis. University of Washington.

Geveler, Markus et al. (2011). "Lattice-boltzmann simulation of the shallow-water equations with fluid-structure interaction on multi-and manycore processors". In: *Facing the MulticoreChallenge, volume 6310 of Lecture Notes in Computer Science*. Springer Berlin/Heidelberg, pp. 92–104.

Ginzbourg, I. and P. M. Adler (1994). "Boundary flow condition analysis for the three-dimensional lattice Boltzmann model". In: *Journal de Physique II* 4.2, pp. 191–214. ISSN: 1155-4312. DOI: 10.1051/jp2:1994123.

Ginzburg, Irina and Dominique d'Humieres (2003). "Multireflection boundary conditions for lattice Boltzmann models". In: *Phys. Rev. E* 68 (6), p. 066614.

Goutal, Nicole (1999). "The Malpasset dam failure. An overview and test case definition". In: *Proceedings of the 4th CADAM Meeting, Zaragoza, Spain, 18-19 November*.

He, Xiaoyi et al. (1997). "Analytic solutions of simple flows and analysis of nonslip boundary conditions for the lattice Boltzmann BGK model". In: *Journal of Statistical Physics* 87.1-2, pp. 115–136. ISSN: 0022-4715.

Hervouet, J M. (2000). "A high resolution 2-D dam-break model using parallelization". In: *Hydrological Processes* 14.13, pp. 2211–2230.

Hervouet, Jean-Michel and Alain Petitjean (1999). "Malpasset dam-break revisited with two-dimensional computations". In: *Journal of Hydraulic Research* 37.6, pp. 777–788.

Huynh, Van Long, Nicholas Dodd, and Fangfang Zhu (2017). "Coastal morphodynamical modelling in nonlinear shallow water framework using a coordinate transformation method". In: 107.

Janssen, Christian F, Stephan T Grilli, Manfred Krafczyk, et al. (2012). "Efficient simulations of long wave propagation and runup using a LBM approach on GPGPU hardware". In: *The Twenty-second International Offshore and Polar Engineering Conference*. International Society of Offshore and Polar Engineers.

Junk, Michael and Zhaoxia Yang (2005). "Asymptotic Analysis of Lattice Boltzmann Boundary Conditions". In: *Journal of Statistical Physics* 121.1-2, pp. 3–35. ISSN: 0022-4715.

Kian Far, Ehsan et al. (2016a). "Distributed cumulant lattice Boltzmann simulation of the dispersion process of ceramic agglomerates". In: *Journal of Computational Methods in Sciences and Engineering* 16.2, pp. 231–252.

— (2016b). "Distributed cumulant lattice Boltzmann simulation of the dispersion process of ceramic agglomerates". In: *Journal of Computational Methods in Sciences and Engineering* 16.2, pp. 231–252.

Krafczyk, Manfred et al. (2015). "DNS/LES Studies of Turbulent Flows Based on the Cumulant Lattice Boltzmann Approach". In: *High Performance Computing in Science and Engineering '14*, pp. 519–531. DOI: 10.1007/978-3-319-10810-0_34.

Krüger, T., F. Varnik, and D. Raabe (2010). "Second - order convergence of the deviatoric stress tensor in the standard Bhatnagar - Gross - Krook lattice Boltzmann method". In: *Physical Review E - Statistical, Nonlinear, and Soft Matter Physics* 82.2, p. 025701.

Krüger, T. et al. (2016). *The Lattice Boltzmann Method, Principles and Practice*. Springer - Switzerland, p. 694.

La Rocca, Michele et al. (2015). "A multispeed Discrete Boltzmann Model for transcritical 2D shallow water flows". In: *J. Comput. Phys.* 284, pp. 117–132.

Lallemand, Pierre and Li-Shi Luo (2000). "Theory of the lattice Boltzmann method: Dispersion, dissipation, isotropy, Galilean invariance, and stability". In: *Physical Review E* 61.6, p. 6546.

Latt, Jonas et al. (2008). "Straight velocity boundaries in the lattice Boltzmann method". In: *Phys. Rev. E* 77 (5), p. 056703.

LeVeque, RJ (1996). *Finite Difference Methods for Ordinary and Partial Differential Equations*. Society for Industrial and Applied Mathematics, Philadelphia, p. 341. ISBN: 9780898716290.

Li-Luo, Shi (1998). "A unified theory of non-ideal gas lattice Boltzmann models". In:

Liu, H. and J. G. Zhou (2014). "Lattice Boltzmann approach to simulating a wetting–drying front in shallow flows". In: *Journal of Fluid Mechanics* 743.February 2014, pp. 32–59. ISSN: 0022-1120. DOI: 10.1017/jfm.2013.682.

Liu, Haifei (2009). "Lattice Boltzmann Simulations for Complex Shallow Water Flows". PhD thesis. University of Liverpool.

Luo, Li-Shi (1993). "Lattice-gas automata and lattice Boltzmann equations for two-dimensional hydrodynamics". PhD thesis. Georgia Institute of Technology.

Lynett, Patrick J., Tso Ren Wu, and Philip L F Liu (2002). "Modeling wave runup with depth-integrated equations". In: *Coastal Engineering* 46.2, pp. 89–107.

Madsen, P.A. and H.A. Sorensen O.R. Schaffer (1997). "Surf zone dynamics simulated by a Boussinesq type model. Part I. Model description and cross-shore motion of regular waves". In: *Coastal Engineering* 32.4, pp. 255–287. ISSN: 0378-3839. DOI: https://doi.org/10.1016/S0378-3839(97)00028-8.

Meselhe, E. A., F. Sotiropoulos, and F. M. Holly (1997). "Numerical Simulation of Transcritical Flow in Open Channels". In: *Journal of Hydraulic Engineering* 123.9, pp. 774–783. ISSN: 0733-9429.

Pasquali, A., M. Geier, and Krafczyk M. (2017). "Near-wall treatment for the simulation of turbulent flow by the cumulant lattice Boltzmann method". In: *Computers & Mathematics with Applications*.

Pasquali, Andrea (2017). "Enabling the cumulant lattice Boltzmann method for complex CFD engineering problems". PhD thesis. Technical University of Braunschweig.

Peng, Yong (2012). "Lattice Boltzmann Simulations of Environmental Flow Problems in Shallow Water Flows". PhD thesis.

Prestininzi, Pietro, Valentina Lombardi, and Michele La Rocca (2016). "Curved boundaries in multi-layer Shallow Water Lattice Boltzmann Methods: bounce back versus immersed boundary". In: *Journal of Computational Science* 16, pp. 16–28.

Prestininzi, Pietro, Giampiero Sciortino, and Michele La Rocca (2013). "On the effect of the intrinsic viscosity in a two-layer shallow water lattice Boltzmann model of axisymmetric density currents". In: *Journal of Hydraulic Research* 51.6, pp. 668–680.

Qian, Y. H., D. D'Humières, and P. Lallemand (1992). "Lattice BGK Models for Navier-Stokes Equation". In: *EPL (Europhysics Letters)* 17.6, p. 479.

Que, Yin-Tik and Kun Xu (2006). "The numerical study of roll-waves in inclined open channels and solitary wave run-up". In: *International Journal for Numerical Methods in Fluids* 50.9, pp. 1003–1027. ISSN: 0271-2091. DOI: 10.1002/fld.1102.

Randall J.LeVeque (1998). "Balancing Source Terms and Flux Gradients in High-Resolution Godunov Methods: The Quasi-Steady Wave-Propagation Algorithm". In: *Journal of Computational Physics* 146.1, pp. 346–365. ISSN: 0021-9991. DOI: 10.1006/JCPH.1998.6058.

Salmon, Rick (1999). "The lattice Boltzmann method as a basis for ocean circulation modeling". In: *Journal of Marine Research* 57.3, pp. 503–535.

Schönherr, M et al. (2011). "Multi-thread implementations of the lattice Boltzmann method on non-uniform grids for CPUs and GPUs". In: *Computers & Mathematics with Applications* 61, pp. 3730–3743. DOI: 10.1016/j.camwa.2011.04.012.

Shafiai, S. H. (2011). "Lattice Boltzmann method for simulating shallow free surface flows involving wetting and drying". PhD thesis. University of Liverpool.

Shan, X and H Chen (1994). "Simulation of non ideal gases and gas-liquid phase transitions by the lattice Boltzmann Equation". In: *Phys. Rev. E* 49.4, p. 697.

Soares Frazao, S (2000). "Dam-break induced flows in complex topographies. Theoretical, numerical and experimental approaches". PhD thesis.

Stansby, P. K. and J. G. Zhou (1998). "Shallow-water flow solver with non-hydrostatic pressure: 2D vertical plane problems". In: *International Journal for Numerical Methods in Fluids* 28.3, pp. 541–563. ISSN: 0271-2091.

Stoker J. J. (1957). *Water Waves: The Mathematical Theory with Applications*. Ed. by Interscience Publishers. Pure and A. New York, USA.

Succi, Sauro (2001). *The lattice Boltzmann equation: for fluid dynamics and beyond*. Oxford university press.

Sukop, Michael C. and Daniel T. Thorne (2006). *Lattice Boltzmann modeling : an introduction for geoscientists and engineers*. Springer, p. 172. ISBN: 9783642066252.

Thommes, Guido, Mohammed Seaid, and Mapundi K. Banda (2007). "Lattice Boltzmann methods for shallow water flow applications". In: *Int. J. Numer. Methods Fluids* 55.7, pp. 673–692.

Tölke, J. and M. Krafczyk (2008). "TeraFLOP computing on a desktop PC with GPUs for 3D CFD". In: *International Journal of Computational Fluid Dynamics* 22.7, pp. 443–456. ISSN: 1061-8562. DOI: 10.1080/10618560802238275.

Toro, E. (1992). "Riemann problems and the WAF method for solving two-dimensional shallow water equations". In: *Phil. Trans. Roy. Soc. Lond.* A.338, pp. 43–68.

Tubbs, Kevin (2010). "Lattic boltzmann modeling for shallow water equations using high preformance computing". PhD thesis.

Tubbs, Kevin R. and Frank T.-C. Tsai (2011). "GPU accelerated lattice Boltzmann model for shallow water flow and mass transport". In: *International Journal for Numerical Methods in Engineering* 86.3, pp. 316–334.

Ubertini, S., G. Bella, and S. Succi (2003). "Lattice Boltzmann method on unstructured grids: Further developments". In: *Phys. Rev. E* 68 (1), p. 016701.

Valiani, Alessandro, Valerio Caleffi, and Andrea Zanni (2002). "Case Study: Malpasset Dam-Break Simulation using a Two-Dimensional Finite Volume Method". In: *Journal of Hydraulic Engineering* 128.5, pp. 460–472.

Vazquez, M. E. (1999). "Improved Treatment of Source Terms in Upwind Schemes for the Shallow Water Equations in Channels with Irregular Geometry". In: *Journal of Computational Physics* 148.2, pp. 497 –526. ISSN: 0021-9991.

Vukovic, Senka and Luka Sopta (2002). "ENO and WENO schemes with the exact conservation property for one-dimensional shallow water equations". In: *Journal of Computational Physics* 179.2, pp. 593–621.

Wellein, G. et al. (2006). "On the single processor performance of simple lattice Boltzmann kernels". In: *Computers & Fluids* 35.8-9, pp. 910–919. ISSN: 0045-7930. DOI: 10.1016/J.COMPFLUID.2005.02.008.

Wolf-Gladrow, Dieter A (2004). *Lattice-gas cellular automata and lattice Boltzmann models: an introduction*. Springer.

Zarghami, Ahad, Silvia Di Francesco, and Chiara Biscarini (2014). "Porous substrate effects on thermal flows through a REV-scale finite volume lattice Boltzmann model". In: *International Journal of Modern Physics C* 25.02, p. 1350086.

Zhou, J G (2004). *Lattice Boltzmann Methods for Shallow Water Flows*. Springer-Verlag.

Zou, Qisu and Xiaoyi He (1997). "On pressure and velocity boundary conditions for the lattice Boltzmann BGK model". In: *Physics of Fluids* 9.6, p. 1591. ISSN: 10706631. DOI: 10.1063/1.869307. arXiv: 9611001 [comp-gas].